The Dissertation Committee for Yi Zou Certifies that this is the approved version of the following dissertation:

# Near-infrared and Mid-infrared Integrated Silicon Devices for Chemical and Biological Sensing

Committee:

Ray T. Chen, Supervisor

Mikhail Belkin

Andrea Alu

Zheng Wang

Yaguo Wang

Swapnajit Chakravarty

# Near-infrared and Mid-infrared Integrated Silicon Devices for Chemical and Biological Sensing

by

Yi Zou, B.E.; M.E.; M.S.E.

## Dissertation

Presented to the Faculty of the GraduateSchool of

The University of Texas at Austin

in Partial Fulfillment

of the Requirements

for the Degree of

## Doctor of Philosophy

The University of Texas at Austin

December 2014

Dedicated to my family

# Acknowledgements

I would like to express my sincere gratitude and appreciation to my advisor, Dr. Ray T. Chen, for his support and guidance during my doctoral study. I greatly appreciate the chance he gave me to work in his group to conduct my research and pursue my graduate education. Many thanks also go to my committee members, Dr. Mikhail Belkin, Dr. Andrea Alu, Dr. Zheng Wang, Dr. Yaguo Wang, and Dr. Swapnajit Chakravarty, for their insightful advices on my dissertation.

I would like to express my appreciation and gratitude to Dr. Swapnajit Chakravarty, for his help over the years. I would like to thank my colleagues from Optical Interconnect Group and Omega Optics for their help and cooperation. Without their help, I can't finish this dissertation.

Finally, I would like to express my gratitude to my wife, my daughter and my parents for their love and support throughout my life. They always believe in me in difficult times. Without their encouragement and trust, this dissertation would not have reached its conclusion.

# Near-infrared and Mid-infrared Integrated Silicon Devices for Chemical and Biological Sensing

Yi Zou, Ph.D.

The University of Texas at Austin, 2014

Supervisor: Ray T. Chen

Silicon has been the material of choice of the photonics industry over the last decade due to its easy integration with silicon electronics as well as its optical transparency in the near-infrared telecom wavelengths. Besides these, it has very high refractive index, and also a broad optical transparency window over the entire mid-IR till about 8$\mu$m. Photonic crystal is well known that it can slow down the speed of light. It also can provide a universal platform for microcavity optical resonators with high quality factor Q and small modal volumes. The slow light effect, high Q and small modal volumes enhance light-matter interaction, together with high refractive index of silicon can be utilized to build a highly sensitive, high throughput sensor with small footprint.

In this research, we have demonstrated highly compact and sensitive silicon based photonic crystal biosensor by engineering the photonic crystal microcavity in both cavity size and cavity-waveguide coupling condition. We have developed solutions to increase biosensor throughput by integrating multimode interference device and improving the coupling efficiency to a slow light photonic crystal waveguides. We have also performed detailed investigations on silicon based photonic devices at mid-infrared region to develop an ideal platform for highly sensitive optical absorption spectroscopy on chip. The studies have led to the demonstration of the first slot waveguide, the first photonic

crystal waveguide, and the first holey photonic crystal waveguide and first slotted photonic crystal waveguide in silicon-on-sapphire at mid-infrared. The solutions and devices we developed in our research could be very useful for people to realize an integrated photonic circuit for biological and chemical sensing in the future.

# Table of Contents

List of Tables ..... xi

List of Figures ..... xii

Chapter 1 Introduction ..... 1

1.1 Silicon Photonics ..... 1

1.2 Dissertation Organization ..... 2

1.3 Reference ..... 4

Chapter 2 Cavity-waveguide coupling engineered high sensitivity silicon photonic crystal microcavity biosensors with high yield ..... 5

2.1 Introduction ..... 5

2.2 Device Design and Principles ..... 7

2.2.1 Device Principles of Subwavelength Grating Coupler ..... 7

2.2.2 Design Principles of Photonic Crystal Microcavities for sensing ..... 10

2.3 Device Fabrication and Characterization ..... 14

2.3.1 Fabrication ..... 14

2.3.2 Characterization ..... 15

2.3.3 Biosensing ..... 25

2.4 Discussions ..... 29

2.4.1 Yield and quality comparison between end-fire coupling and grating coupling ..... 29

2.4.2 Comparison between L13 and L21 PC microcavity ..... 30

2.5 Conclusion ..... 36

2.6 References ..... 37

Chapter 3 Methods to array photonic crystal microcavities for high throughput biosensor ..... 43

3.1 Introduction ..... 43

3.2 Device Design ..... 45

3.3 Device Fabrication ..... 48

3.4 Device Characterization ..... 50
3.5 Conclusion ..... 55
3.6 References ..... 56

Chapter 4 The role of group index engineering in series-connected photonic crystal microcavities for high density sensor microarrays ..... 58
4.1 Introduction ..... 58
4.2 Device Design ..... 59
4.3 Device Characterization and Discussion ..... 62
4.4 Summary ..... 69
4.5 References ..... 70

Chapter 5 Integrated slot waveguides in silicon-on-sapphire for mid-infrared ..... 72
5.1 Introduction ..... 72
5.2 Device Design ..... 73
5.3 Device Fabrication ..... 79
5.4 Device Characterization ..... 80
5.5 Summary ..... 86
5.6 References ..... 86

Chapter 6 Mid-infrared photonic crystal waveguides in silicon-on-sapphire ..... 88
6.1 Introduction ..... 88
6.2 Device Design ..... 89
6.3 Device Fabrication and Characterization ..... 92
6.4 Discussion ..... 100
6.5 Summary ..... 100
6.6 References ..... 101

Chapter 7 Mid-Infrared Holey and Slotted Photonic Crystal Waveguides in Silicon-on-Sapphire ..... 103
7.1 Introduction ..... 103
7.2 Device Design ..... 104
7.3 Device Fabrication and Characterization ..... 109
7.4 Summary ..... 118

7.5 References ..... 118

Chapter 8 Summary ..... 120

Appendix A: Journal Publications ..... 122

Appendix B: Conference Publications ..... 124

Bibliography ..... 128

# List of Tables

Table 2.1 Comparison of different types of PC microcavities.....34

# List of Figures

Figure 1.1: Intel-labs-SP-Six-Building-Blocks. .....2

Figure 1.2: Schematic of the packaged device showing the multiplexing achieved using multi-mode interference (MMI) beam splitter and multiple photonic crystal microcavities coupled along the length of a single photonic crystal.. .....3

Figure 1.3: Schematic of a slot waveguide and subwavelength grating couplers in silicon-on-sapphire at mid-infrared wavelength.. .....4

Figure 2.1: (a) A schematic of subwavelength grating coupler. (b) Upward power efficiency as a function of grating period $\Lambda_G$ and the effective refractive index $n_{sub}$ of the subwavelength structure. .....9

Figure 2.2: (a) A schematic of photonic crystal microcavity device, (b) dispersion diagram of W1 PCW in water. The W1 guided mode is shown together with frequencies of resonant modes for L13 and L21 PC microcavities by black and red dashed lines respectively. The mode profiles are shown in insets. .....13

Figure 2.3: (a) Schematic of the whole device, (b) close up of the L21 PC microcavity which is locates 4 rows away from a W1 PCW, (c) SEM picture of the fabricated PCW device showing the PCW adiabatic group index taper achieved by adiabatic width taper of PCW and high group index region, (d) SEM image of fabricated grating coupler, (e) magnified view of air holes (f) Normalized transmission of a typical subwavelength grating.. .....15

Figure 2.4: Experimental transmission spectra in water of 19 devices comprising W1 PCW coupled to L13 PC microcavities. Extreme right bottom inset shows microscope image of stitching observed on $20^{th}$ device.. .....17

Figure 2.5: (a) Experimental transmission spectra in glycerol of 9 out of 10 devices comprising W1 PCW coupled to L21 PC microcavities. (b) Output power of all ten L21 devices, (c) transmission spectrum of L21 device #5 (d) SEM image of defect on ridge waveguide section at the input of PCW in Device 5. (e) Electric field intensity profiles of the resonant modes A, B, C and D in (a).....20

Figure 2.6: Distribution of Q and absolute wavelength position in water of resonance modes closest to the band edge for (a) L13 and (b) L21 PC microcavities in Fig. 2.4 and Fig. 2.5. .....21

Figure 2.7: Q-factors (black squares) and bulk sensitivity (blue triangles) variation of (a) L21 microcavity side coupled to W1 PCW in water versus microcavity location change (L21_2 represents L21 microcavity 2 rows away from the PCW) and (b) L55 microcavity side coupled to W1 PCW in water versus microcavity location change. The inset is the transmission spectrum of L55 with cavity located 4 rows away from the PCW.....23

Figure 2.8: Experimental drop resonance spectra for the binding between Avidin to Biotin (Kd~$10^{-15}$M) (a) between 0pM to 100pM and (b) at the lower concentration range between 0pM and 5pM. (c) Experimental spectral shift for various concentrations of avidin binding to biotin in two L21 (red circles and black squares) PC microcavities... .....27

Figure 2.9: Experimental drop resonance spectra for the binding between Avidin to Biotin (Kd~$10^{-15}$M) on L55PC microcavity device (a) between 0fM to 1000fM and (b) at the lower concentration range between 0fM and 100fM. (c) Experimental spectral shift for various concentrations of avidin binding to biotin in L55 PC microcavities. ….....28

Figure 2.10: (a) Experimental spectra of (a) L13 and (b) L21 PC microcavities showing shift of resonance mode closest to the band edge in water (black) versus glycerol (red), (c) Experimental spectral shift for various concentrations of avidin binding to biotin in L13 (filled triangles) and L21 (filled squares) PC microcavities. Experimental Q variation for L13 (open triangles) and L21 (open squares) devices are also shown.....32

Figure 2.11: Comparison of minimum experimentally demonstrated detection limits versus other label-free optical platforms as a function of sensing area on chip. Red dots represent data obtained in our PC microcavity biosensors coupled to a W1 PCW.....35

Figure 3.1: (a) Generalized schematic of the test system on chip with integrated 1×x MMI and PC microcavities coupled to PC waveguides. On each of the x output arms of the MMI, multiple PC microcavities are arrayed. Each microcavity is coated with a different target receptor biomolecule, each responsive to its specific conjugate, as indicated by a different color. (b) Stitched microscope image of 1×4 MMI device studied here... .....46

Figure 3.2: (a) SEM of PC devices on 4 arms of a 1×4 MMI (b) Simulation showing optical power distribution in 1×4 MMI... .....48

Figure 3.3: (a) SEM image of L13 PC microcavity adjacent to a W1 PCW. (b) Electric field intensity profile of the resonance mode of the L13 PC microcavity.. .....50

Figure 3.4: (a) Transmission spectrum of W1 PCW with coupled L13 PC microcavity. (Inset) shows the normalized transmission, magnifying the wavelength range around the resonance. (b) Wavelength shift of the resonance shown by arrow in (a) as a function of concentration of probe antibodies, rat anti-Human IL-10 (open circles) and goat anti-rabbit IgG (filled circles). (inset) shows the spectral shift from black to red curve when 0.1nM of probe rat anti-Human IL-10 antibodies is added to a 0nM PBS background. Dashed line indicates detection limit.....52

Figure 3.5: Resonance wavelength shift or none thereof observed in the (a)-(c) L13 PC microcavities in arms #1-#3 of the 1×4 MMI when probe antibodies goat anti-rabbit IgG in PBS and rat anti-human IL-10 in PBS are added in sequence and (d) arm #4 of the 1×4 MMI with 1nM of probe antibodies of goat anti-rabbit IgG in PBS.....55

Figure 4.1: (a) Schematic of the PC sensor device with input and output strip waveguide, PC group index tapers, PC guiding region and L3 PC microcavity. (b) Dispersion diagrams of W1 (solid), and W1.08 (dash) PCWs in water (n=1.33) for PC with a=392.5 nm. The normalized resonance frequency of the coupled PC microcavity at a=392.5 nm is denoted by D. C, B, and A denote the normalized resonance frequencies of L3 PC microcavities in PC regions with a= 393.5 nm, 394 nm and 396 nm respectively cascaded in series with D (a=392.5 nm). Group index is plotted and its magnitude at the coupling frequency indicated in respective colors.....61

Figure 4.2: Scanning electron micrograph of the fabricated device, a) full device with 16 arms, b) each of the 16 arms with 4 cascaded microcavities, c) PCW adiabatic group index taper achieved by adiabatic width taper of PCW and high group index region, d) one of the 4 cascaded microcavities shown in (b), e) close up of the L3 PC microcavity located 2 rows away from a W1 PCW.. .....62

Figure 4.3: Normalized transmission spectral of W1 PCW with coupled series-connected L3 PC microcavities, a) 2 cavities, b) 3 cavities, c) 4 cavities with index taper; d) 2 cavities, e) 3 cavities, f) 4 cavities without index taper. All spectra are measured in water ambient. Resonant peaks are shown by arrows in (a), (b) and (c). In (c), resonant peaks are also labeled as A, B, C and D corresponding to Fig. 4.1(b). Inset (b) shows magnified linear scale spectrum of resonance peak closest to the bandedge. The dash line shows the full width at half maximum (FWHM)... .....64

Figure 4.4: Normalized transmission spectrum of five series-connected L3 microcavity with index taper, in water. Spectrum is normalized to reference strip waveguide, and resonant peaks are shown by arrows. Red curve is obtained by a Lorentz fit of the two individual resonances shown by dashed arrows... .....67

Figure 4.5: Output spectra of high density microarray with a total of 64 sensors integrated into 16 arms inside one device. 4 series-connected L3 microcavity are side coupled to PCW on each arm. All spectra are measured in water. 16 arms are made from a two stage cascaded 1×4 MMI in Fig. 4.2(a)... .....68

Figure 5.1: (a) Confinement factor as a function of slot width S and rail width W, (b) simulated electric field for a slot waveguide with W=0.6μm and S=0.13μm.A high confinement in the slot is obtained.. .....74

Figure 5.2: (a) Simulated electric field for the mode converter, the simulation data shows 98% of conversion efficiency from strip waveguide mode to the slot waveguide mode when $L_{taper}1$=4μm and $L_{taper}2$=10μm. (b) Conversion efficiency as a function of $L_{taper1}$ and $L_{taper2}$.... .....76

Figure 5.3: (a) Simulated coupling efficiency from fiber (red curve) show the peak is located around 3.4μm, and the reflection (black curve), and (b) simulated output optical field from grating coupler to fiber.....78

Figure 5.4: (a) Schematic of the fabricated device, (b) SEM image of fabricated slot waveguide, (c) SEM image of SWG coupler, (d) magnified view of air holes, (e) close up of strip waveguide to slot waveguide mode converter, and (f) SEM image of single mode strip waveguide with 1μm width..80

Figure 5.5: Schematic of the experimental setup used to characterize our devices. .....81

Figure 5.6: Experimental measured and simulated coupling efficiency with different incident angles.... .....82

Figure 5.7: (a) Measured loss of eight single mode waveguides fabricated on SOS operating at 3.4 μm wavelength. The waveguides are 0.6μm in height and 1 μm in width. 2.1dB/cm propagation loss is achieved by linear fitting. (b) Measured loss of eight slot waveguides fabricated on SOS operating at 3.4 μm wavelength. A 11dB/cm propagation loss is achieved by linear fitting.... .....84

Figure 5.8: Measured loss versus number of strip-to-slot waveguide mode converters at an operating wavelength of 3.4μm. Approximately -0.13dB loss per mode converter is measured, corresponding to 97% conversion efficiency.....85

Figure 6.1: (a) 3D FDTD simulation of a short W1 PCW in silicon-on-sapphire for operation at 3.43μm with a=845nm. The different parts of the transmission spectrum are indicated. (b) Set of 3D FDTD simulations of short W1 PCWs with different lattice constants a. Simulation for a=845nm is indicated by the dotted black plot. The output spectrum of our source ICL is indicated by the dashed black plot (right axis)... .91

Figure 6.2: 2D plane wave expansion simulation of the dispersion diagram of a sapphire clad silicon W1 PCW. The red dashed line indicates the PCW dispersion at the interface between silicon ridge waveguide and W1.07 PCW. The reduced group index at the interface is indicated by the lesser slope (dashed blue lines) at a representative frequency $a/\lambda$=0.246. Sapphire light line is superimposed..... .....93

Figure 6.3: (a) Microscope image of the device showing input and output SWGs and PCW. (b) Top view SEM image of PCW and (c) side view SEM image of the PCW at the PCW-strip waveguide interface. Magnified top view SEM images of (d) input taper (e) PCW and (f) output taper.....94

Figure 6.4: (a) Normalized transmitted intensity through an air-clad W1 PCW in SoS with $r$=0.25$a$, as a function of $a$ at λ=3.43μm plotted (a) in air (bold circles) and $C_2Cl_4$ (open circles) and (b) as a function of temperature at 25°C (bold circles) and 60°C (open squares). Insets magnify the data for devices between $a$=840nm and $a$=855nm.....96

Figure 6.5: (a) Transmission losses in W1 PCWs in SoS below the light line for $a$=846nm (○), $a$=848nm (■) and $a$=850nm (●) at λ=3.43μm. Insets plot the propagation losses above the light line for devices with $a$=855nm (■), 860nm (■), 865nm (●), 870nm (●) and 890nm (□). (b) Solid line plot is the group index profile versus wavelength for W1 PCW in Fig. 6.2 with $a$=845nm. Estimated propagation group indices versus lattice constant are plotted with filled circles. Experimental propagation losses for measured devices are plotted versus lattice constant with open circles (right axis).....99

Figure 7.1. (a) Schematic of the holey W1.2 PCW with a row of smaller air holes with radius $rs$=0.625$r$, in the center of the PCW. (b) Dispersion diagram of the device in (a) by plane-wave expansion. (c) Electric field intensity profile of the propagating slow light at the Brillouin zone boundary mode shown by red circle in (b). (d) Cross-section of the electric field intensity in (c) profile through the smaller air holes in the center of the PCW.....106

Figure 7.2: (a) Schematic of the slotted W1.5 PCW with a rectangular slot s=0.155a, in the center of the PCW. (b) Dispersion diagram of the device in (a) by plane-wave expansion. (c) Electric field intensity profile of the propagating slow light mode at the Brillouin zone boundary shown by red circle in (b). (d) Cross-section of the electric field intensity profile in (c)..... .....108

Figure 7.3: (a) Electric field intensity profile of the propagating slow light mode in a W1 PCW at the Brillouin zone boundary. (b) Cross-section of the electric field intensity profile in (a)..... .....109

Figure 7.4: (a) Top view SEM image of the holey PCW. Top view magnified images showing the holey PCW (b) at the interface between the PCW and the input ridge waveguide in (a) and (c) near the center of the device... .....111

Figure 7.5: Top view SEM image of the slotted PCW. (b) Top view magnified images showing the slotted PCW near the center of the device image in (a). (c) Top view and (d) $70^{o}$ tilt view of the slot mode converter at the input (or output) of the slotted PCW.....112

Figure 7.6: (a) Normalized transmitted intensity through an air-clad W1.2 holey PCW in SoS with r=0.25a, rs=0.625r as a function of a at λ=3.43μm plotted in air (bold circles). Propagation losses were measured for few devices (open circles). Insets magnify the data for devices between a=830nm and a=845nm. (b) Propagation loss for devices of different length at a=840nm (magenta), a=845nm (green), a=850nm (black), a=865nm (blue), a=870nm (yellow), and a=890nm (red)..... .....113

Figure 7.7: Normalized transmitted intensity through an air-clad W1.5 slotted PCW in SoS with $r$=0.25$a$, $s$=0.155$a$ as a function of $a$ at λ=3.43μm plotted in air..... .....115

Figure 7.8: Normalized transmitted intensity through an air-clad W1.2 holey PCW in SoS with $r$=0.25$a$, as a function of $a$ at λ=3.43μm plotted (a) in air (red) and $C_2Cl_4$ (black) and (b) as a function of temperature at 25°C (black) and 60°C (red).....116

Figure 7.9: Normalized transmitted intensity through an air-clad W1.5 slotted PCW in SoS with $r$=0.25$a$, $s$=0.155$a$, as a function of $a$ at λ=3.43μm plotted as a function of temperature at 25°C (black) and 60°C (red).....118

# Chapter 1: Introduction

## 1.1 SILICON PHOTONICS

Silicon photonics has attracted a lot of interests in the past decade. Benefiting from mature fabrication technologies developed by semiconductor industry and high refractive index, it is a very promising platform for high density integration of photonic devices. It is compatible with CMOS fabrication and therefore high volume manufacturing is feasible. Currently it is not only being actively researched by academic research groups, but also by many electronics manufacturers including IBM and Intel. Fig. 1.1 shows the six main building blocks for investigation in order to "siliconize" photonics. It is deemed as a means to bridge the gap between photonics and electronics. Besides, silicon has very wide transparency window can cover from near-infrared to mid-infrared [1,2]. Hence it is potentially a viable material for wide wavelength range applications. To utilize its highly transparent property, mature fabrication technologies, and high refractive index to build low cost, high yield, high density on-chip integrated devices in near-infrared and mid-infrared will be very meaningful for both optical interconnect and optical sensing applications.

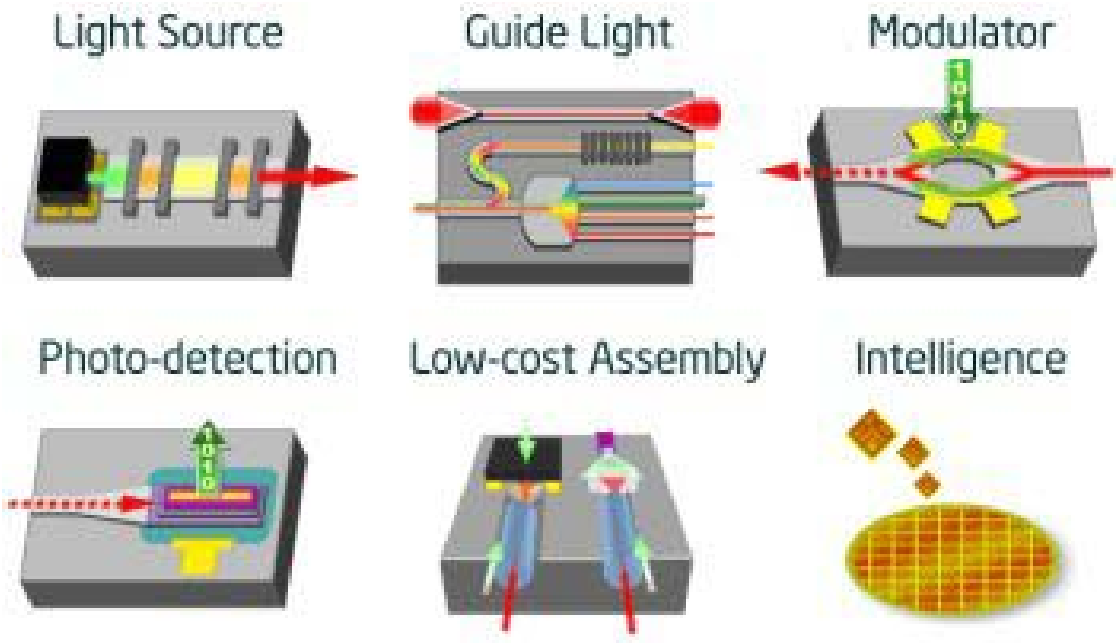


Figure 1.1: Intel-labs-SP-Six-Building-Blocks

In this dissertation, the results of my research in past four years are presented. The design, fabrication, and experimental results of photonic crystal microcavity devices for near-infrared biosensing are discussed here. In addition, the strip and slot waveguide working in mid infrared region are also discussed for chemical sensing. I will also show the first slot waveguide and the first photonic crystal waveguide in silicon-on-sapphire, the first holey and slotted photonic crystal waveguide in mid-infrared demonstration.

## 1.2 Dissertation Organization

This dissertation is organized as follows. The first three chapters conclude my research in biosensing field in past few years. A schematic of our on-chip biolab is show in Fig. 1.2. In Chapter II, the way to improve sensitivity of photonic crystal microcavity devices for detection of biomolecules while keeping high quality factor is described. By increasing a cavity length within the limit of our ink-jet printer while laterally shift the

position of cavity, we can increase the sensing area, enhance the quality factor, and hence lead to higher sensitivity. The use of subwavelength grating couplers for light coupling into and out of the chip also guarantees highly efficient coupling, clean spectrum and high yield. In Chapter III, I will talk about the way to multiplex several sensor spots into one device to improve the throughput of our photonic crystal based biosensors. Using multi-mode interference and series-connection, we demonstrated a lab on a chip which can detect several biomarkers simultaneously. In Chapter IV, the role of group index engineering in cascaded photonic crystal microcavities design is discussed. By properly designing the group index tapers, one high density sensor array with 64 photonic crystal microcavities devices integrated are demonstrated.

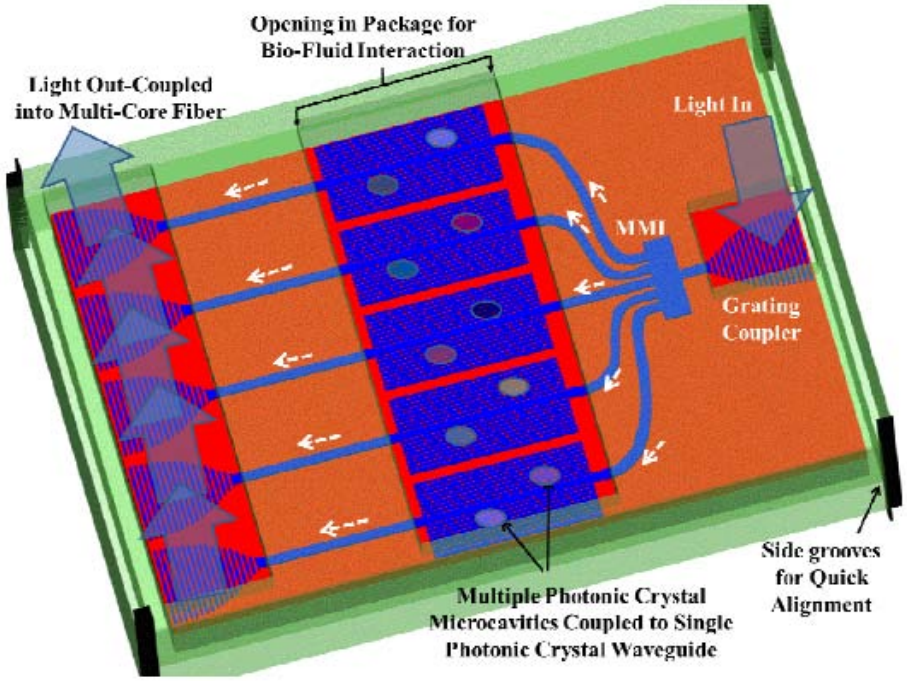


Figure 1.2: Schematic of the packaged device showing the multiplexingachieved using multi-mode interference (MMI) beam splitter and multiple photonic crystal microcavities coupled along the length of a single photonic crystal.

The next three chapter conclude the research I have done in my PhD study in mid-infrared device building. Fig. 1.3 shows a schematic of a slot waveguide together with subwavelength couplers in silicon-on-sapphire working at mid-infrared wavelength. In Chapter V, I will discuss silicon based photonic devices at wavelength 3.43μm. The design of subwavelength grating couplers, strip waveguide and slot waveguide are demonstrated. The first photonic crystal waveguide in silicon-on-sapphire working at mid-infrared region is introduced in Chapter VI. A method to characterize the photonic crystal waveguide using single wavelength source is presented. To further enhance light-matter interaction, holey and slotted photonic crystal waveguides are also proposed and demonstrated in Chapter VII. The design and characterization are discussed. The following chapter, Chapter VIII, summarized the work I have done in my PhD study.

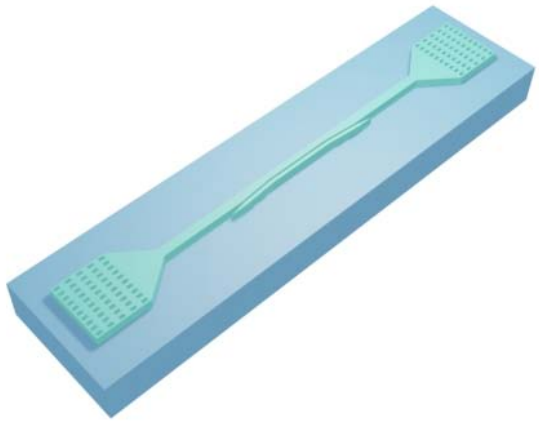

Figure 1.3: Schematic of a slot waveguide and subwavelength grating couplers in silicon-on-sapphire at mid-infrared wavelength.

## 1.3 REFERENCES

[1] R. Soref, Nat. Photonics 4(8), 495 (2010).

[2] R. Soref, S. J. Emelett, and A. R. Buchwald, J. Opt. A 8(10), 840 (2006).

# Chapter 2: Cavity-Waveguide Coupling Engineered High Sensitivity Silicon Photonic Crystal Microcavity Biosensors with High Yield[1]

## 2.1 INTRODUCTION

Silicon photonics is a promising platform for high density integration of photonic devices. Since it is compatible with CMOS fabrication, hence high volume manufacturing is feasible. However, although silicon photonics has several performance advantages, coupling of light into and out of silicon devices reliably has been a primary impediment towards large scale adoption to real applications. Optical fibers are the primary medium for guiding light into and out of the photonic chips. However, silicon based optical devices suffer very high loss when coupling light into/out from chips, due to large mode and effective index mismatches between fiber and silicon waveguide, dimensions of which are of the order of several hundred nanometers. Several coupling approaches have been proposed to address this problem. Methods typically adopted are inverse tapers [1]- [4] and grating couplers which include traditional air trench grating design [5]-[10] and subwavelength nanostructures [11]-[16]. The results show that coupling efficiency can be significantly improved in subwavelength grating couplers which therefore provide significant design freedom to meet the requirement of different

[1] Y. Zou, et. al., Selected Topics in Quantum Electronics, IEEE Journal of, vol.20, no.4, pp.1-10 (2014).

Y. Z. designed, fabricated the device, performed the experiments, analyzed the data, wrote the manuscript; S. C. designed the PC device, analyzed the data, and revised the manuscript; D. N. K and X. X helped design the subwavelength grating couplers; W. L. helped prepare Avidin solution; X. Lin helped draw the schematic. Y. G and A. H. helped analyze the data. R. T. C. oversaw all research phases and revised the manuscript. All authors discussed and commented on the manuscript.

applications. In recent work, it was shown that subwavelength grating couplers with high coupling efficiency for transverse-electric (TE) polarization can be fabricated simultaneously with other photonic devices thereby adding no additional steps in fabrication [15]. In particular, a 2-D photonic crystal comprising air holes etched into dielectric silicon supports an in-plane band gap for light with TE polarization but does not support a sufficiently wide in-plane band gap for transverse-magnetic (TM) polarization. Consequently, a TE selective subwavelength grating coupler introduces an additional polarization filter that further increases the extinction ratio between TE and TM polarizations inside the photonic crystal waveguide. In recent years, photonic crystal (PC) microcavities, because of its compact size (of the order of a few square microns in surface area) and high sensitivity, have attracted significant interest in biosensing. The principle of operation transduces the specific binding of the biomolecule of interest to its conjugate biomolecule receptor bound to the photonic crystal microcavity into an optical signal. When compared to other chip-integrated sensing platforms such as ring-resonators (RR) [17], [18], wire waveguides [19] and surface plasmon resonance (SPR) [20], PC microcavities have higher sensitivity due to its slow light effect, high quality factor resonances and a larger optical mode overlap with the analyte within a compact optical mode volume [21]. However, in spite of significant success in demonstrating highest sensitivity biosensors [22], working device yield using end-fire coupling, after successful fabrication was dismal, of the order of 10% in some instances [23].

In this letter, we show that by integrating subwavelength grating couplers with PC microcavity coupled waveguides for biosensing, coupling efficiency increased compared to previous end-fire coupling methods. Furthermore, the working device yield is significantly improved to 80% with significantly improved spectral purity of observed

resonances. By further engineering the loss due to the leakage of light from the PC microcavity to the PC waveguide in addition to microcavity engineering to improve the uncoupled cavity quality factor, we experimentally detected biomolecular concentrations more than one order of magnitude better than our previous results [22]. Our preliminary yield results combining subwavelength grating couplers with PC microcavity coupled waveguides are extremely significant for biosensing microarray applications that will consider dense integration of multiple simultaneously interrogated sensors on chip [24].

## 2.2 Device Design and Principles

### 2.2.1 Device Principles of Subwavelength Grating Coupler

The subwavelength grating (SWG) coupler works on the same principle as the traditional grating coupler. However, the SWG replaces the air trenches with a subwavelength nanostructure, as shown in Fig. 2.1(a). According to effective medium theory (EMT) [25], a composite medium comprising two different materials interleaved at the subwavelength scale can be treated approximately as a homogenous medium with an effective refractive index between these two materials. Based on these two working principles, the SWG coupler covered by SU8 resist protection layer was simulated by two-dimensional simulation package CAMFR using the design rules laid down previously [15]. The grating period and effective refractive index were scanned simultaneously to get the maximum upward coupling efficiency through the SWG. The simulation result is shown in Fig. 2.1(b).

When the grating period $\Lambda_G$ (in the propagation direction) is fixed at 735nm and the effective refractive index $n_{sub}$ of subwavelength region is set as 2.15 which are indicated in Fig. 2.1(b), the upward coupling efficiency to air reaches its maximum at around 26% with an emitting angle of 14 $^{o}$. The duty cycle is 50%. 22 periods are chosen

to make the grating region 14 μm wide and 16 μm long that can match well with the mode size of a single mode fiber. The SWG size thus provides some tolerances to make the alignment easily during measurement [11]. $L_{sub}$ and $W_{sub}$ represent the trench dimension along and perpendicular to the propagation direction respectively. $\Lambda_{sub}$ is the grating period perpendicular to the propagation direction. The values for parameters $\Lambda_{sub}$ and $W_{sub}$ are calculated according to 1D stratified structure [26]. The refractive indices of subwavelength structure for TE and TM polarizations can be calculated from Eqns. 1 and 2 below.

$$\begin{aligned} \text{TE}: & \frac{\sqrt{n_{si}^2 - n_{TE}^2}}{n_{si}^2} \tan\left( \frac{\pi \sqrt{n_{si}^2 - n_{TE}^2}\,(\Lambda_{sub} - W_{sub})}{\lambda} \right) \\ = & -\frac{\sqrt{n_{hole}^2 - n_{TE}^2}}{n_{hole}^2} \tan\left( \frac{\pi \sqrt{n_{hole}^2 - n_{TE}^2}\, W_{sub}}{\lambda} \right) \end{aligned} \tag{1}$$

$$\begin{aligned} \text{TM}: & \sqrt{n_{si}^2 - n_{TM}^2} \tan\left( \frac{\pi \sqrt{n_{si}^2 - n_{TM}^2}\,(\Lambda_{sub} - W_{sub})}{\lambda} \right) \\ = & -\sqrt{n_{hole}^2 - n_{TM}^2} \tan\left( \frac{\pi \sqrt{n_{hole}^2 - n_{TM}^2}\, W_{sub}}{\lambda} \right) \end{aligned} \tag{2}$$

where $n_{TE}$ and $n_{TM}$ denote refractive indices of the subwavelength structure for TE and TM polarizations, respectively, while $n_{si}$ and $n_{hole}$ are the refractive indices of silicon and material inside the hole respectively. Since a 2D PC lattice of holes in a dielectric supports TE polarization, Eqn. 1 is selected for design. And considering fabrication yield and repeatability limitations, we set the trench width $W_{sub}$=100nm and thus we can fix the parameter $\Lambda_{sub}$=294nm which corresponds to a filling factor around 34%.

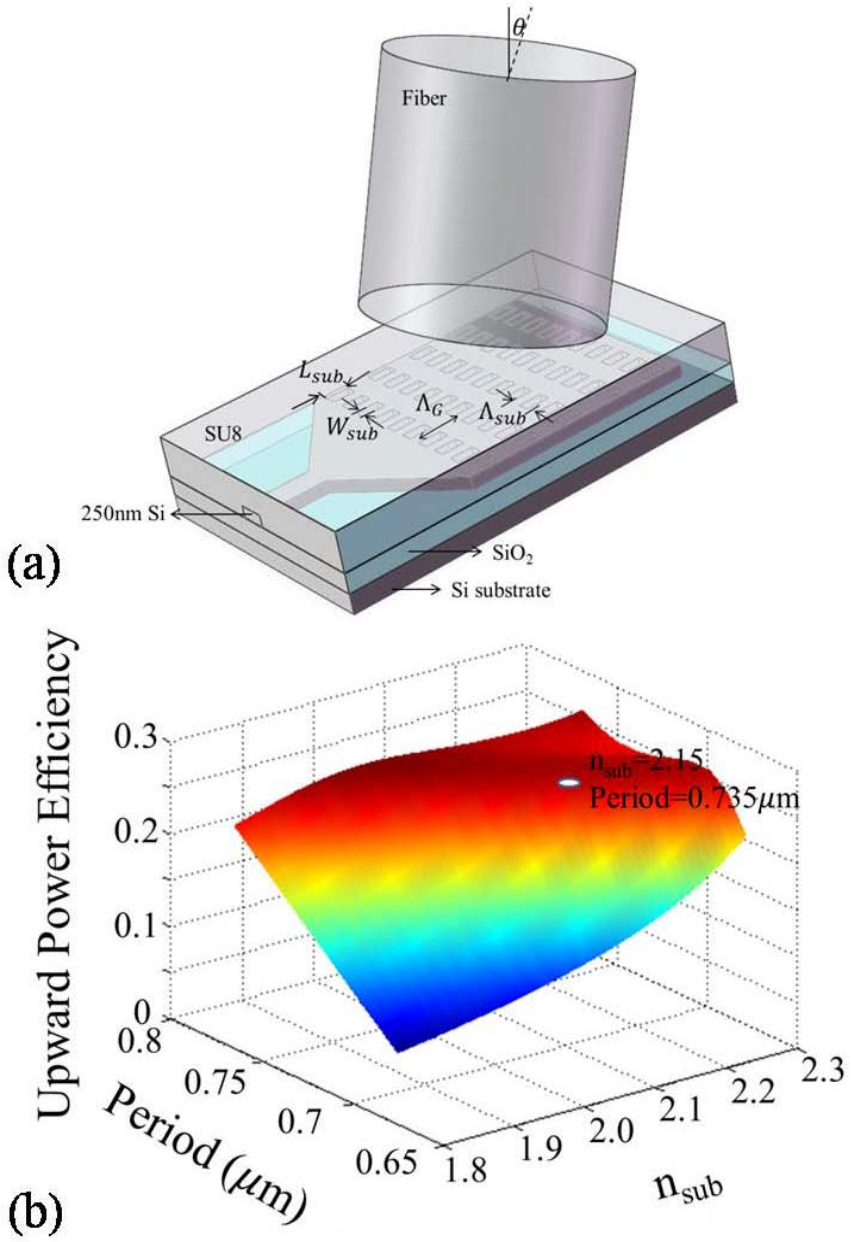


Figure 2.1: (a) A schematic of subwavelength grating coupler. (b) Upward power efficiency as a function of grating period $\Lambda_G$ and the effective refractive index $n_{sub}$ of the subwavelength structure.

### 2.2.2 Design Principles of Photonic Crystal Microcavities for Sensing

The device investigated consists of a L*n* type PC microcavity side coupled to a W1 type Photonic Crystal waveguide (PCW), where *n* denotes the number of missing air holes along the Γ–K lattice direction in a triangular lattice photonic crystal and W1 demotes that the width of the PCW is $\sqrt{3}a$ where a is the lattice constant. The schematic of the PC microcavity coupled waveguide device is shown in Fig. 2.2(a).

The total quality factor $Q_T$ of the resonance mode of a PC microcavity side coupled to a PCW, which is related to the photon lifetime $\tau_p$, at frequency $\omega$ by $Q_T=\omega\tau_p$ is given by

$$\frac{1}{Q_T}=\frac{1}{Q_i}+\frac{1}{Q_R}+\frac{1}{Q_{WG}} \tag{3}$$

where $Q_R=\omega\tau_R$, $Q_i=\omega\tau_i$, and $Q_{WG}=\omega\tau_{WG}$, $\tau_R$, $\tau_i$ and $\tau_{WG}$ represent time constants for the radiation loss, intrinsic cavity loss and waveguide loss respectively. $\tau_R$ is given by:

$$\frac{1}{\tau_R}=\frac{P_R}{W_E} \tag{4}$$

where $P_R$ denotes the total power radiated by the cavity and $W_E$ denotes the stored energy in the cavity which is proportional to the cavity mode volume. We have shown previously [23] that increasing the length of the PC microcavity increases $W_E$. An increased cavity length also lowers the normalized frequency of the resonant mode in the photonic band gap leading to a decrease in the fraction of the optical mode above the bottom oxide cladding light line, and a corresponding decrease in $P_R$. Both factors lead to an increase in the effective Q. At the same time, increasing the length of the PC microcavity increases the analyte overlap with the resonance mode of the PC microcavity. Since the sensitivity of the device is determined by the resonance wavelength shift needed to observe the smallest change in concentration, a large resonance wavelength shift is desired for a given concentration of chemicals or

biomolecules. The microcavity resonance Q and the analyte overlap with the resonance mode both determine the resonance wavelength shift and hence the sensitivity of the device.

We previously showed that in biosensing microarrays, where multiple sensor spots must be coated with unique immobilized antibodies, the method of dispensing the antibodies to be immobilized such as via ink-jet printing or by using microfluidic channels, determines the density of integration. The diameter of the dispensed spot in ink-jet printing is 35 μm in our system with a 50 μm center-to-center spacing between individual dispensed spots [23]. The diameter of 35 μm thus determines the upper limit of miniaturization in biosensing microarrays. We take advantage of the biopatterning engineering limitation to derive the dual benefits of a longer cavity design resulting in higher Q and a larger optical mode overlap with the analyte, to achieve higher sensitivities.

The simulated dispersion diagram of a W1 PCW is shown in Fig. 2.2(b). The resonance frequencies of the L13 and L21 PC microcavities are shown by the dotted black and dotted red lines respectively. As the cavity size increases from L13 to L21, the resonance frequency moves closer to the band edge and $P_R$ decreases. Since $W_E$ is larger for the L21 PC microcavity, $Q_R$ is effectively increased. As observed from Fig. 2.2(b), the group index of the W1 PCW at the coupling frequencies is higher for the L21 ($n_g$ =16) compared to the L13 ($n_g$ =13.2) PC microcavity. Enhanced optical coupling from the waveguide to the microcavity leads to enhanced light-matter interaction thus improving sensitivity as we have shown elsewhere [27].

In an uncoupled cavity, increasing the length of the PC microcavity increases the total Q of resonance modes. However, simply increasing the length of the microcavity from L13 to L21 based on equation 4 does not increase $Q_T$ for the resonance modes of

interest in the cavity-waveguide architecture. A longer cavity leads to increased leakage from the cavity to the PCW leading to lower $Q_{WG}$ which lowers the effective $Q_T$. A high $Q_T$ is desirable since it enables smaller changes in concentration to be detected. Hence, an optimum design requires optimizing the cavity-waveguide coupling for high Q and high sensitivity, in addition to other factors such as the magnitude of slow light in the coupling waveguide that we have discussed elsewhere [27]. To optimize $Q_T$ while enhancing sensitivity, the PC microcavity is moved laterally away from the PCW to increase $Q_{WG}$. In this chapter, we further investigated the effect of the lateral spacing between the cavity and the waveguide on $Q_T$ and sensitivity of the L21 PC microcavity and engineered an optimized spacing to achieve the highest $Q_T$.

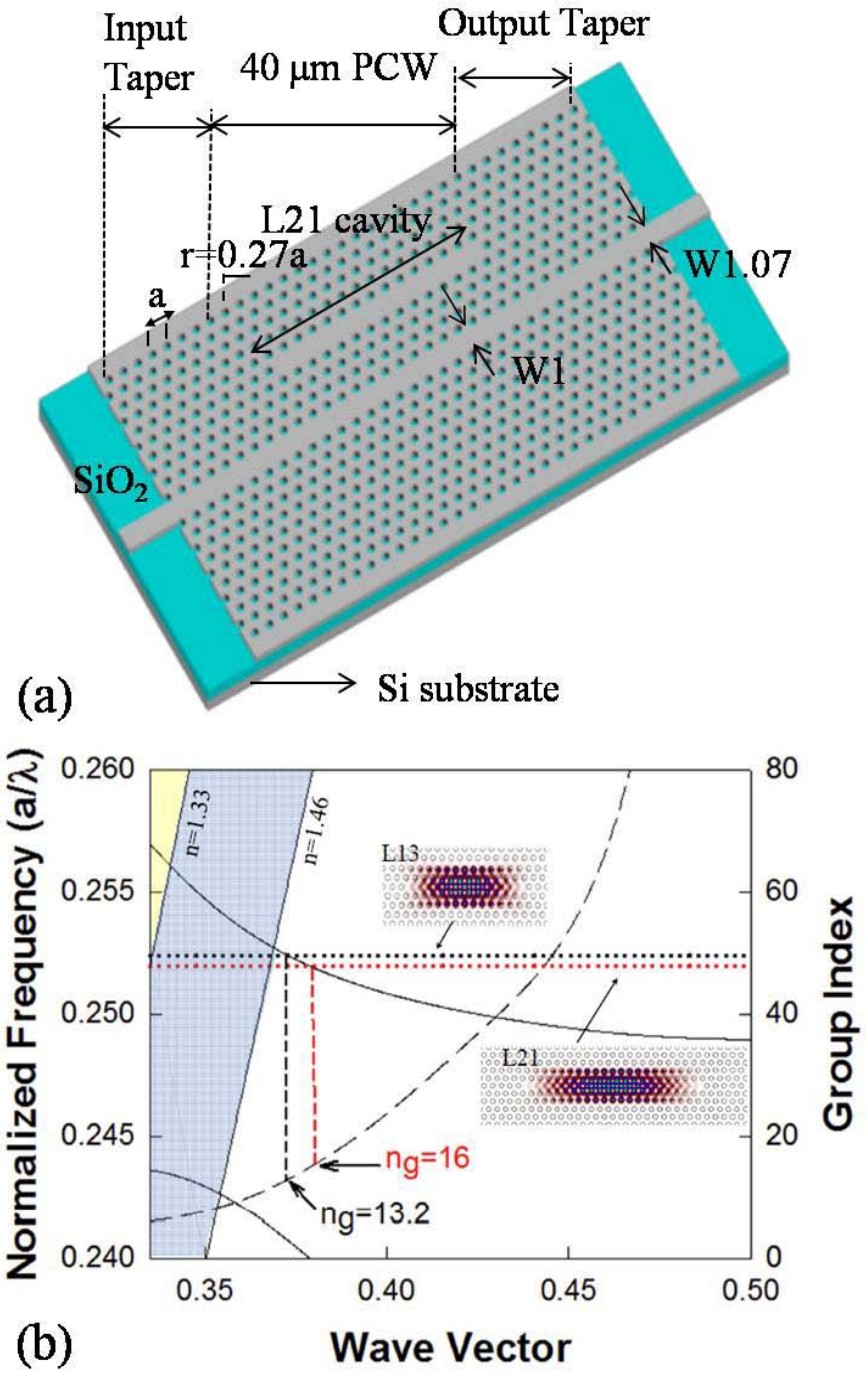


Figure 2.2 (a) A schematic of photonic crystal microcavity device, (b) dispersion diagram of W1 PCW in water. The W1 guided mode is shown together with frequencies of resonant modes for L13 and L21 PC microcavities by black and red dashed lines respectively. The mode profiles are shown in insets.

## 2.3 Device Fabrication and Characterization

### 2.3.1 Fabrication

The devices were fabricated on silicon on insulator (SOI) wafer with 250nm top silicon layer and 3µm buried oxide. PC waveguides, PC impedance tapers to minimize reflection loss, strip waveguides and SWG couplers are patterned simultaneously in one step with e-beam lithography using ZEP-520A e-beam resist followed by reactive ion etching using $Cl_2$/HBr. The diameter of PC holes is 216nm with 393nm period while subwavelength structure has air holes with 100nm by 367.5nm in dimension. The whole chip shown in Fig. 2.3(a) is then coated with 5µm thick SU8 in order to protect the SWG coupler from any interference during biosensing and an open channel is next patterned on top of the PCW region for sensing purpose. SEM images of the fabricated L21 type PC microcavity and SWG coupler are shown in Fig. 2.3. For measurement ease, the total length of the device between the input and output SWG couplers is 1cm.

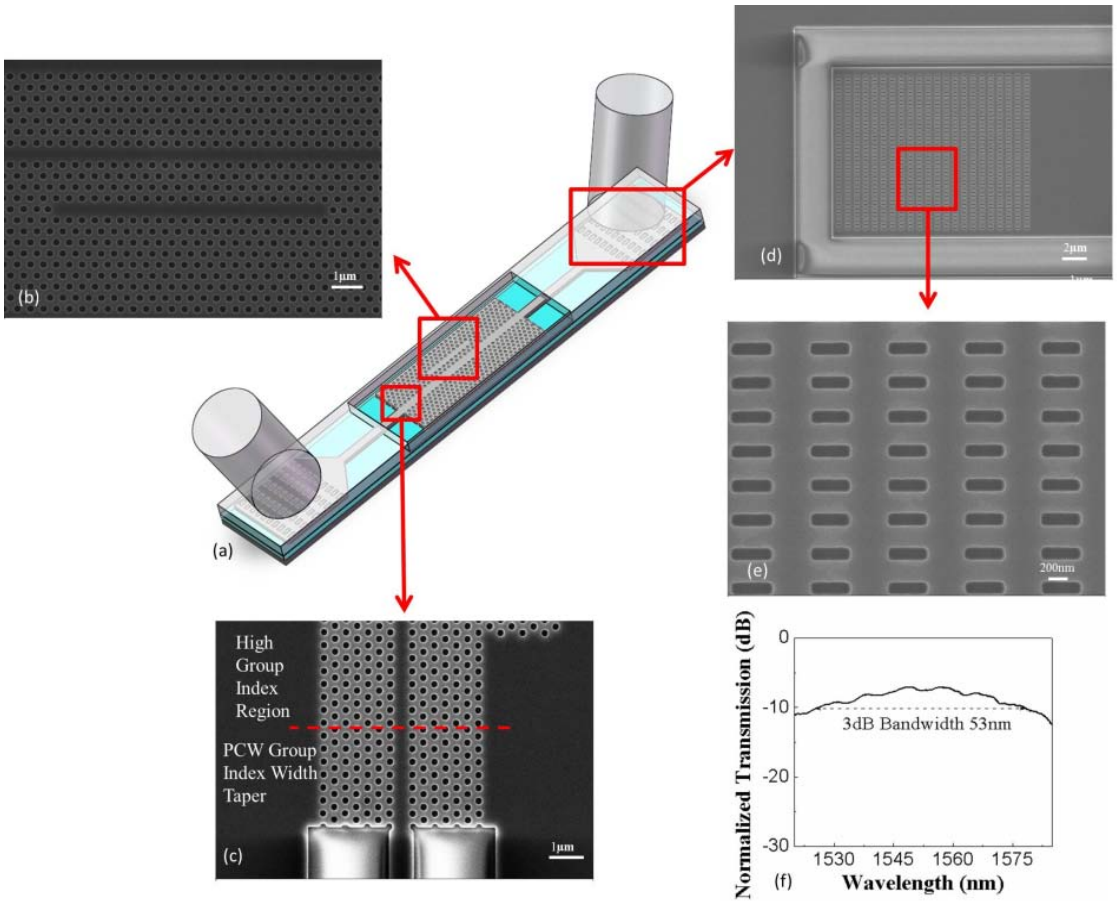


Figure 2. 3 (a) Schematic of the whole device, (b) close up of the L21 PC microcavity which is locates 4 rows away from a W1 PCW, (c) SEM picture of the fabricated PCW device showing the PCW adiabatic group index taper achieved by adiabatic width taper of PCW and high group index region, (d) SEM image of fabricated grating coupler, (e) magnified view of air holes (f) Normalized transmission of a typical subwavelength grating.

### 2.3.2 Characterization

The measurement setup has been described in a previous paper [15]. Input TE polarized light is coupled to the input SWG with a polarization maintaining single mode fiber. Light is coupled out of the output SWG via a standard single mode fiber. Light is

guided in and out of the PCW by ridge waveguide with PC group index taper to enable high coupling efficiency into the slow light guided mode. The group index taper can be done by tuning the hole sizes [28] or the width of the PCW. Position shifting is a more fabrication friendly approach [29], since the accurate control of several different hole sizes requires more optimizations of dose matrices in lithography. The PCW adiabatic group index taper, shown in Fig. 2.3(c), is achieved by gradually increasing the widths of the first eight periods of PCW to reduce the group index. The bottom cladding of silicon dioxide (n=1.46) is kept intact to enable robust devices with high yield. The SWG coupler is firstly characterized by measuring the insertion loss of fiber-to-device-to-fiber. The coupling efficiencies of two couplers are assumed as equal. In Fig. 2.3(f), The grating efficiency curve indicates that the peak efficiency for one SWG coupler is around -7dB which corresponding to 20% efficiency at 1550nm. The 3dB bandwidth is around 53nm. The efficiency is lower than air-clad SWGs reported previously [15] due to the SU8 top cladding of grating region in devices for chemical and biological sensing. The SU8 serves as the protection layer to eliminate any interference to the grating signal and resultant coupling efficiency due to analyte spreading during biosensing. The output spectrum of the grating was used as reference to normalize transmission data from microcavity coupled W1 PCW devices on the same chip.

20 L13 PC microcavity coupled to W1 PCW devices were fabricated on two chips and measured in water. 19 out of 20 devices show good waveguide transmission spectra with clear and sharp transmission band edges in which the power drops more than 20dB within a 5nm wavelength range over the transition from wavelength transmission band to transmission band gap. The spectra from each of the nineteen devices in water are shown in Fig. 2.4. No output power was observed from the 20th device due to the stitching

effect in the input grating coupler that can be seen in the extreme right bottom segment of Fig. 2.4 as a dark green line at the center of the grating.

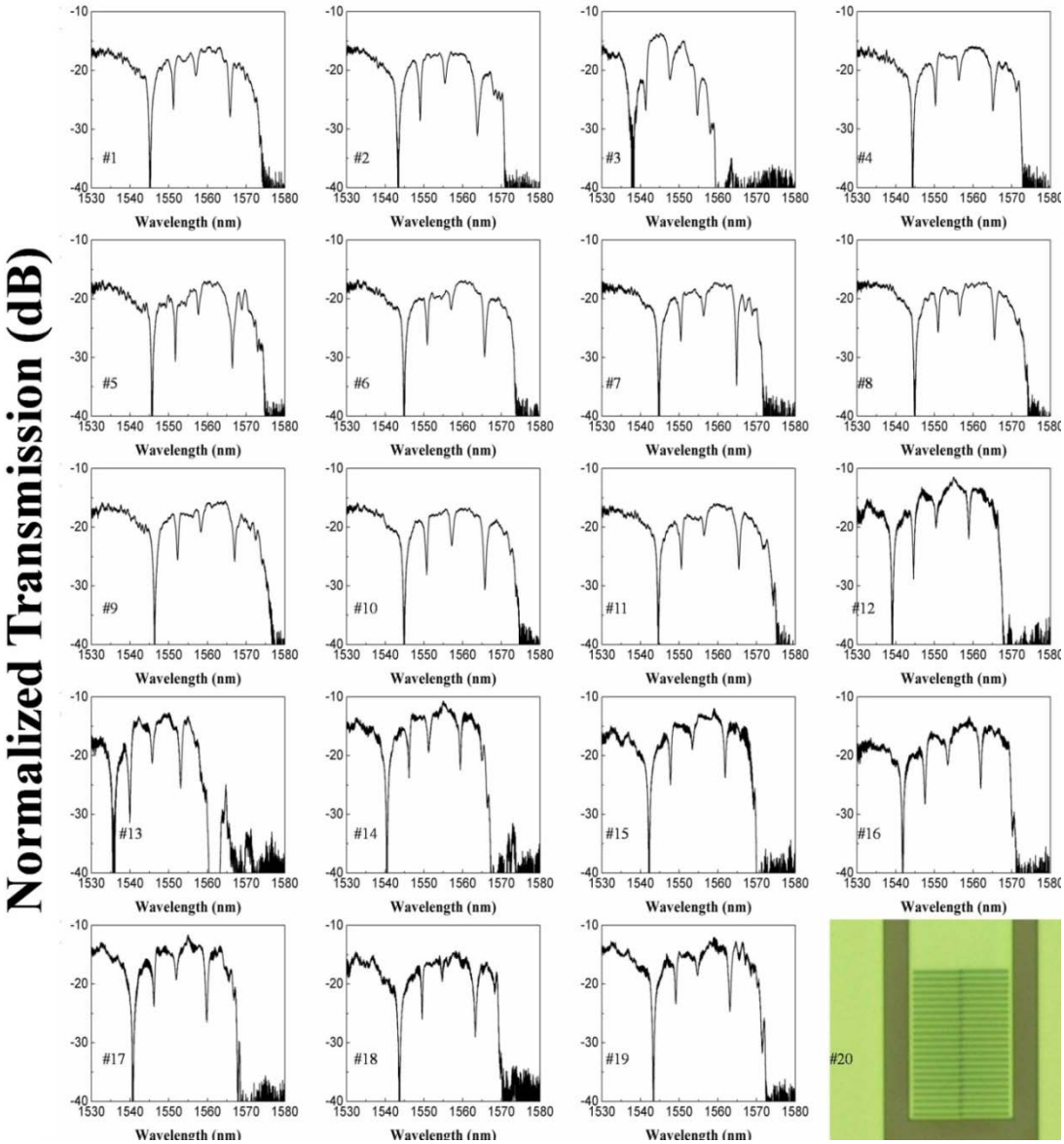


Figure 2.4 Experimental transmission spectra in water of 19 devices comprising W1 PCW coupled to L13 PC microcavities. Extreme right bottom inset shows microscope image of stitching observed on 20$^{th}$ device.

Ten L21 devices are fabricated on a chip and characterized under water and glycerol. Nine out of ten devices provide similar output power at 1550nm as well as good waveguide transmission spectrum characteristics with sharp resonance peaks as observed in Fig. 2.5(a). The transmission from the $10^{th}$ device shows lower output power as in Fig. 2.5(b) and several Fabry-Perot type resonance modes are seen in the transmission spectrum in Fig. 2.5(c) superimposed with the L21 PC microcavity resonance modes. We believe that the transmission characteristics of Device 5 are contributed by a defect on the stripe waveguide section, as shown in the SEM image in Fig. 2.5(d). For all working devices, the absolute wavelength positions of all the resonant modes and band edges are nearly same and the slight difference may be due to fabrication fluctuations or the different thicknesses of the SOI wafer at the specific location of the photonic crystal pattern on the SOI wafer.

A close examination of the L21 PC microcavity spectra in Fig. 2.5(a) indicates that the resonance closest to the transmission band edge is missing from Devices 2 and 8. The missing mode is labeled A in the L21 spectrum shown in Device 1 in Fig. 2.5(a). For each of devices 2 and 8, it is also observed that the quality factor of mode C is also reduced. However, quality factors of modes B and D in devices 2 and 8 are similar to the Q in other devices in Fig. 2.5(a) where mode A is observed. The electric field intensity profiles of modes A, B, C and D for the L21 PC microcavity are calculated using RSoft 2D BandSolve and shown in Figs. 5(e). While no visual confirmation could be achieved from a top view SEM image of the L21 PC microcavities in devices 2 and 8, an examination of the mode field profile suggests that fabrication induced variations could exist in the region of the air holes in the immediate vicinity of the photonic crystal microcavity within the red dashed square demarcated in Mode B in Fig. 2.5(e), the

dashed region being the only region common to both modes A and C, where modes B and D have low electric field intensities.

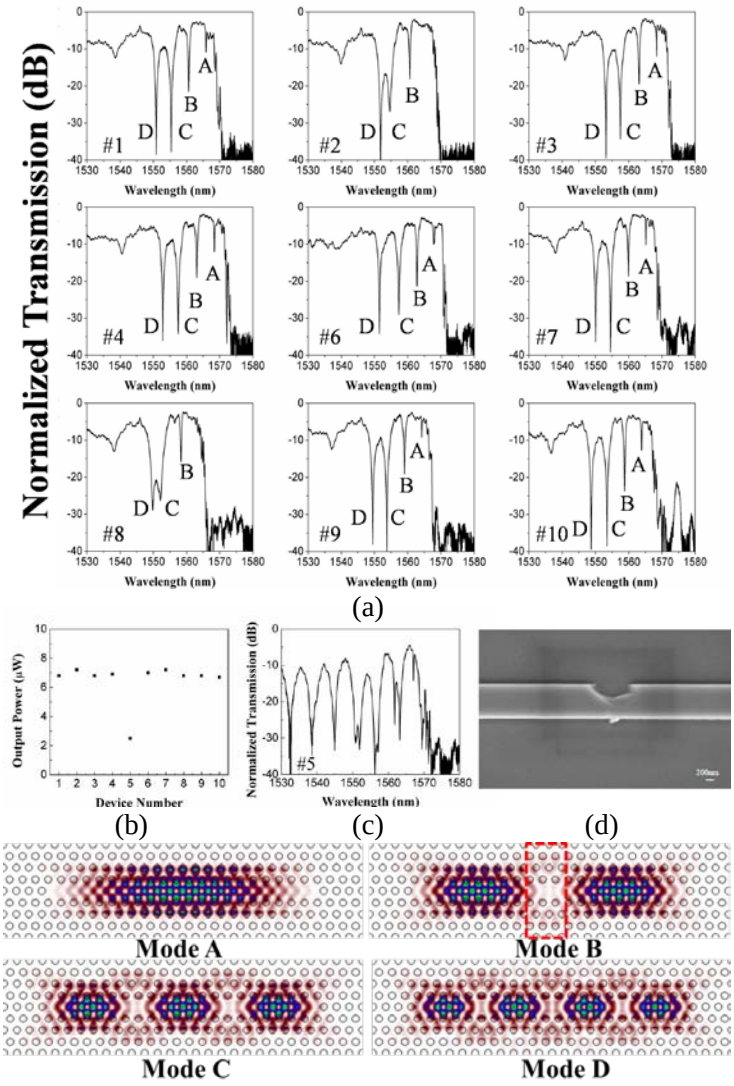


Figure 2.5 (a) Experimental transmission spectra in glycerol of 9 out of 10 devices comprising W1 PCW coupled to L21 PC microcavities. (b) Output power of all ten L21 devices, (c) transmission spectrum of L21 device #5 (d) SEM image of defect on ridge waveguide section at the input of PCW in Device 5. (e) Electric field intensity profiles of the resonant modes A, B, C and D in (a).

Fig. 2.6(a) and 2.6(b) shows the distribution of Q in water for all L13 and L21 devices investigated in Figs. 2.4 and 2.5 respectively. For L21 devices, excluding devices #2, #5 and #8, a narrow distribution of Q (7,300 +/- 500) and a narrow distribution of absolute wavelength of the resonance mode A (+/- 2nm) is observed. For L13 devices, we exclude devices #3, #7 and #13, in addition to #20, since extremums are observed in one or both of Q and absolute wavelength position. For the remaining devices, the distribution of Q is (5,300 +/- 1200) while the variation in absolute wavelength position is +/-4nm. We note here that the Q~5300+/-1200 observed in water in L13 PC microcavities in the present devices with 250nm silicon device layer is lower than Q~13,000 previously demonstrated with SOI devices with 230nm device silicon capped by 20nm SiO2. [23]

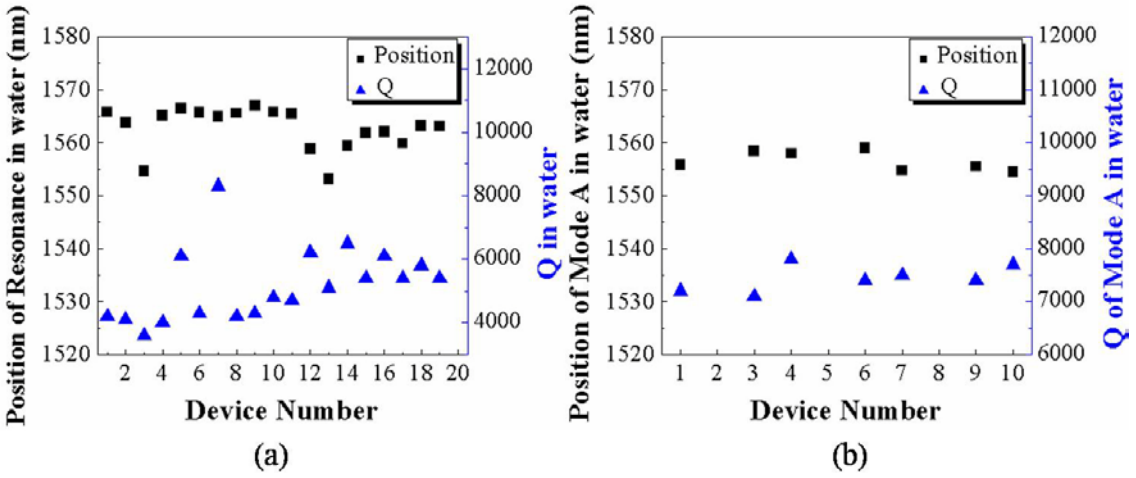


Figure 2.6 Distribution of Q and absolute wavelength position in water of resonance modes closest to the band edge for (a) L13 and (b) L21 PC microcavities in Fig. 2.4 and Fig. 2.5.

With respect to the absolute wavelength, it is to be noted that a distribution of +/- 5nm is allowable for these sensor structures since the intrinsic material absorption of silicon and the ambient PBS can be assumed to be nearly constant over this narrow wavelength range so as not to affect the Q appreciably. Also, the device operating principle requires the measurement of relative wavelength shift and hence the absolute wavelength variation within +/- 5nm can be tolerated. From considerations of purity of device transmission spectrum, resonance mode quality factor and absolute resonance wavelength position, the yields for L13 and L21 devices are thus 80% and 70% respectively.

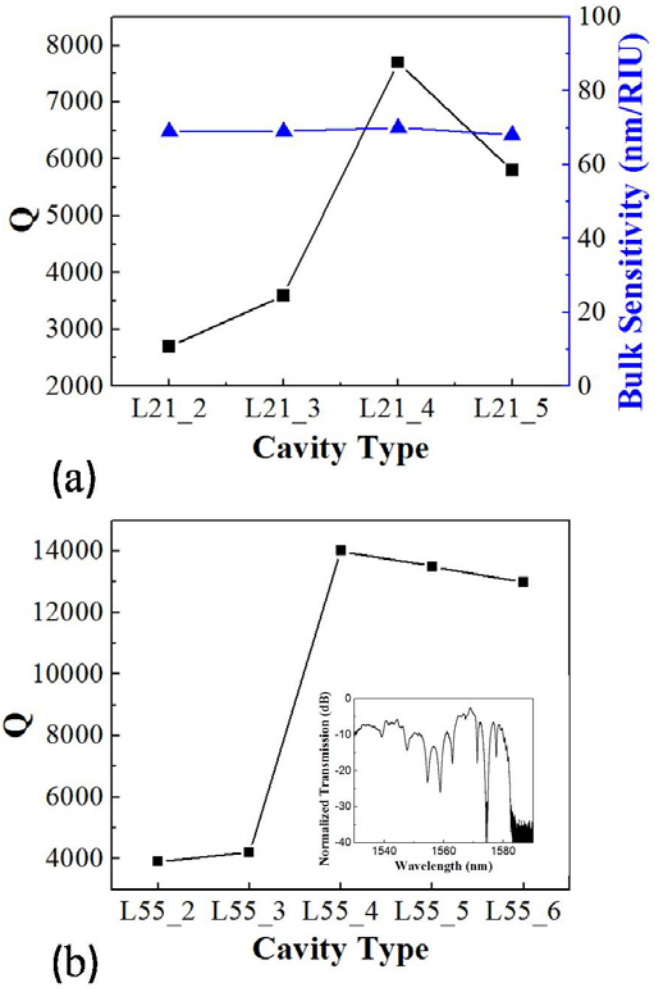


Figure 2.7 Q-factors (black squares) and bulk sensitivity (blue triangles) variation of (a) L21 microcavity side coupled to W1 PCW in water versus microcavity location change (L21_2 represents L21 microcavity 2 rows away from the PCW) and (b) L55 microcavity side coupled to W1 PCW in water versus microcavity location change. The inset is the transmission spectrum of L55 with cavity located 4 rows away from the PCW.

As discussed in Section 2, the loss from the PC microcavity into the PCW plays a critical role in the total loss of the PC microcavity, and contributes a term $Q_{WG}$ to

Equation 3. Since $Q_{WG}$ is primarily determined by the number of periods between the PC microcavity and the PCW, we fabricated devices in which the L21 PC microcavity is located 2, 3, 4 and 5 rows away from the PCW. Fig. 2.7(a) shows the experimental Q ($=\lambda/\Delta\lambda$).

As the L21 PC microcavity moves away from the PCW, Q increases indicating reduced cavity to waveguide loss and improved optical confinement by the photonic crystal microcavity. At the same time, the normalized frequency of the resonance mode increases as the dielectric fraction in the vicinity of the PC microcavity decreases as it moves away from the PCW. From the dispersion diagram in Fig. 2.2(b), a higher normalized frequency implies more radiation loss as a greater fraction of the optical mode is above the light line, which will decrease $Q_R$. $Q_i$ will also decrease as the PC microcavity moves further away from the W1 PCW due to the increased mode overlap with surface roughness of more surrounding holes.

A limiting situation is reached when the PC microcavity is located more than 4 rows away from the PCW. The increase of $Q_R$ and $Q_i$ dominate over the increase in $Q_{WG}$ and hence the effective $Q_T$ decreases. Since the loss rate from the cavity to the waveguide and vice-versa is directly proportional to the cavity length, the highest Qs will be achieved at different distance of the cavities from the PCW for cavities of different lengths such as L13 and L21. The L13 PC microcavities in Fig. 2.4 were considered 2 rows away laterally from the W1 PCW. For our L21 PC microcavity, it is observed that when the PC microcavity is located 4 rows away from the PCW, Q reaches a maximum. The Q of a L21 PC microcavity located 2 rows away from the W1 PCW (Q~2,500) is lower than the Q of a L13 PC microcavity located 2 rows away from the W1 PCW. Hence, a simple increase of the cavity length does not increase Q; other factors such as

the cavity-waveguide coupling determined by $Q_{WG}$ need to be engineered. The bulk sensitivities of the L21 PC microcavity devices shown in Fig. 2.7 (a), change negligibly as the L21 PC microcavity is moved away from the W1 PCW, since the mode volume of the microcavity changes negligibly as the cavity is moved farther away from the W1 PCW. However, a larger Q enables smaller changes in analyte concentration to be accurately measured.

A similar effect is observed with a L55 type PC microcavity with 55 missing holes along the length of a W1 PCW. L55 PC microcavity devices were fabricated with the microcavity located 2, 3, 4, 5, and 6 rows away from the PCW on one chip. As shown in Fig. 2.7 (b), the Q of the resonance closest to the transmission band edge varies and reaches a maximum (~14,000) when the PC microcavity is located 4 rows away from the W1 PCW. The inset shows the transmission spectrum of W1 PCW with L55 PC microcavity 4 rows away from the PCW.

### 2.3.3 Biosensing

To enable the biosensing experiments, the devices were first functionalized to enable receptor antibody/ protein immobilization on the silicon substrate. The biomolecule functionalization process has been described in detail in ref. [22]. 60μl target protein Avidin (67kDa) solution was directly dispensed from a micro-pipette. The diameter of the dispensed spot on silicon is around 8mm. During biosensing measurements, after each new addition of a new concentration of target protein, the device is washed three times in PBS before the effective resonance wavelength shift is measured in PBS. Experimental resonance transmission spectra observed when avidin binds to the probe biotin is shown in Fig. 2.8(a). The lowest concentrations are shown separately in Fig. 2.8(b) for clarity. In both Fig. 2.8(a) and 2.8(b), ripples observed are

due to Fabry-Perot effects which become larger as the resonance modes come closer to the transmission band edge due to the larger group index mismatch between the PCW and the ridge waveguides as shown in Fig. 2.2(b). Work is currently in progress to reduce the ripples in the resonance via advanced group index taper engineering.

At the lowest concentration of 1pM for L21 PC microcavity, which corresponds to 67pg/ml avidin, a resonance wavelength shift of 0.04nm was observed as shown in Fig. 2.8(b). In the L21 PC microcavity, (integrating over an area where the E-field intensity is more than 50% of the maximum value and including the entire internal surface area of the holes along the periphery of the photonic crystal microcavity in the Γ–K orientation where the E-field intensity is more than 50% over a fraction of the periphery of the hole) [30], from Fig. 2.2(b), the optical mode overlaps a surface area on the chip of 13.62$\mu m^2$. The actual real estate coverage of the optical mode on the chip is approximately 5.7$\mu m^2$ slightly larger than the L13 PC microcavity [22]. By assuming uniform surface coverage, the detection limit for surface density is 80fg/$mm^2$. Fig. 2.8(c) plots the resonant wavelength shift $\Delta\lambda$ as a function of concentration. As observed in Fig. 2.8(c), at the concentrations bigger than 100pM, binding sites of biotin are increasingly occupied by avidin and the resonance wavelength shift gradually saturated. To verify sensing repeatability, two identical L21 PC microcavity coupled PCW devices were fabricated and tested. Both show similar wavelength shift when different concentrations were added. These results further prove the measurement repeatability of L21 PC microcavity devices. A control experiment is done to verify that no resonance wavelength shift occurs in a control PC microcavity coated with BSA when different concentrations of avidin are introduced.

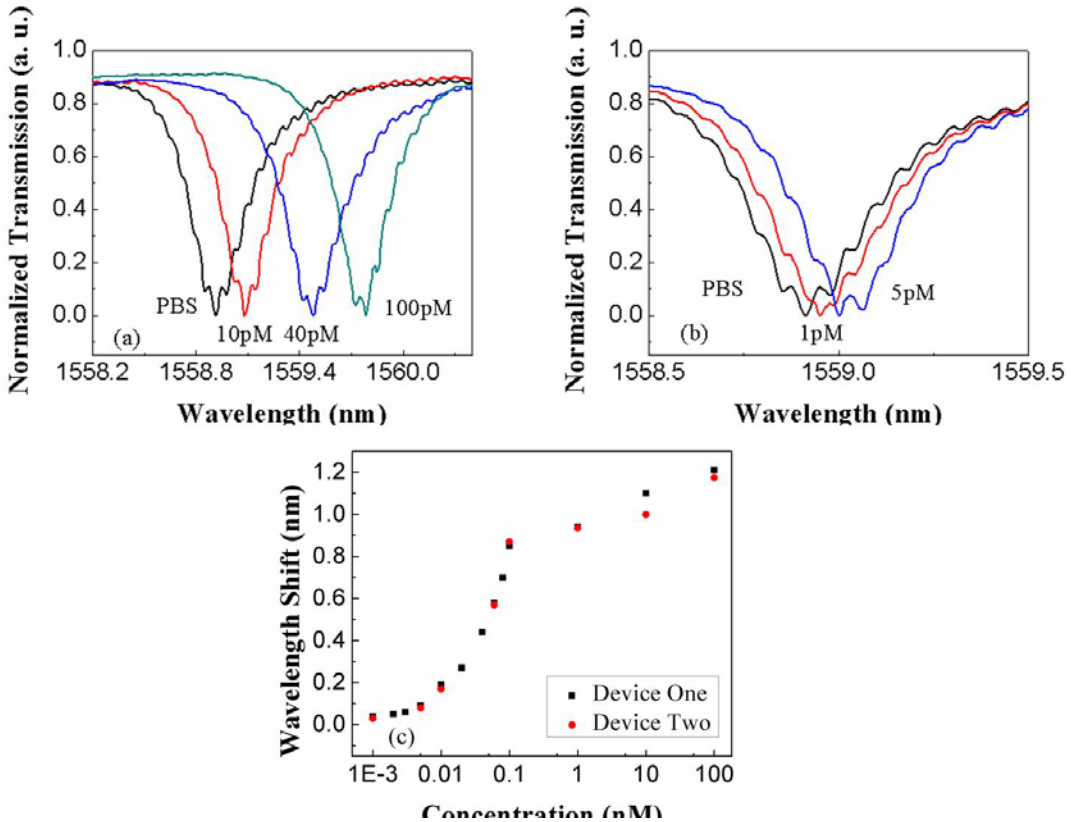


Figure 2.8 Experimental drop resonance spectra for the binding between Avidin to Biotin (Kd~$10^{-15}$M) (a) between 0pM to 100pM and (b) at the lower concentration range between 0pM and 5pM. (c) Experimental spectral shift for various concentrations of avidin binding to biotin in two L21 (red circles and black squares) PC microcavities.

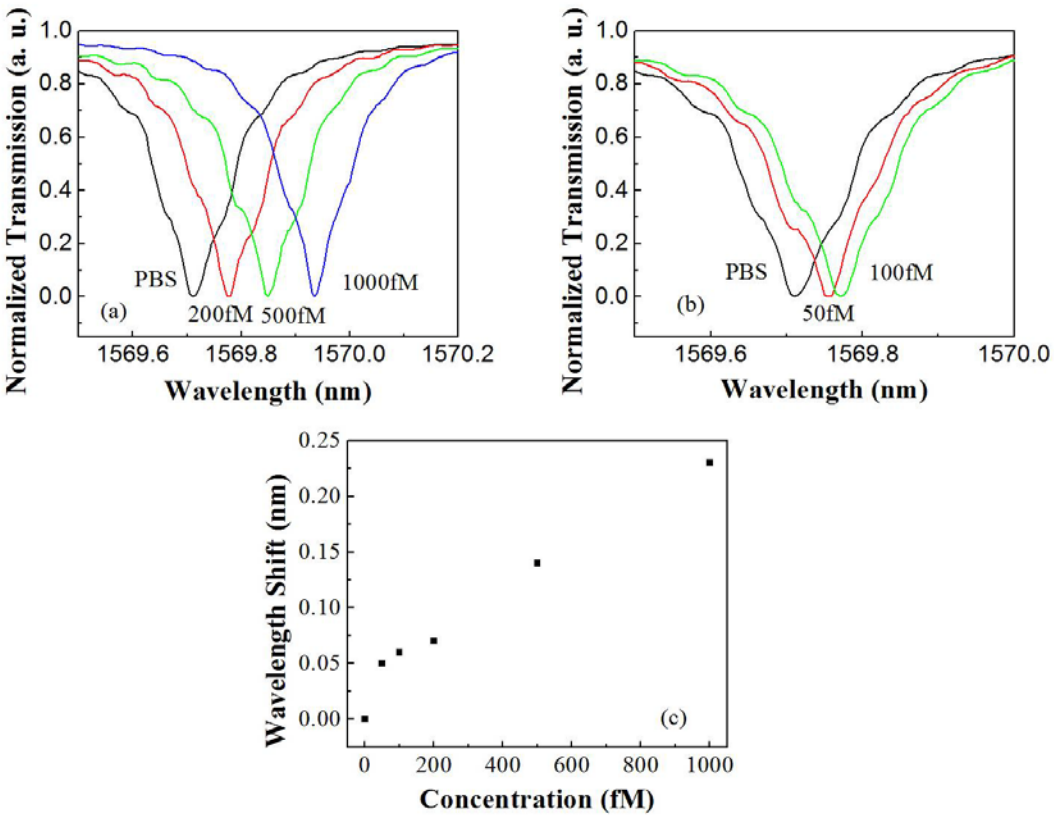


Figure 2.9 Experimental drop resonance spectra for the binding between Avidin to Biotin (Kd~$10^{-15}$M) on L55PC microcavity device (a) between 0fM to 1000fM and (b) at the lower concentration range between 0fM and 100fM. (c) Experimental spectral shift for various concentrations of avidin binding to biotin in L55 PC microcavities.

The L55 PC microcavity has a larger mode volume and thus a larger sensing area. The L55 cavity length is approximately 23 μm, which is less than the 35 μm drop size of the inkjet-printed probe protein. The biosensing on this device followed the same procedure as for L13 and L21 devices. The resonance wavelength spectral shift curves with different concentrations are shown in Figs. 9(a) and 9(b) for the L55 PC

microcavity. Fig. 2.9(c) shows the change in resonance wavelength as a function of concentration. We successfully detected avidin-biotin binding at the concentration of 50 femto-Molar (3.3pg/ml) with the L55 PC microcavity, , more than an order of magnitude better than L21.

The wavelength shifts observed in the control experiments are within 0.02nm, which is within the wavelength accuracy limit of our optical spectrum analyzer. Since $dn/dT$=1.87 × $10^{-4}$ at 295 K for silicon, the biomolecule sensing measurement limit of the shift $\Delta\lambda$ is 0.01 nm [23] which is lower than the accuracy limit of our optical spectrum analyzer. Hence there is no need for temperature compensation. Thus, in all experiments, resonance wavelength shifts greater than 0.02nm were considered as the signature of a binding event between the receptor capture biomolecule (biotin) and its specific conjugate (avidin).

## 2.4 DISCUSSIONS

### 2.4.1 Yield and quality comparison between end-fire coupling and grating coupling

As seen from Figs. 2.4 and 2.5(a), fabrication yield rate is greatly improved using SWG couplers in our devices. High quality spectral can be observed from all the working devices with clean curve, sharp resonances and high extinction ratio between pass band and band gap.

The SWG serves as a wave front scrambler and therefore an antireflection layer. The SWG destroys the wave front of incident light, reduces the reflection from SOI chip and the oblique incident angle also lowers the Fabry-Perot effects thereby greatly eliminating the fringes and enhancing the coupling efficiency into SOI chip. Secondly, the extinction ratio between pass band and band gap reduces quite a lot for end-fire coupling method compared with subwavelength grating coupler. While an external

polarization filter is employed in end-fire coupling, the polarization contrast between transverse electric (TE) and transverse magnetic (TM) of external filters determined the final polarization extinction ratio. In contrast, the SWG designed specifically for TE polarization appears to be an additional effective polarization filter and blocks the remaining TM polarized light from the incident fiber. Thus the final polarization extinction ratio is the product of polarization extinction ratios of the external filter and the SWG. Coupling light into PCWs through SWG couplers thus dramatically improves spectral quality and measurement yield of working devices, as noted in Fig. 2.6. Since the SWG couplers can be fabricated simultaneously with PCWs, there are no extra steps needed. No cleaving of waveguides is necessary as in end-fire coupling, which usually would require further post-processing such as polishing of facets for better yield. . SWGs therefore significantly improve the yield of devices with good spectral characteristics useful for biosensing experiments, which is the better measure of working device yield compared to just fabrication yield.

It may be argued that 30 devices are insufficient to reach a conclusion on yield. Yield information on photonic crystal devices is generally not reported in the literature; our own experience together with discussions with our research peers indicate that in general, yield of photonic crystal device is quite poor. Our yields of 80% by integrating SWG couplers with PC devices therefore represent significant milestone not only in PC biosensors but in PC based nanophotonics, in general. We believe the results can be easily validated in a commercial foundry with large sample size.

### 2.4.2 Comparison between L13 and L21 PC microcavity

The comparison of bulk sensitivity of L13 and L21 PC microcavities coupled to W1 PCW is shown in Fig. 2.10(a) and 2.10(b) respectively. Comparing the wavelength

shifts of the resonance mode in water and glycerol, the shift for L13 is 8.6nm (66nm/RIU), while the L21 shift is 9.6nm (74nm/RIU). The resonance modes of interest in these structures are the modes located closest to the band edge (mode A for L21 PC microcavity as in Fig. 2.6(a)).

For the L13 PC microcavity, as observed previously [22] the offset of the resonance mode from the band edge is around 6nm while for L21 the offset is approximately 4nm. Considering the same absolute normalized frequency of the transmission band edge in Fig. 2.2(b), a resonance mode located closer to the W1 PCW transmission band edge has lower fraction of radiation loss $P_R$. A longer L21 PC microcavity has more stored energy $W_E$ per unit volume than the L13 PC microcavity. A lower $P_R$ and higher $W_E$ both contribute to higher $Q_R$ for the L21 PC microcavity compared to the L13 PC microcavity. The L21 PC microcavity also has a larger optical mode volume than L13 which enables greater optical mode overlap with any analyte than in L13. It can be reasonably expected that $Q_i$ will be higher in L13 than in L21 due to the smaller optical mode volume which reduces the surface roughness scattering loss.

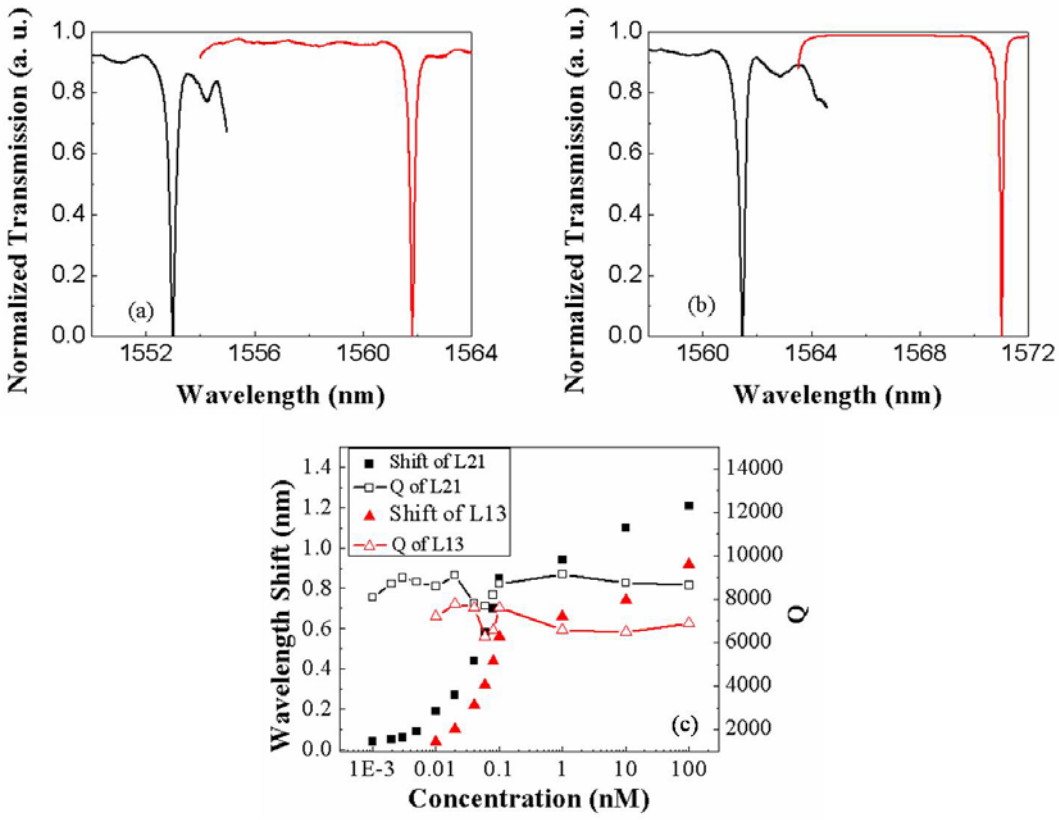


Figure 2.10 (a) Experimental spectra of (a) L13 and (b) L21 PC microcavities showing shift of resonance mode closest to the band edge in water (black) versus glycerol (red), (c) Experimental spectral shift for various concentrations of avidin binding to biotin in L13 (filled triangles) and L21 (filled squares) PC microcavities. Experimental Q variation for L13 (open triangles) and L21 (open squares) devices are also shown.

Finally, we consider that $Q_{WG}$ is inversely proportional to the length of the optical microcavity and directly proportional to the group velocity in the coupled W1 PCW. Both factors indicate a lower $Q_{WG}$ in L21 compared to L13 PC microcavities. The

lowering effect of $Q_{WG}$ was compensated by moving the L21 PC microcavity four rows away from the W1 PCW. Microcavity engineering thus resulted in resonances in L21 PC microcavities with Q~7,300+/-500 in water higher than Q~5300+/-1200 in L13 PC microcavities in addition to larger optical mode overlap with the analyte. As observed in Fig. 2.10(c), the Q of L21 PC microcavities is generally higher than that of L13 PC microcavities when measured as a function of increasing concentration of dispensed antibodies. The variation of Q in each case is within the range typically observed for both L13 and L21 PC microcavities. In addition, as shown in Fig. 2.2(b), the magnitude of slowdown factor in the coupled W1 PCW at the resonance mode frequency of interest is higher in L21 than in L13 PC microcavities, which also contributes to higher sensitivity [27]. The combined effects of higher Q, higher optical mode overlap and larger slow light effect in the coupled waveguide at the resonance frequency of interest, in L21 PC microcavities compared to L13 PC microcavities, leads to higher biosensing sensitivity in L21 compared to L13 as shown in the plot in Fig. 2.10(c) for different concentrations of avidin binding to receptor capture biotin.

A similar analysis was performed for L55 PC microcavities. The resonance mode of interest in the L55 PC microcavity is offset ~3nm from the transmission band edge compared to a 4nm offset of resonance A of the L21 PC microcavity. As a result, the group index of light in the propagating waveguide is even larger than in L21. Coupled with higher Q and higher optical mode overlap than L21, the L55 PC microcavity consequently experimentally demonstrated a lower detection limit. Table 1 summarizes the characteristic of three types PC microcavities discussed in this chapter.

Table 2.1 Comparison of different types of PC microcavities

| Microcavity Type | Detection Limit (Molar) | Q | Location of cavity (rows offset from PCW) | Yield |
|---|---|---|---|---|
| L13 | $10^{-11}$ | 5300+/- 1200 | 2 | 80% |
| L21 | $10^{-12}$ | 7300+/- 500 | 4 | 70% |
| L55 | $5\times10^{-14}$ | 14000+/-600 | 4 | N/A |

It can be anticipated that linear PC microcavities longer than L55 will have better sensitivity than 50 femto-molar demonstrated here experimentally. From the perspective of limitations due to ink-jet printed spot size with 35μm diameter, for maximum usage of a particular type of probe antibody that interacts with the trapped optical mode in the vicinity of the sensing microcavity in a multiplexed assay, the length can be increased to beyond 23μm of our L55 PC microcavity.

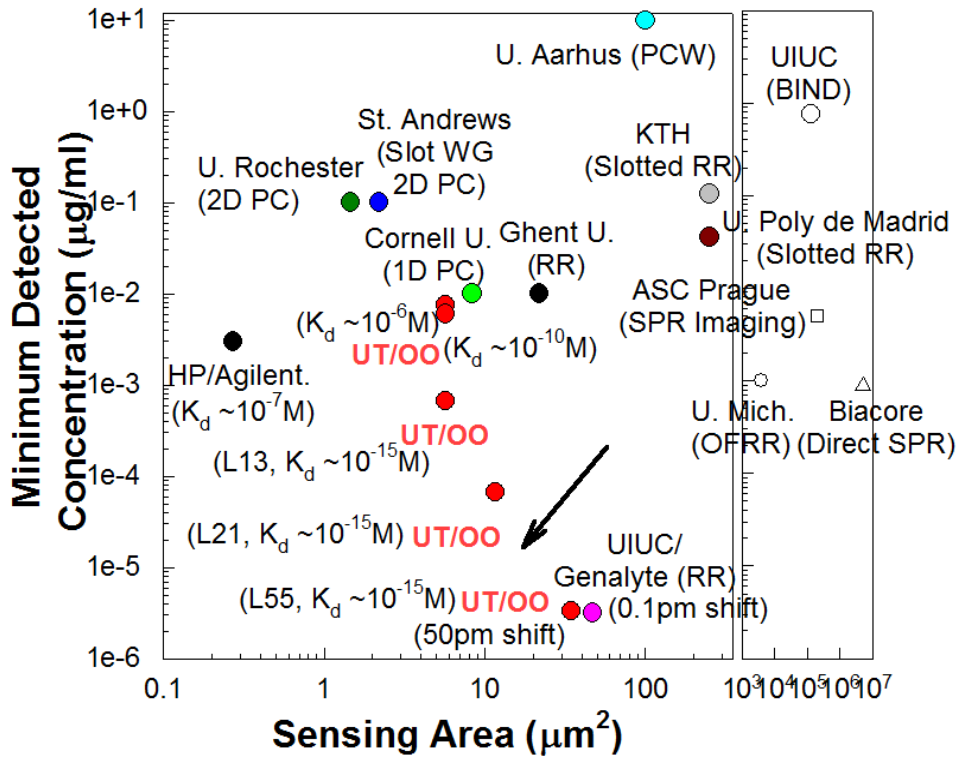


Figure 2.11 Comparison of minimum experimentally demonstrated detection limits versus other label-free optical platforms as a function of sensing area on chip. Red dots represent data obtained in our PC microcavity biosensors coupled to a W1 PCW.

In Fig. 2.11, we update the current status [22] of the minimum experimentally detected concentration of target biomolecules captured by a probe receptor, demonstrated in our PC microcavities side coupled to a W1 PCW, versus other label-free methods, including surface plasmon resonance devices [20], opto-fluidic ring resonators [31], ring resonator [18, 32, 33] and other photonic crystal (PC) devices [34, 35, 36, 37, 38], as function of sensing area. Compared to a 0.1pm shift observed with a 60fM concentration of streptavidin binding to biotin in a ring resonator with diameter 30μm [17], the 23μm

long L55 PC microcavity device demonstrated a 500 times larger resonance wavelength shift of 50pm for the binding of avidin to biotin. A recent demonstration of sub-attomolar detection with PC nanolasers in an InP platform is not considered due to its incompatibility with biological buffers with salt ions [39]. The sensing area of our device is smaller than other techniques such as nano-hole plasmonic arrays [40], or surface enhanced Raman scattering sensors [41] at equivalent detected concentrations, which essentially interrogate the signal over a large number of hot spots to achieve published sensitivities

## 2.5 Conclusion

In summary, we demonstrated an on-chip sensing system for high yield and high sensitivity biosensing combining subwavelength grating couplers and long linear PC microcavities side-coupled to a W1 PCW. In addition to high working device yields, of 80% for L13 devices and 70% for L21 devices, subwavelength grating couplers also significantly improve the quality of the resonance spectrum. The quality factor of L21 and L55 PC microcavities coupled to the W1 PCW was increased by engineering the cavity-waveguide coupling along with the length of the microcavity. We experimentally detected the binding of 1pM and 50 femto-molar concentration of avidin to its specific conjugate biotin in PBS for L21 and L55 devices respectively, more than one order of magnitude higher than our previous demonstration [22] and with higher sensitivity and larger miniaturization than other competing technologies. Device miniaturization is still retained from the context of practical engineering limitations of biomolecule patterning in a biosensing microarray.

## 2.6 REFERENCES


[1] T. Shoji, T. Tsuchizawa, T. Watanabe, K. Yamada, and H. Morita, "Low loss mode size converter from 0.3 μm square Si wire waveguides to single mode fibers," Electron. Lett., vol. 38, pp. 1669-1670, 2002.

[2] V. R. Almeida, R. R. Panepucci, and M. Lipson, "Nanotaper for compact mode conversion," Opt. Lett., vol. 28, pp. 1302-1304, 2003.

[3] K. K. Lee, D. R. Lim, D. Pang, C. Hoepfner, W-Y. Oh, K. Wada, L. C. Kimerling, K. P. Yap, and M. T. Doan, "Mode transformer for miniaturized optical circuits," Opt. Lett., vol. 30, pp. 498-500, 2005.

[4] S. J. McNab, N. Moll, and Y. A. Vlasov, "Ultra-low loss photonic integrated circuit with membrane-type photonic crystal waveguides," Opt. Express, vol. 11, pp. 2927 - 2939, 2003.

[5] D. Taillaert, F. Van Laere, M. Ayre, W. Bogaerts, D. Van Thourhout, P. Bienstman, and R. Baets, "Grating Couplers for Coupling between Optical Fibers and Nanophotonic Waveguides," Jpn. J. Appl. Phys., vol. 45, pp. 6071–6077, 2006.

[6] Y. Tang, Z. Wang, L. Wosinski, U. Westergren, and S. He, "Highly efficient nonuniform grating coupler for silicon-on-insulator nanophotonic circuits," Opt. Lett., vol. 35, pp. 1290–1292, 2010.

[7] G. Roelkens, D. Vermeulen, D. Van Thourhout, R. Baets, S. Brision, P. Lyan, P. Gautier, and J. M. Fedeli, "High efficiency diffractive grating couplers for interfacing a single mode optical fiber with a nanophotonic silicon-on-insulator waveguide circuit," Appl. Phys. Lett., vol. 92, pp. 131101-1-131101-3, 2008.

[8] F. Van Laere, G. Roelkens, M. Ayre, J. Schrauwen, D. Taillaert, D. Van Thourhout, T. F. Krauss, and R. Baets, "Compact and Highly Efficient Grating Couplers Between

Optical Fiber and Nanophotonic Waveguides," J. Lightwave Technol., vol. 25, pp. 151- 156, 2007.

[9] M. Antelius, K. B. Gylfason, and H. Sohlström, "An apodized SOI waveguide-to-fiber surface grating coupler for single lithography silicon photonics," Opt. Express, vol. 19, pp. 3592-3598, 2011.

[10] F. Li, L. Wu, T. Li, M. Dubinovsky, S. Tang, and Ray T. Chen, "Unidirectional surface-normal waveguide grating coupler for wafer-scale MCM interconnect," Proc. of the SPIE 3005, pp. 136-142, 1997.

[11] L. Liu, M. Pu, K. Yvind, and J. M. Hvam, "High-efficiency, large-bandwidth silicon-on-insulator grating coupler based on a fully-etched photonic crystal structure," Appl. Phys. Lett., vol. 96, pp. 051126-1-051126-3, 2010.

[12] R. Halir, P. Cheben, S. Janz, D.-X. Xu, Í. Molina-Fernández, and J. G. Wangüemert-Pérez, "Waveguide grating coupler with subwavelength microstructures," Opt. Lett., vol. 34, pp. 1408-1410, 2009.

[13] R. Halir, P. Cheben, J. H. Schmid, R. Ma, D. Bedard, S. Janz, D. X. Xu, A. Densmore, J. Lapointe, and ´I. Molina-Fern´andez, "Continuously apodized fiber-to-chip surface grating coupler with refractive index engineered subwavelength structure," Opt. Lett., vol. 35, pp. 3243–3245, 2010.

[14] C. Xia and H. K. Tsang, "Nanoholes grating couplers for coupling between silicon-on-insulator waveguides and optical fibers," IEEE Photonics Journal, vol. 1, pp. 184- 190, 2009.

[15] X. Xu, H. Subbaraman, J. Covey, D. Kwong, A. Hosseini, and R. T. Chen, "Complementary metal–oxide–semiconductor compatible high efficiency subwavelength grating couplers for silicon integrated photonics," Appl. Phys. Lett., vol. 101, pp. 031109-1-031109-3, 2012.

[16] H. Subbaraman, X. Xu, J. Covey, and R. T. Chen, "Efficient light coupling into in-plane semiconductor nanomembrane photonic devices utilizing a sub-wavelength grating coupler," Opt. Express, vol. 20, pp. 20659-20665, 2012.

[17] M. Iqbal, M. A. Gleeson, B. Spaugh, F. Tybor, W. G. Gunn, M. Hochberg, T. Baehr-Jones, R. C. Bailey, and L. C. Gunn, "Label-free biosensor arrays based on silicon ring resonators and high-speed optical scanning instrumentation," IEEE J. Sel. Top. Quant. Electron., vol. 16, pp. 654-661, 2010.

[18] C. F. Carlborg, K. B. Gylfason, A. Kazmierczak, F. Dortu, M. J. Banuls Polo, A. Maquieira Catala, G. M. Kresbach, H. Sohlstrom, T. Moh, L. Vivien, J. Popplewell, G. Ronan, C. A. Barrios, G. Stemme, and W. van der Winjgaart, "A packaged optical slot-waveguide ring resonator sensor array for multiplex label-free assays in labs-on-chips," Lab Chip, vol. 10, pp. 281-290, 2010.

[19] A. Densmore, M. Vachon, D. X. Xu, S. Janz, R. Ma, Y. H. Li, G. Lopinski, A. Delage, J. Lapointe, C. C. Luebbert, Q.Y. Liu, P. Cheben, and J.H. Schmid, "Silicon photonic wire biosensor array for multiplexed real-time and label-free molecular detection," Opt. Lett., vol. 34, pp. 3598 -3600, 2009.

[20] H. Sipova, S. Zhang, A. M. Dudley, D. Galas, K. Wang, and J. Homola, "Surface plasmon resonance biosensor for rapid label-free detection of microribonucleic acid at subfemtomole level," Anal. Chem., vol. 82, pp. 10110-10115, 2010.

[21] B. S. Song, S. Noda, T. Asano and Y. Akahane, "Ultra-high-Q photonic double heterostructure nanocavity", Nat. Mater., vol. 4, pp. 207-210, 2005.

[22] S. Chakravarty, Y. Zou, W. Lai, and R. T. Chen, "Slow light engineering for high Q high sensitivity photonic crystal microcavity biosensors in silicon," Biosens. Bioelectron., vol. 38, pp. 170-176, 2012.

[23] W. C. Lai, S. Chakravarty, Y. Zou and R. T. Chen, “Silicon nano-membrane based photonic crystal microcavities for high sensitivity bio-sensing,” Opt. Lett., vol. 37, pp. 1208-1210, 2012.

[24] Y. Zou, S. Chakravarty, W. Lai, C. Lin and R. T. Chen, “Methods to array photonic crystal microcavities for high throughput high sensitivity biosensing on a silicon-chip based platform,” Lab Chip, vol. 12, pp. 2309-2312, 2012.

[25] P. Yeh, A. Yariv, and C.-S. Hong, “Electromagnetic propagation in periodic stratified media. I. General theory,” J. Opt. Soc. Am., vol. 67, pp. 423-438, 1977.

[26] S. M. Rytov, “Electromagnetic properties of a finely stratified medium,” Sov. Phys. JETP, vol. 2, pp. 466-475, 1956.

[27] W-C. Lai, S. Chakravarty, Y. Zou, and R.T. Chen, “Slow light enhanced sensitivity of resonance modes in photonic crystal biosensors,” Appl. Phys. Lett., vol. 102, pp. 041111-1-041111-4, 2013.

[28] C. Y. Lin, X. Wang, S. Chakravarty, B. S. Lee, W. C. Lai, and R. T. Chen, “Wideband group velocity independent coupling into slow light silicon photonic crystal waveguide,” Appl. Phys. Lett., vol. 97, pp. 183302-1-183302-3, 2010.

[29] S. A. Schulz, L. O'Faolain, D. M. Beggs, T. P. White, A. Melloni, and T. F. Krauss, “Dispersion engineered slow light in photonic crystals: a comparison,” J. Opt., vol. 12, pp. 104004-1-104004-10, 2010.

[30] D. Dorfner, T. Zabel, T. Hürlimann, N. Hauke, L. Frandsen, U. Rant, G. Abstreiter, and J. Finley, “Photonic crystal nanostructures for optical biosensing applications,” Biosens. Bioelectron., vol. 24, pp. 3688–3692, 2009.

[31] H. Li, and X. Fan, “Characterization of sensing capability of optofluidic ring resonator biosensors,” Appl. Phys. Lett. Vol. 97, pp. 011105, 2010.

[32] C. A. Barrios, “Optical Slot-Waveguide Based Biochemical Sensors,” Sensors vol. 9, pp. 4751–4765, 2009.

[33] K. De Vos, I. Bartolozzi, E. Schacht, P. Bienstman, and R. Baets, “Silicon-on-insulator microring resonator for sensitive and label-free biosensing,” Opt. Express vol. 15, pp. 7610–7615, 2007.

[34] M. Lee, and P. M. Fauchet, “Two-dimensional silicon photonic crystal based biosensing platform for protein detection,” Opt. Express vol. 15, pp. 4530–4535, 2007.

[35] C. Kang, C. T. Phare, Y. A. Vlasov, S. Assefa, and S. M. Weiss, “Photonic crystal slab sensor with enhanced surface area,” Opt. Express vol. 18, pp. 27930-27937, 2010.

[36] S. Mandal, and D. Erickson, “Nanoscale optofluidic sensor arrays,” Opt. Exp. vol. 16, pp. 1623–1631, 2008.

[37] M. G. Scullion, A. Di Falco, and T. F. Krauss, “Slotted photonic crystal cavities with integrated microfluidics for biosensing applications,” Biosens. Bioelectron. vol. 27, pp. 101-105, 2011.

[38] S. Zlatanovic, L. W. Mirkarimi, M. M. Sigalas, M. A. Bynum, E. Chow, K. M. Robotti, G. W. Burr, S. Esener, and A. Grot, “Photonic crystal microcavity sensor for ultracompact monitoring of reaction kinetics and protein concentration,” Sensors and Actuators B, vol. 141, pp. 13–19, 2009.

[39] S. Hachuda, S. Otsuka, S. Kita, T. Isono, M. Narimatsu, K. Watanabe, Y. Goshima, T. Baba, “Selective detection of sub-atto-molar streptavidin in 1013-fold impure sample using photonic crystal nanolaser sensor”, Opt. Express, vol. 21 iss. 10, pp. 12815-12821, 2013.

[40] T-Y. Chang, M. Huang, A. A. Yanik, H-Y Tsai, P. Shi, S. Aksu, M. F. Yanik and H. Altug, “Large-Scale Plasmonic Microarrays for Label-Free High-Throughput Screening,” Lab Chip vol. 11, pp. 3596-3602, 2011.

[41] Z. Chen, S. M. Tabakman, A. P. Goodwin, M. G. Kattah, D. Daranciang, X. R. Wang, G. Y. Zhang, X. L. Li, Z. Liu, P. J. Utz, K. L. Jiang, S. S. Fan and H. J. Dai, “Protein microarrays with carbon nanotubes as multicolor Raman labels,” Nat. Biotechnol., vol. 26, pp. 1285–1292, 2008.

# Chapter 3: Methods to array photonic crystal microcavities for high throughput high sensitivity biosensing on a silicon-chip based platform[2]

## 3.1 INTRODUCTION

Microarrays provide an unprecedented opportunity for comprehensive concurrent analysis of thousands of biomolecules such as proteins [1], genes, DNA molecules, small molecules or nucleic acids. The global analysis of the response to a toxic agent, as opposed to the traditional method of examining a few select biomolecules, provides a more complete picture of toxicologically significant events. In proteomics studies for the detection of various infectious diseases and cancers, microarrays have been used ubiquitously. The measurement throughput in such methods is however low due to the necessity to measure each sensor spot separately with an individual detector, which also increases the detection antibody requirement as well as the sample volume needed for measurement.

Label-free biosensors are particularly attractive since they avoid complex chemistries caused by steric hindrance of the labels. All methods of detection transduce the specific binding of the biomolecule of interest to its specific conjugate biomolecule receptor bound to the device substrate, into an electrical, mechanical or optical signal. Optical detection techniques are generally preferred due to their freedom from

---

[2] Y. Zou, et. al., Lab on a Chip 12, 2309-2312 (2012).

Y. Z. designed, fabricated the device, performed the experiments, analyzed the data, wrote the manuscript; S. C. designed the PC device, analyzed the data, and revised the manuscript; W. L. helped prepare Avidin solution; C.Y. Lin helped draw the pattern. R. T. C. oversaw all research phases and revised the manuscript. All authors discussed and commented on the manuscript.

electromagnetic interference. While several platforms based on ring resonators [2,3], wire waveguides [4] and surface plasmon resonance (SPR) [5] have been investigated. Photonic crystal (PC) microcavities [6], in general, are more compact (of the order of a few square microns in surface area) and have higher sensitivity than other devices due to slow light effect and a larger optical mode overlap with the analyte within compact optical mode volume. Recent research has shown that PC biosensors have biomolecular surface mass density detection limit of 22 pg $mm^{-2}$ which compares quite favorably with detection limits of 1pg $mm^{-2}$ in SPR on almost four orders of magnitude smaller surface area [7]. In contrast to conventional notion of trying to achieve the smallest possible PC microcavity for sensing purposes, we showed that a slightly longer PC microcavity can deliver significantly improved performance both in terms of higher sensitivity as well the ability to detect small changes in concentration. Increasing the length of the PC microcavities reduced the radiation loss, which scales inversely with the cavity length, thereby reducing the resonance linewidth and thus increasing the ability to detect small changes in concentration. Furthermore, the slightly increased length enables larger overlap of the optical mode with the analyte leading to higher sensitivity. The increased length of the PC microcavities is not a drawback in terms of chip scale miniaturization, since a primary requirement in such hybrid architectures is the need to functionalize the resonators with target receptor biomolecules that will bind specifically to their probe biomolecule conjugates in a diagnostic assay. The ink-jet printed target receptor spot size we achieved is about 35 μm in diameter [7], which thus determines the minimum spacing that can be achieved between adjacent resonators functionalized with different unique target receptor biomolecules in a chip-integrated diagnostic microarray. In addition, much of the research in the literature concerns single PC microcavity biosensors. Methods to array two dimensional PC microcavities have primarily focused on the detection of a

single biomolecular probe binding to its specific conjugate target biomolecule on all microcavities [8].

In this chapter, we demonstrate the high sensitivity of long PC microcavities. We also demonstrate two methods to array these PC microcavities, which can be combined to create large chip-integrated microarrays in which all PC microcavity sensors, each coated with a different biomolecule target receptor, can be simultaneously interrogated with the same small quantity of probe sample, resulting in high throughput diagnostic assays. All devices are demonstrated in a silicon-on-insulator (SOI) platform, which also guarantees higher fabrication yield, more robust devices, and demonstrates better performance characteristics than the best devices demonstrated to date in the PC platforms on freestanding membranes.

## 3.2 Device Design

Fig. 3.1(a) shows the schematic of the test system on chip (SoC), where individual components are clearly shown. On each output arm of the 1 × 4 multi-mode interference (MMI) studied here, photonic crystal (PC) microcavities are arrayed along the length of a single photonic crystal waveguide (PCW). The test SoC we designed and then fabricated has one PC microcavity on three arms. On the fourth arm, two PC microcavities are arrayed along the length of one PCW. The scanning electron micrograph (SEM) of the key sections is shown in Fig. 3.2(a) which consists of a 1 × 4 MMI optical power splitter which splits the input light from a ridge waveguide into four output channels.

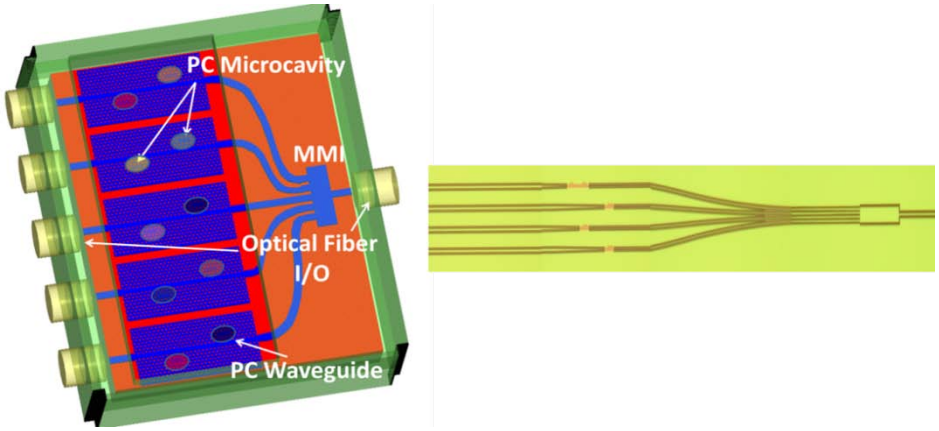


Figure 3.1 (a) Generalized schematic of the test system on chip with integrated 1×x MMI and PC microcavities coupled to PC waveguides. On each of the x output arms of the MMI, multiple PC microcavities are arrayed. Each microcavity is coated with a different target receptor biomolecule, each responsive to its specific conjugate, as indicated by a different color. (b) Stitched microscope image of 1×4 MMI device studied here.

The MMI was simulated by two-dimensional beam propagation method using RSoft's BeamProp software using design rules laid down previously [9]. The simulation result is shown in Fig. 3.2(b). The length and width of the MMI were designed as 123 μm and 16 μm respectively. Each of the input and output waveguide arms after the 1 × 4MMI is 2.5 μm wide and the output waveguides are separated by 1.5 μm. The output arms of the MMI are numbered as shown in Fig. 3.2(a). The PCW is a W line defect waveguide with uniform lattice constant a = 400 nm, where W1 denotes that width of the PCW is $\sqrt{3}$(a). Silicon slab thickness and air hole diameter are h = 0.58a and d = 0.54a.

Since the ink-jet spot size is 35 μm in diameter, we are pursuing optimized designs investigating sensitivity versus increasing size of the PC microcavity. We have shown earlier that L13 PC microcavities with dimensions ~5.5 μm × 0.5 μm, not only have high sensitivity due to overlap of the confined optical mode with more air holes along the periphery of the PC microcavity but also have high quality factor (Q-factors), Q ≈26 760, which enables the detection of smaller changes in concentration.7 Linear L13 PC microcavities with 13 missing holes along Γ–K direction, as shown in Fig. 3.3(a), are fabricated two periods away from the PCW. On arms 1–3, the edge air holes on the axis of the PC microcavity are shifted outward [10] in the Γ–K direction by 0.15a. Shifts beyond 0.15a lead to fabrication challenges with adjacent holes. The mode profile of the resonant mode of interest, as described in Ref. 7, is shown in Fig. 3.3(b).

On arm 4, both PC microcavities are of the specially designed L13 type. In the PC microcavity labeled A, the edge air-holes are shifted in the Γ–K direction inward by 0.05a. In the other PC microcavity labeled B, the edge air-holes are shifted outward in the Γ–K direction by 0.15a. The inward shift of 0.05a causes the resonant mode to interact more with the edge holes along the axis, thus pulling the resonance up in frequency [10]. The design leads to resonant modes from the two series-arrayed microcavities on the same PCW that are separated by wavelength. The spacing of 50 μm between the two microcavities ensures no crosstalk. As said previously, the spacing of 50 μm is not a drawback since we have shown earlier [7] that our Dimatix ink-jet printer achieved a minimum spacing of 50 μm between adjacent printed target antibodies that each covered a circular area with diameter 35 μm.

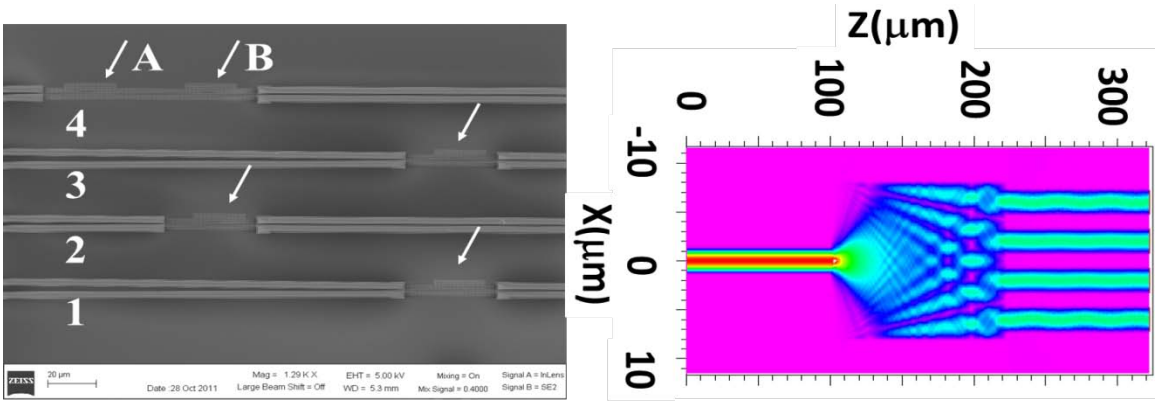


Figure 3.2 (a) SEM of PC devices on 4 arms of a 1×4 MMI (b) Simulation showing optical power distribution in 1×4 MMI.

### 3.3 DEVICE FABRICATION

Devices were fabricated on SOI wafer with 230nm top silicon layer and 3 $\mu$m buried oxide. 45nm thermal oxide was grown on top of silicon as etch mask for pattern transfer.PC waveguides, PC impedance tapers to minimize reflection loss, 1×4 MMI optical splitters and strip waveguides are patterned in one step with e-beam lithography followed by reactive ion etching.

To enable the biosensing function, the on-chip sensing sub-system (OCSS) was functionalized by treating with 10% by volume 3-aminopropyl-triethoxy-silane (3-APTES) in toluene. It is then washed 3 times in toluene to ensure complete removal of unbound 3-APTES, 3 times in methanol to remove toluene and finally 3 times in de-ionized water to remove methanol. The OCSS is then incubated in 1% glutaraldehyde in phosphate buffered saline (PBS) for 5 minutes and washed 3 times in PBS and ink-jet printed with target antibodies (Abs) in glycerol. Past research has shown that the 3-

APTES-glutaraldehyde coupled layer retains its initial activity for several weeks [11]. This negates any potential concern regarding time-dependent binding affinities of the target Abs, due to the time it takes to switch cartridges in our ink-jet printer. The printed spots were left to incubate overnight. Subsequently, all target Abs not bound to the functionalized device layer were removed by washing 3 times in PBS. The washing steps are completed in a few seconds, which ensures that unbound target Abs do not have sufficient time to bind to undesired areas to create any cross-talk. On arms #1 and #2 of the MMI as defined in Fig. 3.2, human IL-10 (Insight Genomics, Cat #: RP027) and rabbit anti-goat IgG (BioRad Labs, Cat. #: 172-1034) target Abs are dispensed on the PC microcavities within the OCSS. On arm #4, the PC microcavityB is printed with rabbit anti-goat IgGAbs. After overnight incubation and washing, the device is coated with bovine serum albumin (BSA) to prevent any non-specific binding and washed. The PC microcavity in arm #3 and the second PC microcavity Ain arm #4 are thus effectively covered with BSA and serve as control microcavities for biomolecule binding. The device is kept wet in PBS at all times.

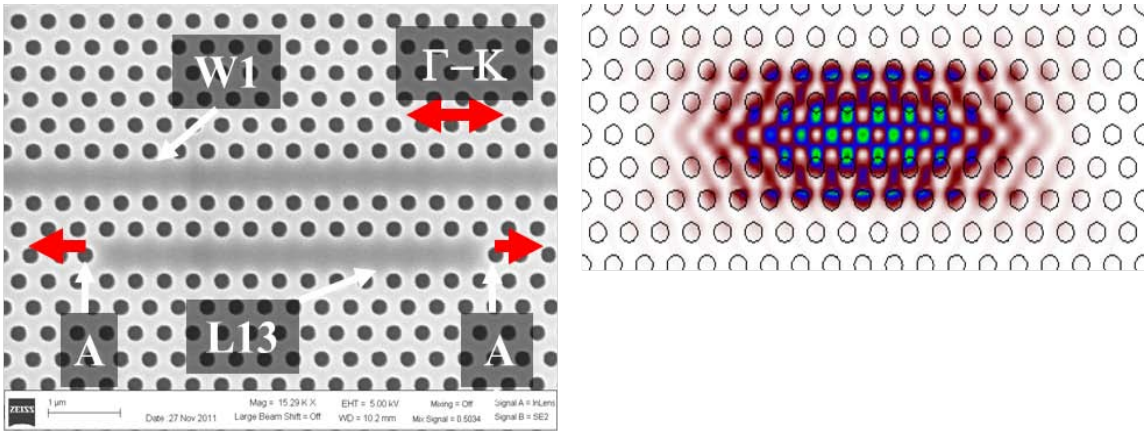


Figure 3.3 (a) SEM image of L13 PC microcavity adjacent to a W1 PCW. (b) Electric field intensity profile of the resonance mode of the L13 PC microcavity.

### 3.4 Device Characterization

Light is guided in and out of the PCW by ridge waveguides from the MMI with PC group index taper to enable high coupling efficiency into the slow light guided mode [12]. Devices were tested with TE-polarized light by end-fire coupling method with polarization maintaining single mode tapered lensed fibers. All probe Abs are introduced in PBS which forms the top cladding. When probe Abs that are specific to their conjugate target Abs on the different arms are introduced, the conjugate specific binding causes a change in the refractive index in the immediate vicinity of the corresponding PC microcavity leading to a change in resonance frequency and hence a shift in wavelength of the dropped resonance from the transmission spectrum of the PCW in the corresponding arm of the MMI. The magnitude of the shift gives a precise interpretation of the concentration of probe Abs.

The resonance spectrum of the L13 PC microcavity was first measured in PBS, functionalized with target receptor Abs. The transmission spectrum of the PCW with the coupled L13 PC microcavity is shown in Fig. 3.4(a). The resonance wavelength is at 1578.9nm, near the band edge at 1588nm, with approximately 12dB extinction ratio. The corresponding mode profile of the microcavity coupled resonance mode was shown in Fig. 3.3(b).

The resonance wavelength shift versus concentration of probe Abs on arms #1 and #2 were first separately characterized for different concentrations of rat anti-human IL-10 (Invitrogen, Cat #: RHC1K1001) (molecular weight MW=150kDa) and goat anti-rabbit IgG (Cat. #: 170-6515) probe Abs (MW=150kDa) and the results shown in Fig. 3.4(b).

Before a new addition of antibody solution carrying a different type of probe protein, the resonance wavelength was measured ($\lambda_1$). For each concentration of newly added probe antibody solution, the chip was incubated in the probe antibody solution and the resonance wavelength monitored as a function of time. No resonance wavelength shift was observed for 20 minutes. After 20 minutes, the resonance wavelength increased as a function of time, until the shift saturated after another 20 minutes at $\lambda_2$. The chip was next washed 3 times in PBS to remove unbound probe Abs and the resonance wavelength $\lambda_3$ ($<\lambda_2$) measured again. The final resonance wavelength shift $\Delta\lambda$, as plotted in Figs. 3.4(b) is given by $\Delta\lambda=\lambda_3-\lambda_1$.

A larger wavelength shift is observed in Fig. 3.4(b) with the probe Ab solution of rat anti-human IL-10 Abs than goat anti-rabbit IgG Abs. The difference in wavelength shifts for the two Abs is related to the lower dissociation constant $K_d$ of rat anti-human IL-10 Abs ($K_d \sim 10^{-10}$M) than goat anti-rabbit IgG ($K_d \sim 10^{-6}$M), the details of which are being submitted in a later publication.

A typical resonance shift upon specific binding for the high-Q L13 PC microcavity resonance of 0.1nM rat anti-human Abs to Human IL-10 Abs is shown in the inset of Fig. 3.4(b).

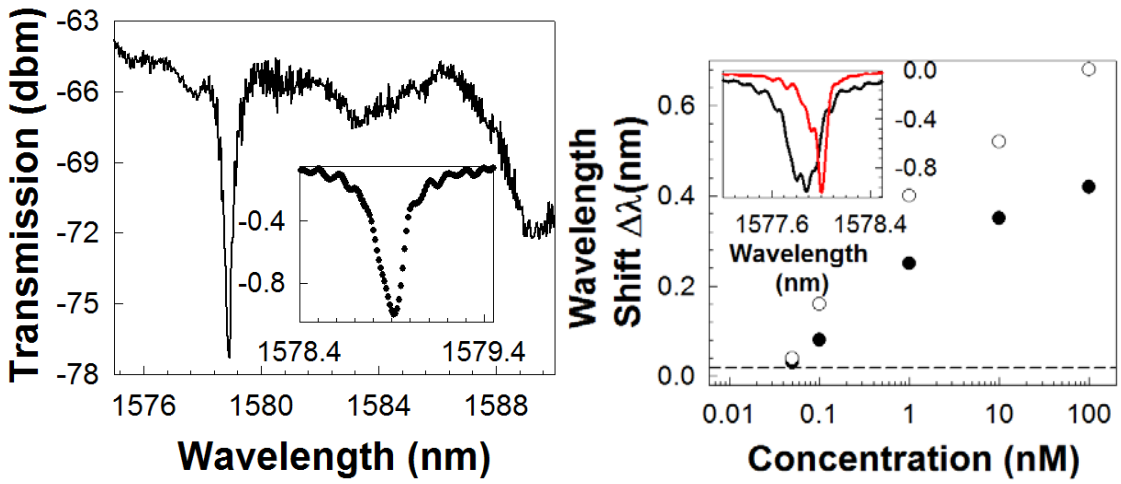


(a) (b)

Figure 3.4 (a) Transmission spectrum of W1 PCW with coupled L13 PC microcavity. (Inset) shows the normalized transmission, magnifying the wavelength range around the resonance. (b) Wavelength shift of the resonance shown by arrow in (a) as a function of concentration of probe antibodies, rat anti-Human IL-10 (open circles) and goat anti-rabbit IgG (filled circles). (inset) shows the spectral shift from black to red curve when 0.1nM of probe rat anti-Human IL-10 antibodies is added to a 0nM PBS background. Dashed line indicates detection limit.

The experimentally confirmed Q-factor is approximately 9,300. Our previous W1 coupled L7 PC microcavity device [7], with seven missing holes, in SOI structures had a Q-factor approximately 7,300. Q~9,300 represents the highest Q reported for bio-sensing in SOI PC devices. 60μl of probe Abs was directly dispensed from a micro-pipette. Note that only the probe Abs are dispensed with the micro-pipette, as in a diagnostic scenario where the sample will be directly dispensed on the microarray chip. The target receptor Abs was ink-jet printed. Based on dispensed spot diameter ~8mm, the L13 PC microcavities can thus detect binding of 7.5ng/ml of rat anti-human IL-10 probe Abs. From Fig. 3.3(b) inset, considering a sensing area ~11$\mu m^2$, (integrating over a surface where the E-field intensity is more than 50% of maximum value and including the inner surface area of peripheral holes) [7], and uniform surface coverage, the estimated detection limit, without considering unbound Abs that are washed away, in L13 devices is 98atto-grams for rat anti-human IL-10 probe Abs. In ref. [13], at a concentration of 0.67nM of probe biomolecules with Kd ~$6\times10^{-7}$M, the authors observed a resonance wavelength shift less than 0.05nm with resonances that had Q~300. In contrast, the interpolated resonance wavelength shift that would be observed in our L13 PC microcavity device (from Fig. 3.4) for biomolecules with $K_d$~$10^{-6}$ M is about 0.2nm. The diffusion limited time limit for sensing can be reduced in the future by choosing a smaller volume of dispensed probe solution and/or by incorporating a flow cell into our measurements.

The multiplexing experiment is performed with the device in Fig. 3.1. Results from each arm of the MMI are shown in Fig. 3.5(a)-(c). 60μl of 600nM of goat anti-rabbit IgG Abs in PBS is introduced which causes a resonance wavelength shift in arm #2 that is printed with its specific conjugate rabbit anti-goat IgG Abs. A similar shift is observed in the PC microcavity A in arm #4 of the MMI. No shift is observed in arm #1

which was printed with human IL-10 Abs, which is not specific to the introduced probe Abs or in arms #3 or in the PC microcavity B in arm #4 that was coated with BSA. Next, 60μl of 600nM of rat anti-human IL-10 Abs in PBS is introduced. A resonance wavelength shift is observed in arm #1 of the MMI that was printed with its specific target conjugate Human IL-10 Abs. No resonance wavelength shift is observed in the other arms. Fig. 3.5(d) shows the transmission spectrum of the W1 PCW in arm #4 of the MMI with the two coupled L13 microcavities with slightly different geometry as described earlier. The resonances corresponding to PC microcavities A and B are at 1565nm and 1573nm respectively. Fig. 3.5(d) shows the resonance wavelength shift observed in the W1 PCW in arm #4 in A at 1565nm when 1nM of probe goat anti-rabbit IgG Abs in PBS is added. No shift is observed in B at 1573nm.

Our current measurement setup can only measure one waveguide at a time; however one can couple outputs from all waveguides to a multi-core optical fiber to enable all measurements to be monitored simultaneously for high throughput bio-sensing.

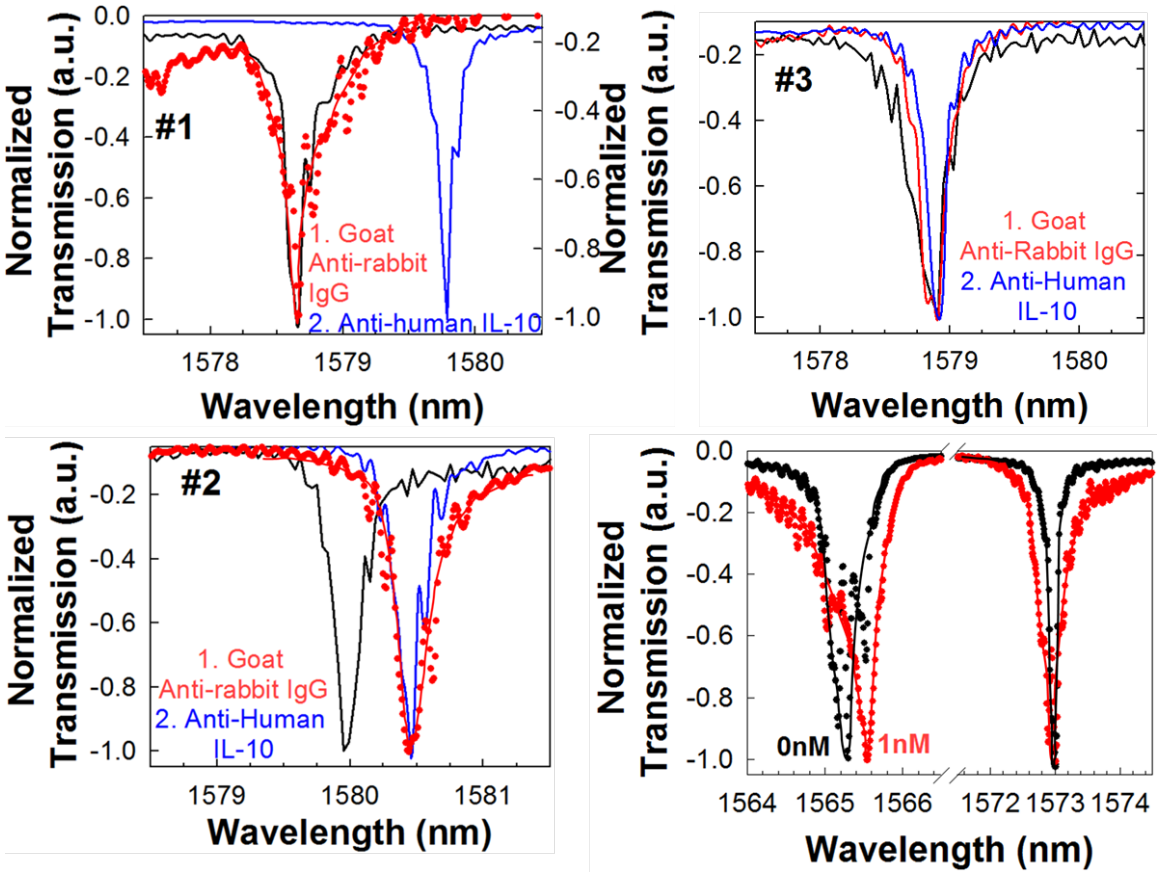


Figure 3.5 Resonance wavelength shift or none thereof observed in the (a)-(c) L13 PC microcavities in arms #1-#3 of the 1×4 MMI when probe antibodies goat anti-rabbit IgG in PBS and rat anti-human IL-10 in PBS are added in sequence and (d) arm #4 of the 1×4 MMI with 1nM of probe antibodies of goat anti-rabbit IgG in PBS.

## 3.5 Conclusion

In summary, we demonstrated an on-chip sensing subsystem for high throughput high sensitivity bio-sensing withMMI power splitters and multiple PC microcavities

coupled to PCWs. In addition to the highest Q observed in bio-ambient PBS with SOI-based PC microcavity devices, that enables higher accuracy, we observed more than an order of magnitude higher Q and four times larger resonance wavelength shift than previous demonstration [13]. The present demonstration interrogates five PC microcavities simultaneously, that recognize different specific binding interaction between target and probe antibody conjugates. Based on past designs [9], future devices will extend to larger arrays for simultaneous high throughput high sensitivity measurement that will benefit the microarray end-user community in diverse fields.

## 3.6 REFERENCES

[1] M. F. Templin, D. Stoll, J. M. Schwenk, O. Potz, S. Kramer, and T. O. Joos, Proteomics, 2003,3, 2155.

[2] M. Iqbal, M. A. Gleeson, B. Spaugh, F. Tybor, W. G. Gunn, M. Hochberg, T. Baehr-Jones, R. C. Bailey, and L. C. Gunn, IEEE J. Sel. Top. Quant. Electron. 2010, 16, 654.

[3] C. F. Carlborg, K. B. Gylfason, A. Kazmierczak, F. Dortu, M. J. Banuls Polo, A. MaquieiraCatala, G. M. Kresbach, H. Sohlstrom, T. Moh, L. Vivien, J. Popplewell, G. Ronan, C. A. Barrios, G. Stemme, and W. van der Winjgaart, Lab Chip 2010, 10, 281.

[4] A. Densmore, M. Vachon, D. X. Xu, S. Janz, R. Ma, Y. H. Li, G. Lopinski, A. Delage, J. Lapointe, C. C. Luebbert, Q. Y. Liu, P. Cheben, and J. H. Schmid, Opt. Lett. 2009, 34, 3598.

[5] H. Sipova, S. Zhang, A. M. Dudley, D. Galas, K. Wang, and J. Homola, Anal. Chem. 2010, 82, 10110.

[6] S. Chakravarty, J. Topoľančik, P. Bhattacharya, S. Chakrabarti, Y. Kang, and M. E. Meyerhoff, Opt. Lett. 2005, 30, 2578.

[7] W-C. Lai, S. Chakravarty, Y. Zou, C-Y. Lin, and R.T. Chen, Optics Lett. 2012, 37, 1208.

[8] S. Pal, E. Guillermain, R. Sriram, B. L. Miller, and P. M. Fauchet, Biosens. and Bioelectron. 2011, 26, 4024.

[9] A. Hosseini, D. N. Kwong, Y. Zhang; H. Subbaraman, X. Xu and R. T. Chen, IEEE J. Sel. Top. Quant. Electron. 2011, 17, 510.

[10] Y. Akahane, T. Asano, B-S. Song, and S. Noda, Nature 2003, 425, 944.

[11] A. Subramanian, S. J. Kennel, P. I. Oden, K. B. Jacobson, J. Woodward, and M. J. Doktycz, Enzyme and Microbial Tech.1999, 24, 26.

[12] C-Y. Lin, X. Wang, S. Chakravarty, B-S. Lee, W-C. Lai, and R. T. Chen, Appl. Phys. Lett. 2010, 97, 183302.

[13] S. Zlatanovic, L. W. Mirkarimi, M. M. Sigalas, M. A. Bynum, E. Chow, K. M. Robotti, G. W. Burr, S. Esener, and A. Grot, Sens. and Actuators. B 2009, 13, 141.

# Chapter 4: The role of group index engineering in series-connected photonic crystal microcavities for high density sensor microarrays[3]

## 4.1 INTRODUCTION

Integrated optical devices based on photonic crystals show a unique slow light phenomenon that significantly enhances light-matter interaction [1]. Several applications have been proposed and demonstrated, such as tunable delay lines [2, 3], ultracompact optical switches [4], and highly-efficient modulators [5-9]. In recent years, photonic crystal (PC) microcavities have attracted a lot of interests in biological and chemical sensing due to their compact sizes (of the order of a few square microns in surface area) and high sensitivity [10-15]. PC microcavities side coupled to a photonic crystal waveguide (PCW) take advantage of strong slow light effect, high quality factor resonances and a larger optical mode overlap with the analyte within a compact optical mode volume to provide superior performance compared to other chip based photonic technologies [15]. The miniaturized geometries enable multiple sensor microcavities on chip [16] to be integrated simultaneously, thus advancing the platform towards high density biosensing microarrays.

Dense integration of PC sensors on chip requires that PC microcavities be laid out in series and parallel in the optical circuit. In the past, we have demonstrated that multimode interference (MMI) power splitters can be employed to connect several PC

[3] Yi Zou, et. al., Applied Physics Letters, 104, 141103 (2014).

Y. Z. designed, fabricated the device, performed the experiments, analyzed the data, wrote the manuscript; S. C. designed the PC device, analyzed the data, and revised the manuscript; L. Zhu helped fabricate partial devices. R. T. C. oversaw all research phases and revised the manuscript. All authors discussed and commented on the manuscript.

microcavity sensors in parallel [16]. Multiplexing of two and five H1 (one missing or modified hole) PC microcavities in series were demonstrated previously in 2D [17] and 1D [18] PCs respectively. While the 1D PC couples to a strip waveguide at group index $n_g$~3.7, the 2D H1 PC microcavity couples to the 2D PCW at $n_g$~4.2. 2D PC microcavities of the L3, L13 or L55 types (where Ln denotes that the PC microcavity is formed by removing n holes along the Γ−K lattice direction in a hexagonal lattice), have demonstrated experimentally higher sensitivities [15] than devices in ref. [17, 18]. In Ln type PC microcavities, the resonances couple to the PCWs at $n_g$>12 [19]; hence group index engineering is necessary from coupling strip waveguides to the input and output of the PCWs to overcome Fresnel reflection losses at the resonance frequency of the PC microcavity. In this chapter, we experimentally demonstrate that group index taper engineering [20, 21] is necessary to efficiently multiplex L3-type PC microcavities in series. We demonstrate five L3 PC microcavities in series. We also demonstrate a dense microarray of 64 microcavity-based sensor nodes with series and parallel connected PC microcavity sensors, all sensors being simultaneously interrogated at the same instant of time, from a single optical source.

## 4.2 Device Design

The engineered PC structure, as shown in Fig. 3.1(a), has a L3 PC microcavity side coupled to a W1 line defect PCW, where L3 denotes 3 missing air holes and W1 denotes that the width of the PCW is $\sqrt{3}a$ where a is the lattice constant. Silicon slab thickness and air hole diameter are h=250 nm and d=0.55a respectively. For transverse electric (TE) polarization, the PCW only supports a single propagation mode inside the band gap as shown in the dispersion diagram in Fig. 3.1(b). The band diagram of the W1

PCW is obtained by three-dimensional plane wave expansion (PWE) simulations, considering water (refractive index n= 1.33) as the ambient.

Four such structures of Fig. 3.1(a) are connected in series to result in 4 PC microcavities in series. In contrast to previous designs, where the two PC microcavities are coupled to the same PCW, the isolated PC microcavity design ensures negligible cross-talk between individual sensors. Each PC structure in series is designed with a different lattice constant a of 392.5, 393.5, 394, and 396 nm respectively to stagger the transmission bandedge in each PC section. Since the L3 PC microcavity resonance is offset by a fixed wavelength (~20 nm) from the transmission bandedge of the corresponding PCW, the staggering of lattice constants thus ensures that the individual PC microcavity resonances do not overlap in the final output transmission spectrum. In each PC pattern, the group index taper is engineered by gradual widening of the PCW from W1 to W1.08 near the coupling strip waveguide as depicted in Fig. 3.1(a). W1.08 indicates that the width of the PCW in that section is $1.08 \times \sqrt{3}a$. Fig. 3.1(b) is the dispersion diagram of the W1 PCW with the smallest lattice constant a= 392.5 nm. The dispersion profile for the W1.08 PCW, also at a= 392.5 nm, is shown by the dashed black line. The corresponding group indices are also indicated in the figure.

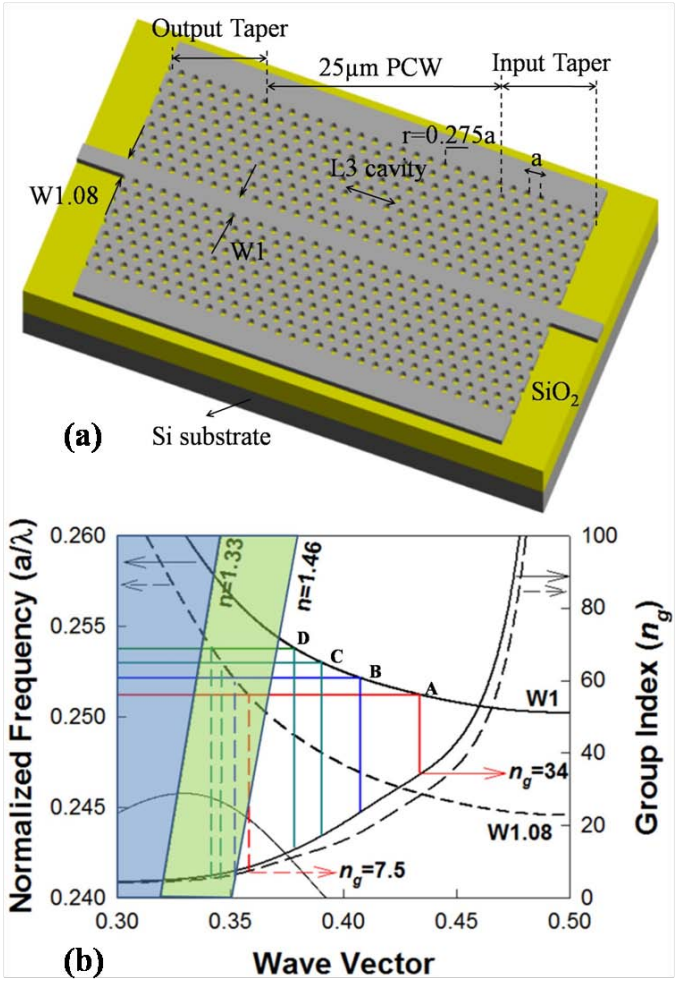


Figure 4.1 (a) Schematic of the PC sensor device with input and output strip waveguide, PC group index tapers, PC guiding region and L3 PC microcavity. (b) Dispersion diagrams of W1 (solid), and W1.08 (dash) PCWs in water (n=1.33) for PC with a=392.5 nm. The normalized resonance frequency of the coupled PC microcavity at a=392.5 nm is denoted by D. C, B, and A denote the normalized resonance frequencies of L3 PC microcavities in PC regions with a= 393.5 nm, 394 nm and 396 nm respectively cascaded in series with D (a=392.5 nm). Group index is plotted and its magnitude at the coupling frequency indicated in respective colors.

## 4.3 Device Characterization and discussion

The devices were fabricated on a silicon on insulator (SOI) wafer with 250 nm silicon layer and 3 μm buried oxide (BOX) layer. Fabrication details can be found in ref. [15]. All components including PCWs, PC microcavities, group index tapers and strip waveguides are patterned on SOI chip simultaneously. PCW devices with and without PC tapers were fabricated on the same chip. Scanning electron microscope (SEM) images of the fabricated structure and individual sections are shown in Fig. 4.2.

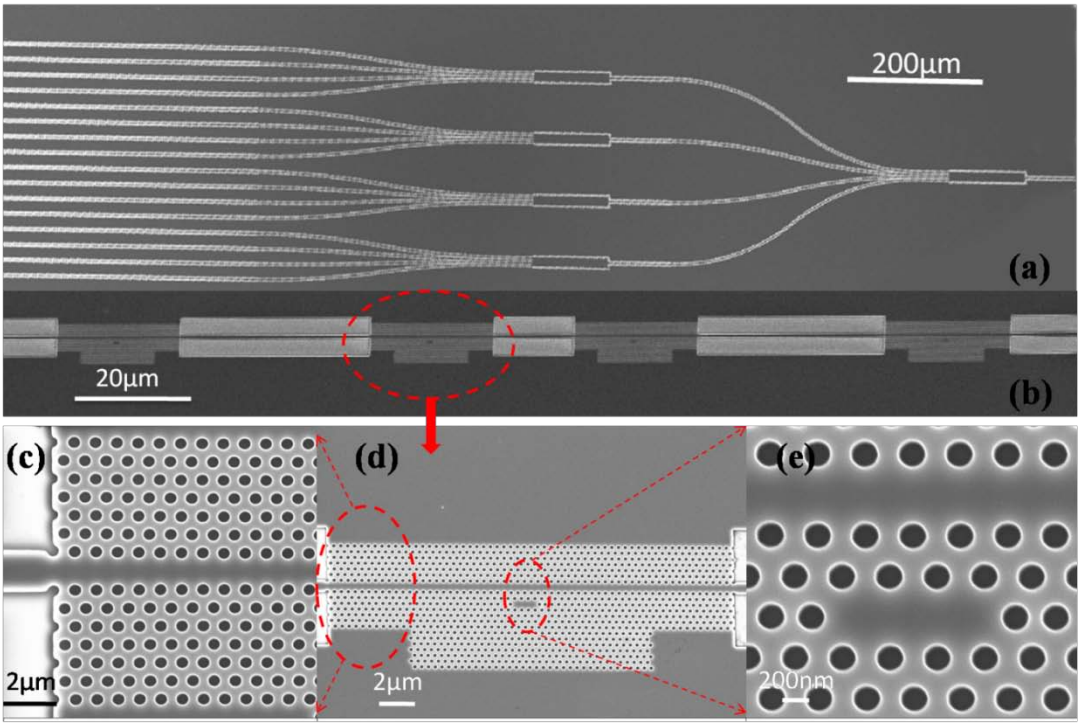


Figure 4.2 Scanning electron micrograph of the fabricated device, a) full device with 16 arms, b) each of the 16 arms with 4 cascaded microcavities, c) PCW adiabatic group index taper achieved by adiabatic width taper of PCW and high group index region, d) one of the 4 cascaded microcavities shown in (b), e) close up of the L3 PC microcavity located 2 rows away from a W1 PCW.

Light is coupled into and out of the devices using subwavelength grating couplers [15, 22] via polarization maintaining single mode fiber on the input side and standard single mode fiber on the output side respectively. Optical spectrum analyzer (OSA) is used to analyze the transmitted light. All the transmission spectra of PC devices with and without PC tapers were normalized to the spectrum from a reference waveguide comprising two grating couplers and one single strip waveguide. In the L3 PC microcavity coupled to W1 PCW in water, a single resonance is dropped in the output transmission spectrum of the PCW [10]. Fig. 4.3 plots the output transmission spectra from 2, 3 and 4 cascaded L3 PC microcavities in series, with and without index taper. All spectra are measured in water with the objective to implement biosensing.

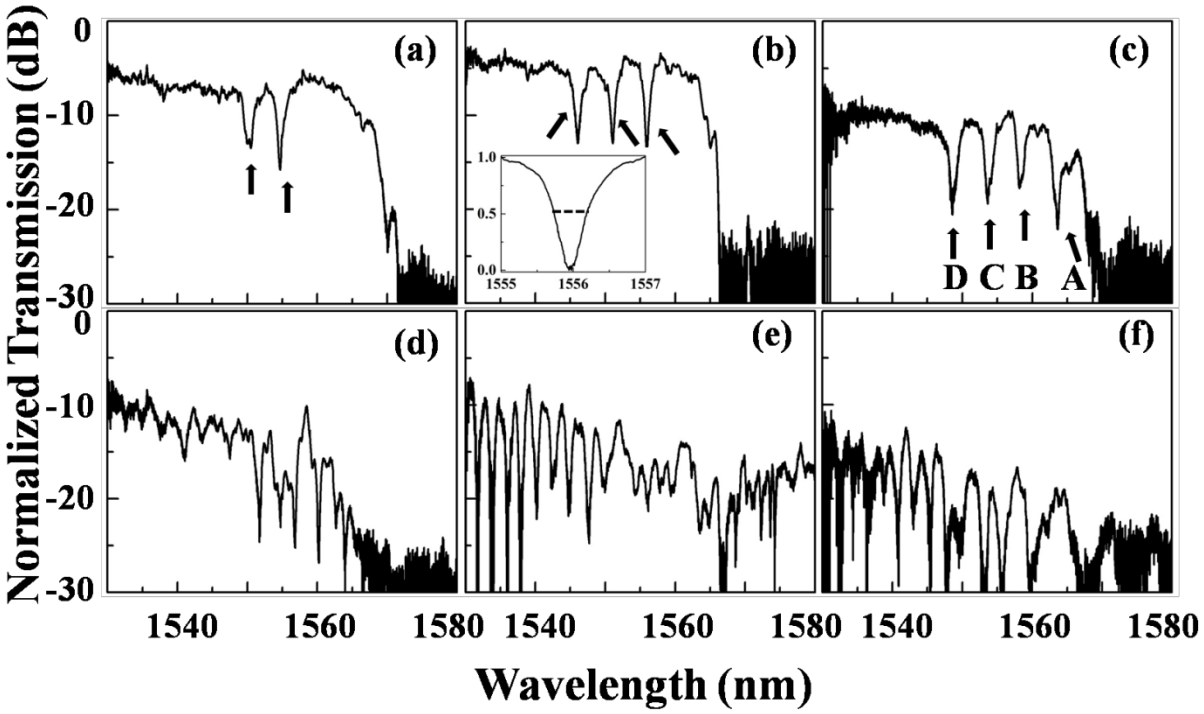


Figure 4.3 Normalized transmission spectral of W1 PCW with coupled series-connected L3 PC microcavities, a) 2 cavities, b) 3 cavities, c) 4 cavities with index taper; d) 2 cavities, e) 3 cavities, f) 4 cavities without index taper. All spectra are measured in water ambient. Resonant peaks are shown by arrows in (a), (b) and (c). In (c), resonant peaks are also labeled as A, B, C and D corresponding to Fig. 4.1(b). Inset (b) shows magnified linear scale spectrum of resonance peak closest to the bandedge. The dash line shows the full width at half maximum (FWHM).

With group index tapers, as shown in Fig. 4.3(a), (b), and (c), 2, 3, and 4 resonant peaks respectively are clearly seen. In Fig. 4.3(c), when four PC microcavities are connected in series as shown in fig. 4.2 (b), the resonances of the L3 PC microcavities in the respective sections are dropped from the transmission spectrum of the series

connected W1 PCWs. The four resonances are indicated as A, B, C, and D respectively arising from resonances in largest to smallest lattice constant PC sections. The resonances are easily distinguished, and the bandedges are also sharp with 20dB extinction ratio between the transmission band and the band gap. In contrast, in Fig. 4.3(d), (e), and (f), without PC group index tapers, the resonant peaks are probably buried in noise fringes resulting from group index mismatch between the strip waveguide and PCW.

The normalized resonance frequencies of 4 cascaded L3 PC microcavities are calculated from the experimental transmission spectrum as indicated by lines with different colors A, B, C and D in Fig. 4.1(b). In demarcating the position of the resonance wavelength in the dispersion diagram, based on previous results [19, 21], we estimate that the group index at the experimentally observed transmission bandedge is $n_g$ ~35. Mode D represents the microcavity resonance for the L3 PC microcavity in the PC pattern with smallest lattice constant a=392.5 nm. The resonance wavelength that is dropped by this PC microcavity is coupled to the PCW at the strip waveguide-PCW interface at $n_g$~ 6 instead of $n_g$~13 which is in the absence of a group index taper.

Since the wavelengths C, B and A that are dropped in succeeding PC stages must first propagate through the PC stage with a= 392.5 nm, Fig. 4.1(b) shows that in the absence of a group index taper, these wavelengths would be coupled into the first PC stage at increasing group indices, reaching $n_g$ =34 at the resonance wavelength A. Such a large group index mismatch with the single mode strip waveguide makes the coupling efficiency very low. It also results in huge Fresnel reflections and Fabry-Perot resonance fringes in the output transmission spectra as observed in Figs. 3(d), (e) and (f). We also note the higher propagation loss with increasing series cascading of PC sections. The higher loss and decrease in extinction ratio is also evidenced by Fig. 4.3, where a

bandedge is vaguely discernible in Fig. 4.3(d), by comparing with Fig. 4.3(a); however, no sharp bandedges can be seen in Figs. 4.3(e) and 4.3(f). When a group index taper is employed, resonance wavelength A instead couples to the first PC pattern and succeeding PC patterns at a low group index $n_g$=7.5 which significantly lowers the reflection losses and Fabry-Perot fringes. Noise ripples arising from such reflection is thus suppressed below 2dB. The transmission bandedge is clearly observable in each case. The dispersion engineering is done in each stage, so that the resonance wavelength A dropped in the PC microcavity in the last (fourth) stage with a=396 nm has significantly reduced reflection losses in preceding stages. The same argument holds for resonances C and B dropped by the L3 microcavities in the second and third PC stages in series.

In Fig. 4.4, we show the output transmission spectrum from 5 series-connected L3 PC microcavities, with group index engineering in each stage. 5 distinct resonant peaks are observed. In biosensing, resonance wavelength shifts in the range 1-2 nm have been observed at the highest detected concentration of 1μM. Hence, we strive to maintain 2nm spacing between individual resonances, so that resonances from individual PC microcavities do not overlap with others in the microarray when a shift in the corresponding PC microcavity is caused by probe-target biomolecule conjugation induced refractive index changes. From Fig. 4.4, the five resonance peaks are separated by roughly 2 nm from each other. We note that the extinction ratios of peaks marked by solid arrows are around 12 dB. A Lorentz curve fitting of the two resonance peaks indicated by dashed arrows indicates that the extinction ratios are roughly 8 dB and 15 dB respectively for the peaks at 1554 nm and 1556 nm. The variation of extinction ratio is within the range typically observed due to fabrication differences. Fabrication differences from designed etched hole diameters within the same chip results in the two

resonances shown by dashed arrows being closer to each other than designed. Since the L3 PC microcavity resonance is offset approximately 20 nm from the W1 PCW transmission bandedge, by appropriate choice of lattice constants, and better control of fabrication, we estimate that up to 8 PC microcavities can be easily connected in series using the method demonstrated here.

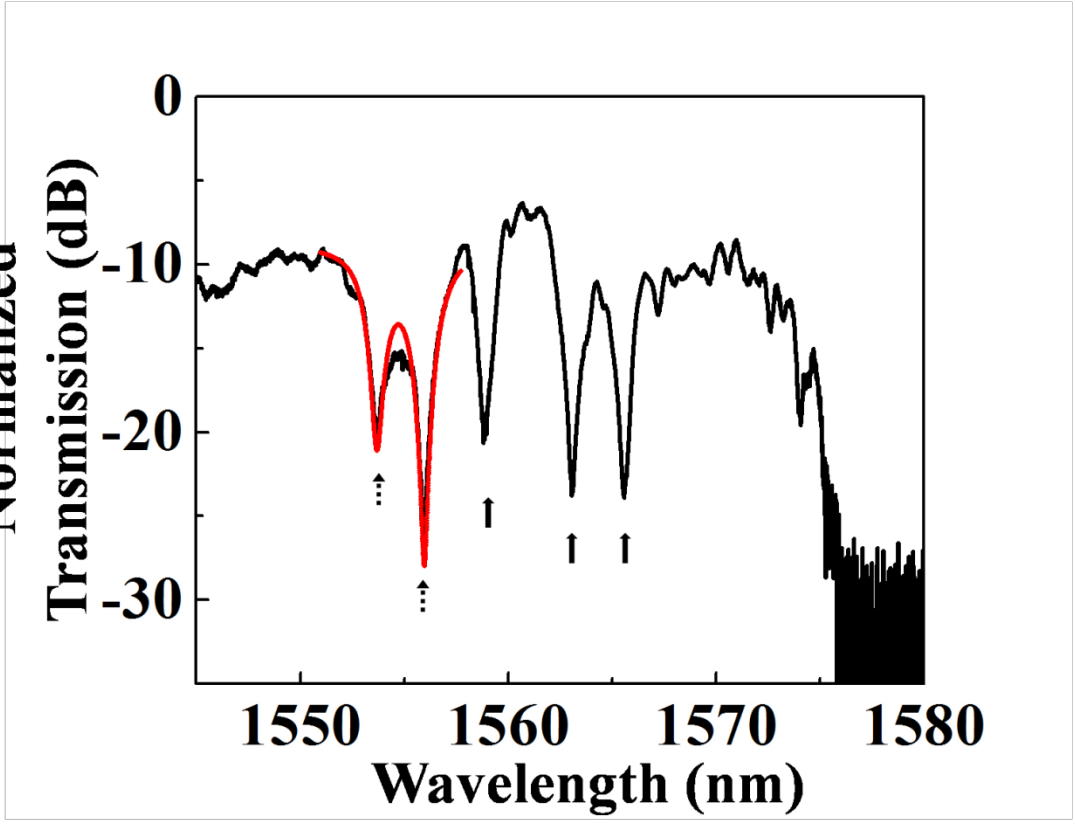


Figure 4.4 Normalized transmission spectrum of five series-connected L3 microcavity with index taper, in water. Spectrum is normalized to reference strip waveguide, and resonant peaks are shown by arrows. Red curve is obtained by a Lorentz fit of the two individual resonances shown by dashed arrows.

The series cascaded PC microcavities are next combined with two-stage cascaded 1 × 4 MMIs to build a high density microarray with 1 input arm and 16 output arms. 4 PC microcavities are connected in series on each arm. Thus, in total, 64 (4x4x4) PC microcavities are integrated in one device. The output transmission spectrum in all 16 arms (4x4) is shown in Fig.4.5. All 16 arms have similar spectra; 4 distinct resonant peaks and sharp bandedges can be seen from each spectrum. The Q-factor in all microcavities in water varies between 2000-4000, which is a typical range of Q's that have been observed in our oxide clad single L3 PC microcavities in silicon. The location of the resonant peaks and bandedges are very similar. Small differences in absolute wavelength are observed due to fabrication imperfections. In biosensing, or chemical sensing, such small differences in the absolute wavelength do not matter since the relative resonance wavelength shift is the parameter of interest.

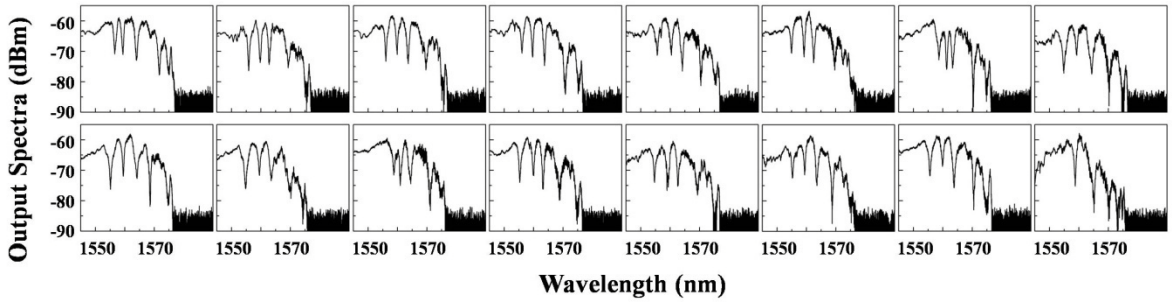


Figure 4.5 Output spectra of high density microarray with a total of 64 sensors integrated into 16 arms inside one device. 4 series-connected L3 microcavity are side coupled to PCW on each arm. All spectra are measured in water. 16 arms are made from a two stage cascaded 1×4 MMI in Fig. 4.2(a).

The multiplexed design presented here is similar to multi-channel drop filters in air ambient demonstrated previously [23, 24] with 4 L3 PC microcavities coupled to the same PCW in free-standing silicon membranes. The transmission spectrum of the PCW after the resonance drops was extremely noisy [25]. From the measurement system perspective, individually monitoring the dropped resonances out-of-plane from the individual PC microcavities is significantly more complicated than measuring all the dropped resonance wavelength shifts simultaneously in the in-plane output transmission spectrum of the coupled PCW.

Efforts to access the dropped resonances in-plane in ref. [23] resulted in low quality factor (Q) ~1000 in air at the output of the coupled PCW compared to Q ~35,000 observed by the authors out-of-plane in ref. [24]. Our sensing experiments in water ambient also indicate that series multiplexing beyond two PC microcavities coupled to a single PCW is difficult due to poor spectral quality in the in-plane output transmission spectrum from the PCW. Group index engineered PC designs help to overcome the limitation and allow several PC microcavities to be multiplexed in series, as demonstrated here.

## 4.4 SUMMARY

In summary, we demonstrated that group index taper engineering in PCW architectures is critical to enable series connection of PC sensors. We demonstrated a method for simultaneous interrogation of 64 PC microcavity sensors from a single optical source. While important in dense integration of sensors in biosensing microarrays, similar designs may also be incorporated in the future into compact add-drop filter designs for optical communications on-chip.

## 4.5 References


[1] T. Baba, Nature Photonics 2, 465 (2008).

[2] M. Povinelli, S. Johnson, and J. Joannopoulos, Opt. Express 13, 7145 (2005).

[3] C. Y. Lin, H. Subbaraman, A. Hosseini, X. Wang, L. Zhu, and R. T. Chen, Appl. Phys. Lett. 101, 051101 (2012).

[4] D. M. Beggs, T. P. White, L. O'Faolain, and T. F. Krauss, Opt. Lett. 33, 147 (2008).

[5] Y. Jiang, W. Jiang, L. Gu, X. Chen, and R. T. Chen, Appl. Phys. Lett. 87, 221105 (2005).

[6] L. Gu, W. Jiang, X. Chen, L. Wang, and R. T. Chen, Appl. Phys. Lett. 90, 071105 (2007).

[7] X. Wang, S. Chakravarty, B. S. Lee, C. -Y. Lin, and R. T. Chen, Opt. Lett. 34, 3202 (2009).

[8] C. -Y. Lin, X. Wang, S. Chakravarty, B. S. Lee, W. Lai, J. Luo, A. K. -Y. Jen, and R. T. Chen, Appl. Phys. Lett. 97, 093304 (2010).

[9] A. Hosseini, X. Xu, H. Subbaraman, C. Lin, S. Rahimi, and R. T. Chen, Opt. Express 20, 12318-12325 (2012).

[10] W. -C. Lai, S. Chakravarty, Y. Zou, and R. Chen, Opt. Lett. 37, 1208 (2012).

[11] S. Chakravarty, Y. Zou, W. Lai, and R. T. Chen, Biosens. Bioelectron. 38, 170 (2012).

[12] D. Dorfner, T. Zabel, T. Hürlimann, N. Hauke, L. Frandsen, U. Rant, G. Abstreiter, and J. Finley, Biosens. Bioelectron. 24, 3688 (2009).

[13] M. Lee, and P. M. Fauchet, Opt. Express 15, 4530 (2007).

[14] S. Zlatanovic, L. W. Mirkarimi, M. M. Sigalas, M. A. Bynum, E. Chow, K. M. Robotti, G. W. Burr, S. Esener, and A. Grot, Sensors and Actuators B, 141, 13 (2009).

[15]Y. Zou, S. Chakravarty, D. Kwong, W. Lai, X. Xu, X. Lin, A. Hosseini, and R. T. Chen, IEEE J. Sel. Top. Quantum Electron. 20(4), 6900710 (2014).

[16] Y. Zou, S. Chakravarty, W. Lai, C. Lin and R. T. Chen, Lab Chip 12, 2309 (2012).

[17] E. Guillermain, and P. M. Fauchet, Mater. Res. Soc. Symp. Proc. 1191, 1191-OO11-06 (2009)

[18] S. Mandal, and D. Erickson, Opt. Exp. 16(3), 1623 (2008).

[19] W. -C. Lai, S. Chakravarty, Y. Zou, Y. Guo, and R.T. Chen, Appl. Phys. Lett. 102, 041111 (2013).

[20] P. Pottier, M. Gnan, and R. M. De La Rue, Opt. Express 15, 6569 (2007).

[21] C. Y. Lin, X. Wang, S. Chakravarty, B. S. Lee, W. Lai, and R. T. Chen, Appl. Phys. Lett. 97, 183302 (2010).

[22] X. Xu, H. Subbaraman, J. Covey, D. Kwong, A. Hosseini, and R. T. Chen, Appl. Phys. Lett. 101, 031109 (2012).

[23] H. Takano, B-S. Song, T. Asano, and S. Noda, Opt. Exp. 14 (8), 3491 (2006).

[24] Y. Akahane, T. Asano, B-S. Song, and S. Noda, Nature 425, 944 (2003).

[25] B. -S. Song, T. Asano, Y. Akahane, Y. Tanaka, and S. Noda, J. Lightwave Tech. 23(3), 1449-1455 (2005).

# Chapter 5: Integrated slot waveguides in silicon-on-sapphire for Mid Infrared[4]

## 5.1 INTRODUCTION

The mid-infrared (MIR) regime, which typically ranges from 2-20μm, has attracted a lot of interest due to its potential applicability in a wide variety of areas, such as trace-gas sensing, free-space communication, environmental monitoring and thermal imaging [1].

Most of the chemical bonds have much stronger absorption peaks in MIR than near-infrared (NIR), so by moving from NIR to MIR, the sensitivity of spectroscopy can be enhanced by several orders.

As proposed by Soref et. al in Ref. 1 and 2, silicon is an ideal platform for MIR applications up to 8μm benefiting from its low material losses, mature fabrication technologies, and high refractive index. Traditional silicon on insulator (SOI) wafer has been widely used in NIR, but it is limited by high absorption of silicon dioxide in the range between 2.6 to 2.9μm and above 3.5μm. Hence, silicon on sapphire (SOS) was proposed as an alternative platform which has a transparent window up to 5.5μm, and also provides a high refractive index contrast between the core and the cladding [1, 2]. So far, SOS based strip waveguides operating at 2.75μm [3], 4.5μm [4, 5], 5.18μm [6] and

---

[4] Yi Zou, et. al., Opt. Lett. 39, 3070-3073 (2014).

Y. Z. designed, fabricated the device, performed the experiments, analyzed the data, wrote the manuscript; H. S., and S. C. helped analyze the data, and revised the manuscript; X. X., W. L. and A. H. helped design partial devices. R. T. C. oversaw all research phases and revised the manuscript. All authors discussed and commented on the manuscript.

5.5μm [7] have been demonstrated. Besides, several optical components such as grating couplers operating at 2.75μm [3, 8] and 4.5μm [5], ring resonators operating at 2.75μm [8], 4.5μm [5] and 5.5μm [7] have been realized on SOS. The SOS platform is thus very attractive for integrated MIR photonics. So far, to the best of our knowledge, slot waveguides have not been demonstrated on SOS platform. Slot waveguides can provide enhanced light-matter interaction, and thus are very useful components for both optical sensing to achieve high sensitivity and on-chip interconnects for device miniaturization. The enhanced electric field in the narrow low-index slot in slot waveguides compared to conventional waveguides has already been demonstrated in the NIR [9, 10]. The high optical confinement, combined with the inherent larger absorption cross section of fundamental molecular vibration signatures of various organic and inorganic compounds in the MIR, can lead to an effectively more sensitive sensor device.

In this chapter, we demonstrate subwavelength grating (SWG) coupled slot waveguide for the first time in SOS for transverse-electric (TE) polarized wave operation at 3.4μm wavelength.

## 5.2 Device Design

The slot waveguides are designed using FIMMWAVE software from PhotonDesign. The rail width W and slot width S are optimized to achieve high confinement in the slot, as shown in Fig 5.1(a). High electric-field confinement (about 43%) is achieved in the slot for W=0.6μm and S=0.13μm. Fig. 5.1(b) shows the transverse-electric (TE) field profile in the slot waveguide corresponding to the above dimensions.

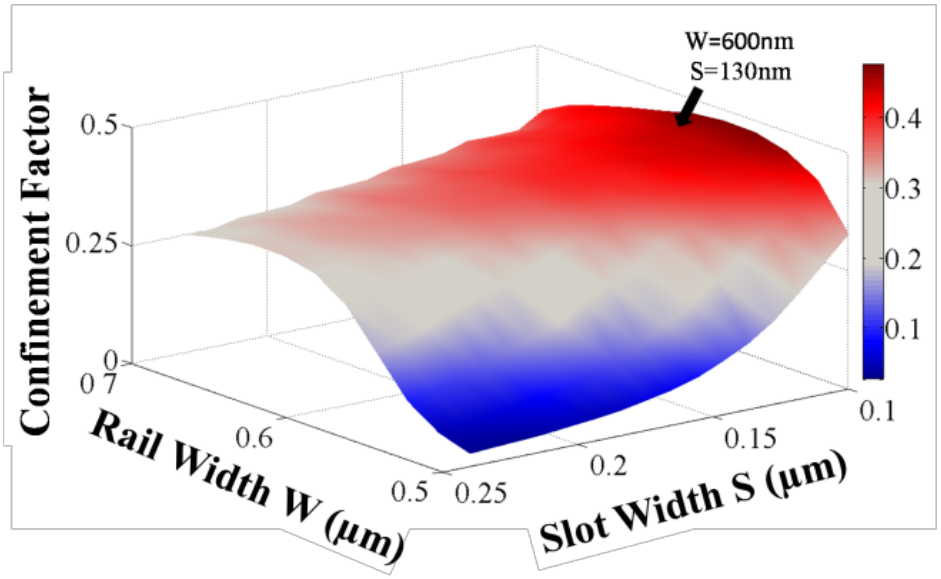


(a)

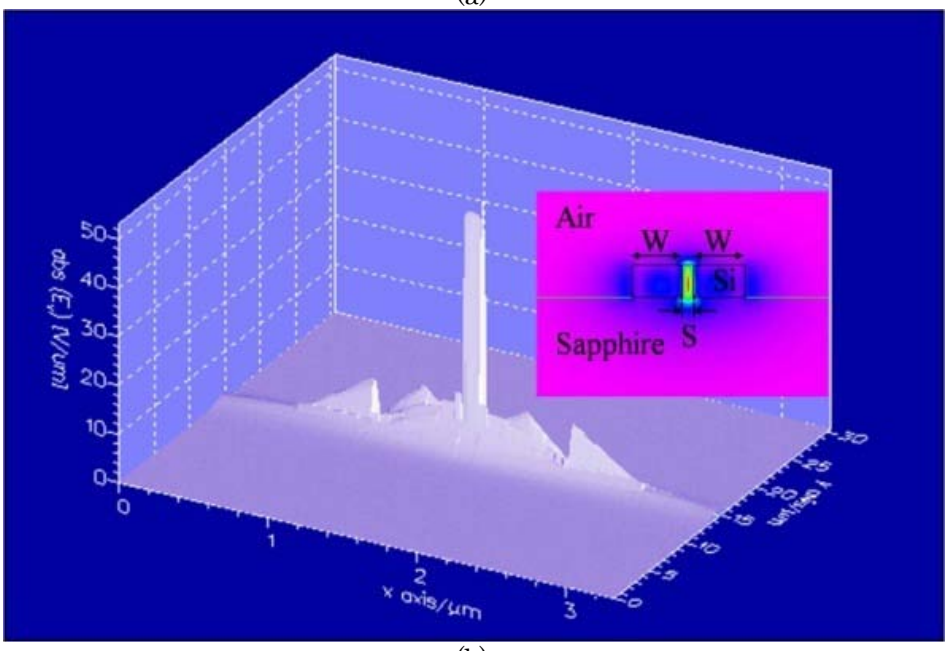


(b)

Figure 5.1 (a) Confinement factor as a function of slot width S and rail width W, (b) simulated electric field for a slot waveguide with W=0.6μm and S=0.13μm.A high confinement in the slot is obtained.

Next, we designed an efficient strip-to-slot waveguide mode converter. A mode converter is a very crucial component in slot waveguide devices. A poorly designed mode converter would lead to large insertion losses. In NIR, several mode converters have been proposed to achieve highly efficient conversion [11, 12.]. Two-step tapers have more efficient performance and are more robust in fabrication tolerance compared to other mode converters in the literature [11, 12, 13]. We therefore adopt a two-step taper structure in our design [13]. The structure is shown in Fig. 5.2(a). A strip waveguide with a width of 1μm is chosen to ensure single mode propagation of the fundamental TE polarized wave. The mode converter is composed of two sections: a Taper1 section with length $L_{taper1}$=4μm, where the slot width S is reduced from 600nm to 130nm, and a Taper2 section with length $L_{taper2}$=10μm, where the silicon rail width changes from 1μm to 600nm, as shown in Fig. 5.2(a). Taper 1 helps to keep the reflection losses low [13]. Taper 2 ensures that the electric field converts gradually from the strip waveguide into the air gap and finally forms the slot mode. The above parameters provided the best simulated conversion efficiency of 98% (-0.08dB) from a set of scans with varying $L_{taper1}$ and $L_{taper2}$ using FIMMWAVE as shown in Fig. 5.2(b). The electric field distribution for the optimized design is also plotted in Fig. 5.2(a).

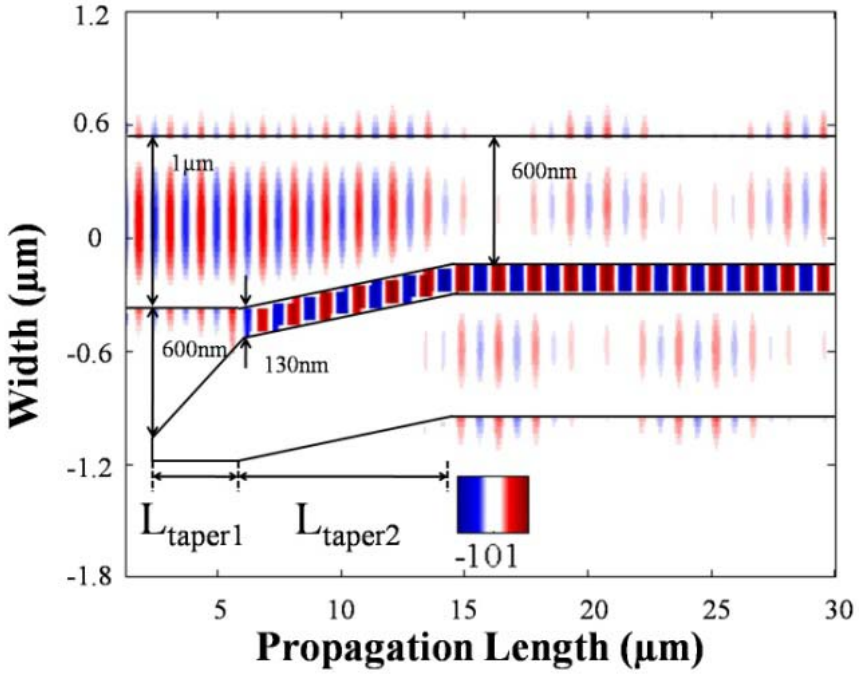


(a)

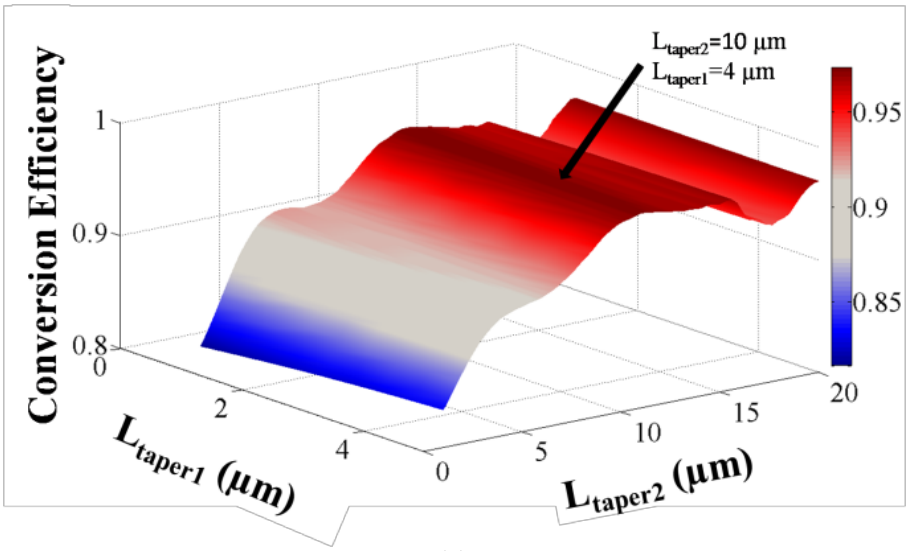


(b)

Figure 5.2 (a) Simulated electric field for the mode converter, the simulation data shows 98% of conversion efficiency from strip waveguide mode to the slot waveguide mode when $L_{taper1}$=4μm and $L_{taper2}$=10μm. (b) Conversion efficiency as a function of $L_{taper1}$ and $L_{taper2}$.

In order to couple light into and out of the waveguide components, SWG couplers are designed, with an operating wavelength at 3.4μm. The grating couplers are designed based on our previous design procedure [14, 15]. TE polarized wave is selected since our vertical slot waveguide only supports TE wave. A 2D simulation package from CAMFR is first utilized to get the optimized period and filling factor along waveguide propagation direction, as well as the effective subwavelength refractive index ($n_{sub}$). The simulated parameters are then verified using 2DFDTD. Next, the parameters of the subwavelength structure, such as air trench width, length, and period, are calculated by using effective index approximation[16]. For our structure operating at 3.4μm wavelength, the optimized SWG trench width, length and period are calculated as 152nm, 825nm, and 800nm, respectively. The grating period is set at 1500nm. The design results in an effective subwavelength refractive index ($n_{sub}$) of 2.45 in the propagation direction, and the peak emission angle is obtained as$11^{O}$ from normal incidence. The simulated transmission spectrum, indicated in red in Fig. 5.3(a) shows a maximum efficiency of about 36% from fiber to SWG coupler near 3.4μm. The simulated optical field distribution is shown in Fig. 5.3 (b). It can be seen that good coupling into a fiber positioned at $11^{O}$ is achieved.

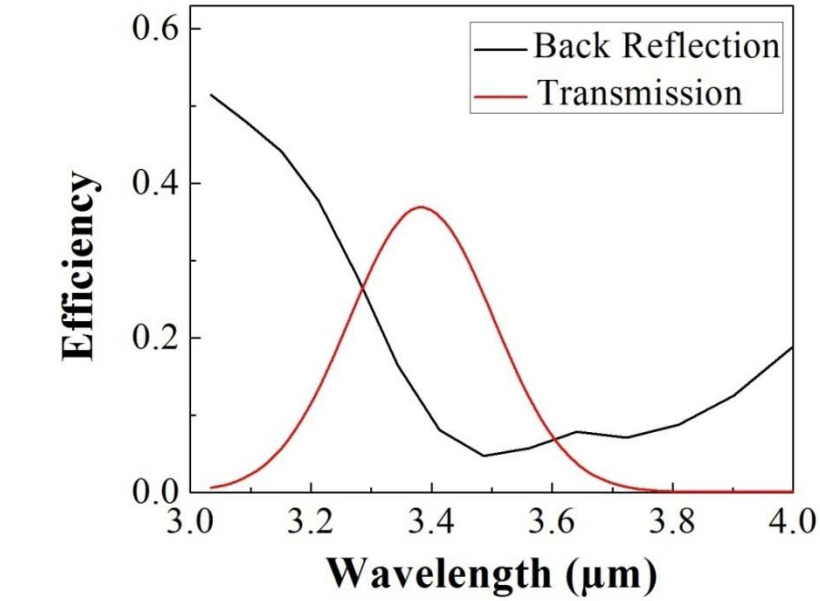


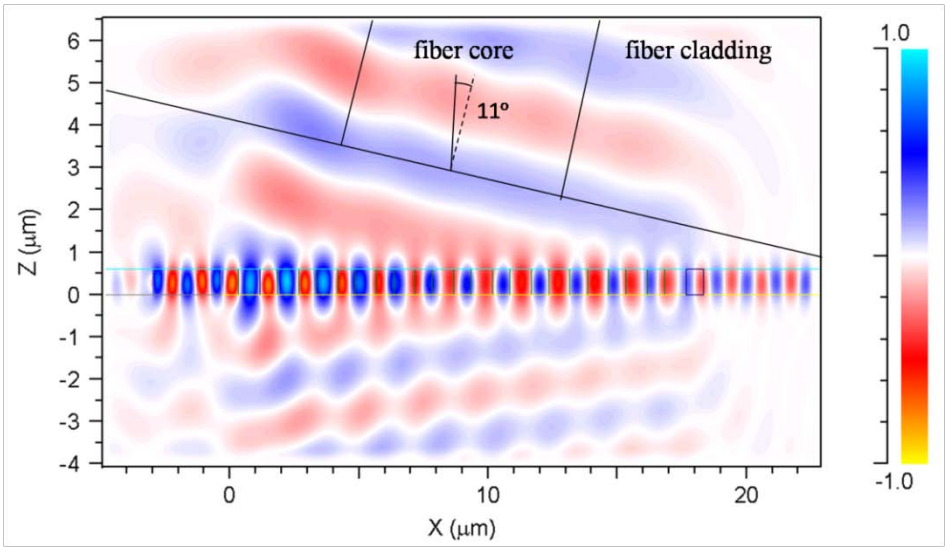


Figure 5.3 (a) Simulated coupling efficiency from fiber (red curve) show the peak is located around 3.4μm, and the reflection (black curve), and (b) simulated output optical field from grating coupler to fiber.

## 5.3 Device Fabrication

The devices are fabricated on a silicon-on-sapphire (SOS) platform with 600nm silicon layer on a 500μm thick sapphire substrate. A 140nm silicon dioxide layer is first deposited on top of silicon layer using plasma enhanced chemical vapor deposition (PECVD) to serve as a hard mask for pattern transfer. All the components including SWG couplers, strip waveguides, slot waveguides and strip-to-slot waveguide mode converters are patterned in one step using JEOL JBX-6000FS electron-beam lithography tool with ZEP-520A ebeam resist, followed by developing in n-Amyl acetate (ZEP-N50) for 2mins, and rinsing in isopropyl alcohol (IPA). The ebeam resist pattern is next transferred to silicon dioxide by reactive ion etching (RIE) using $CHF_3$ and $O_2$ at 400V DC biasand 40mTorr pressure for 8mins. Following this, the pattern in silicon dioxide is transferred to silicon by inductively coupled plasma (ICP) etch using HBr and $Cl_2$ at 400W ICP power, 200W RF power, 10mTorr pressure and 20Torr Helium flow for backside cooling for 6.5min. Finally, the chip is cleaned using Piranha for 15min and followed with three cycles of Piranha/HF post-process treatment as suggested from Ref. [5]. A schematic of the fabricated device is shown in Fig. 5.4 (a). SEM images of the fabricated components are shown in Figs. 5.4 (b)-(f).

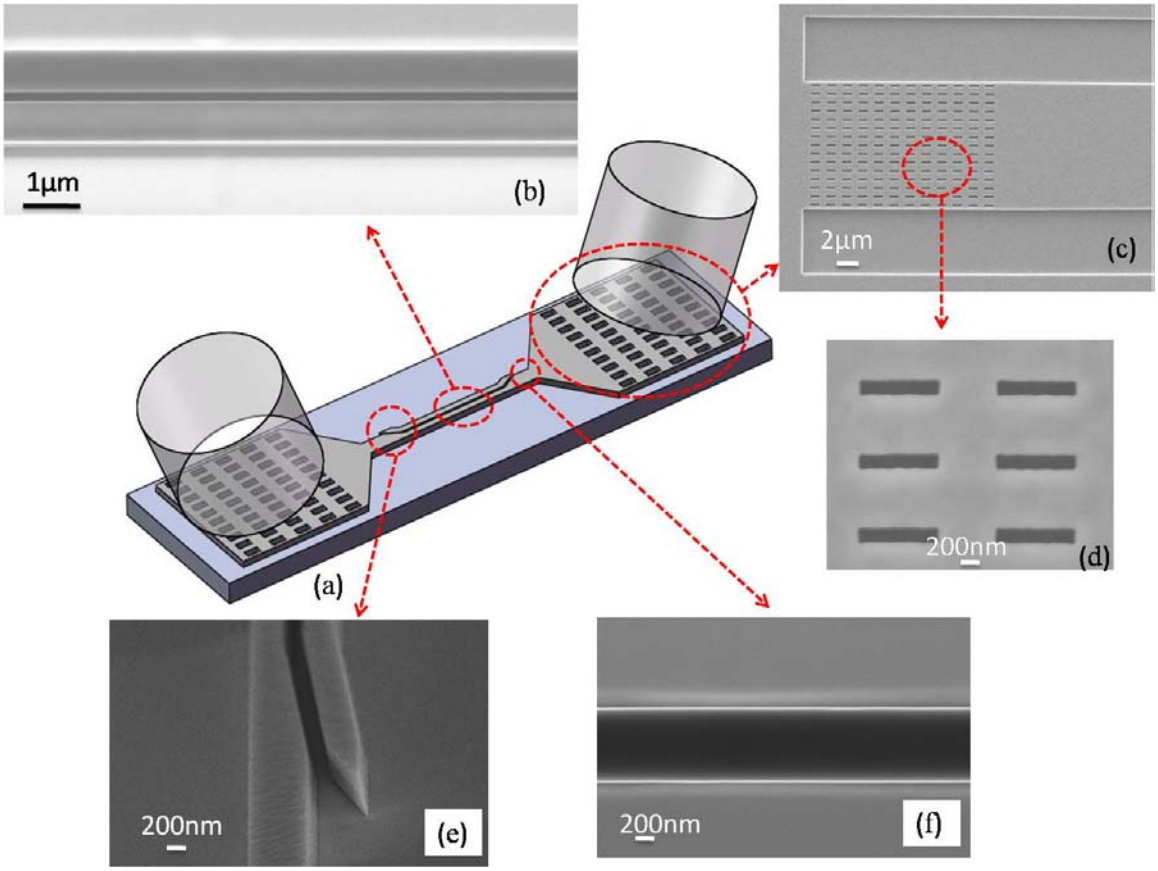


Figure 5.4 (a) Schematic of the fabricated device, (b) SEM image of fabricated slot waveguide, (c) SEM image of SWG coupler, (d) magnified view of air holes, (e) close up of strip waveguide to slot waveguide mode converter, and (f) SEM image of single mode strip waveguide with 1µm width.

## 5.4 Device Characterization

Devices are characterized using the setup schematically shown in Fig. 5.5. Light emitted from a continuous-wave interband cascade laser (ICL) from Thorlabs, with a fixed wavelength of 3.4µm, is passed through a pair of ZnSe lenses and coupled into a 9/125µm single mode $ZrF_4$ optical fiber from Thorlabs. Light from the optical fiber is then coupled into the fabricated chip via SWG couplers. At the output end, another SWG

coupler couples the light from chip to the output fiber. An InSb detector is used to measure the power from the output fiber. In order to improve the signal-to-noise ratio, a mechanical chopper is used with chopping frequency of 1KHz, and the detected signals from InSb are demodulated by a lock-in amplifier.

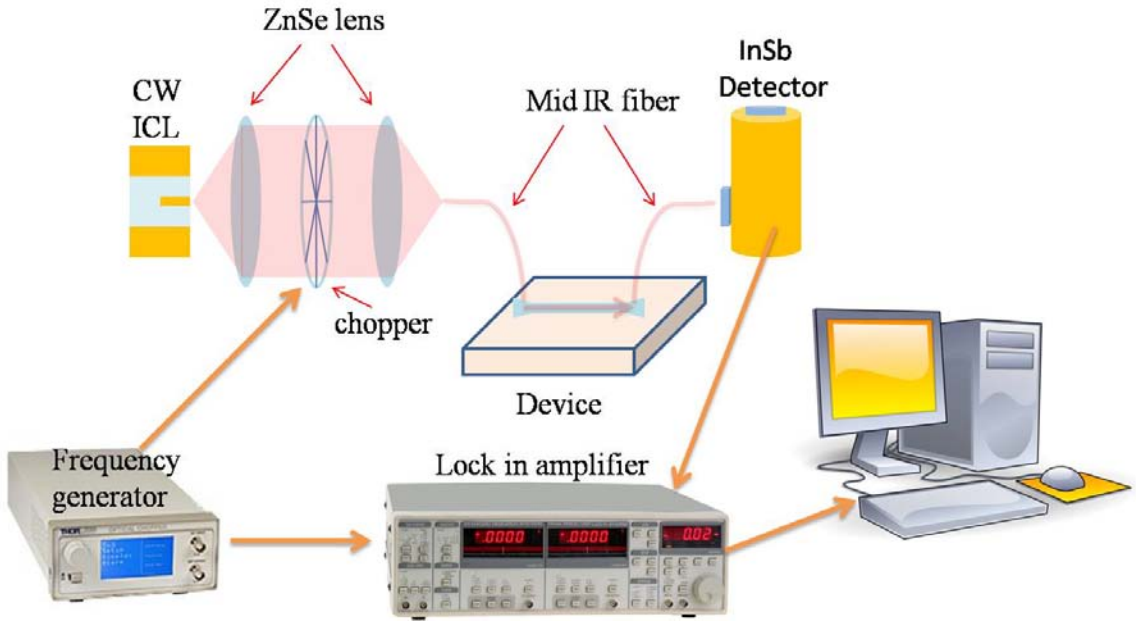


Figure 5.5 Schematic of the experimental setup used to characterize our devices.

In order to measure the coupling efficiency of the SWG couplers, light from the optical fiber positioned at $11^{o}$ was coupled into an SWG coupler pair, and the power from another tilted output fiber was measured. An insertion loss of 10.8dB was experimentally confirmed, which provides a coupling efficiency of 29% for each coupler, which gives a discrepancy of about 7% between the measured and the calculated values. This discrepancy could possibly be due to fabrication error, together with an underestimation

of measured coupling efficiency due to lack of knowledge of the exact polarization state, since no polarization maintaining fiber for MIR is currently available. Coupling efficiency for different incident angles are also measured and compared with simulation results. Reasonable agreement between simulated and measured values is observed in Fig. 5.6.

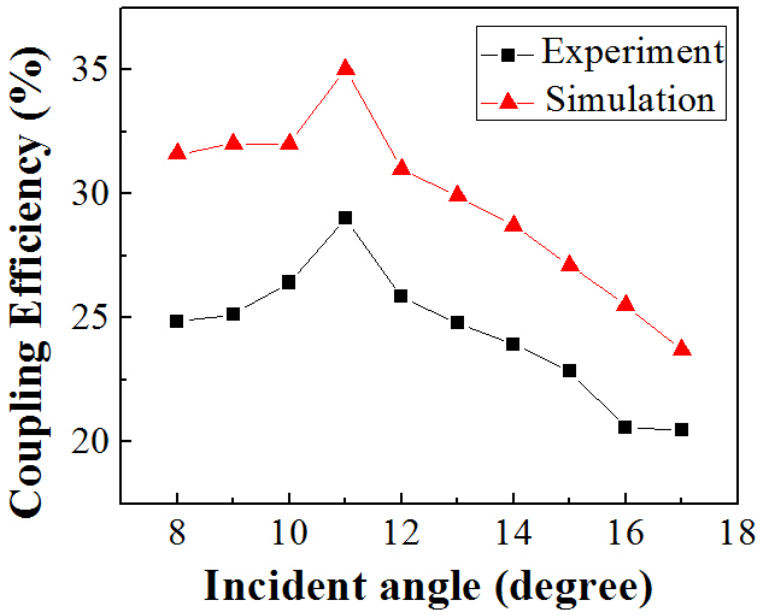


Figure 5.6 Experimental measured and simulated coupling efficiency with different incident angles.

The propagation loss of TE wave for the strip waveguides and the slot waveguides are measured using the cut-back method. Figs. 5.7(a) shows the measured loss from eight strip waveguides with lengths ranging from 1mm to 8mm, and Fig. 5.7(b) show four slot waveguides with length from 0.1mm to 0.3mm. By performing a linear fit to the data, we obtain propagation losses of 2.1dB/cm and 11dB/cm, for the strip and slot

waveguides, respectively. Since propagation loss of 0.74dB/cm was observed in SOS strip waveguide devices at 4.3-4.6μm [5], the larger value can be attributed to increased Rayleigh scattering loss at shorter wavelength. Better control of device fabrication will lead to lower loss in our slot waveguides.

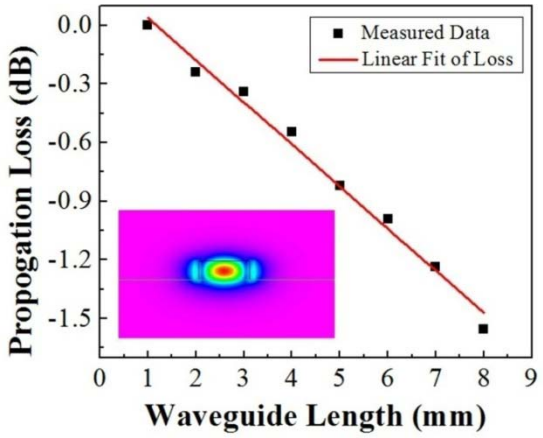


(a)

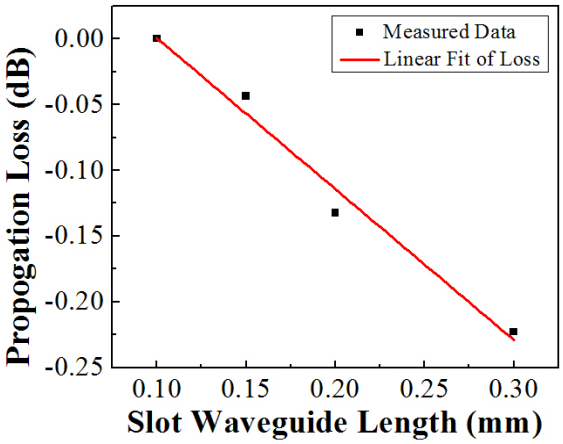


(b)

Figure 5.7 (a) Measured loss of eight single mode waveguides fabricated on SOS operating at 3.4 μm wavelength. The waveguides are 0.6μm in height and 1 μm in width. 2.1dB/cm propagation loss is achieved by linear fitting. (b) Measured loss of eight slot waveguides fabricated on SOS operating at 3.4 μm wavelength. A 11dB/cm propagation loss is achieved by linear fitting.

We also measured the conversion efficiency of our strip-to-slot waveguide mode converters by measuring the loss from several cascaded mode converters, as shown in Fig. 5.8. A linear fit to the data provides a loss of about -0.13dB per mode converter, corresponding to 97% conversion efficiency, which agrees well with the simulated result of 98% in Fig. 5.2(b).

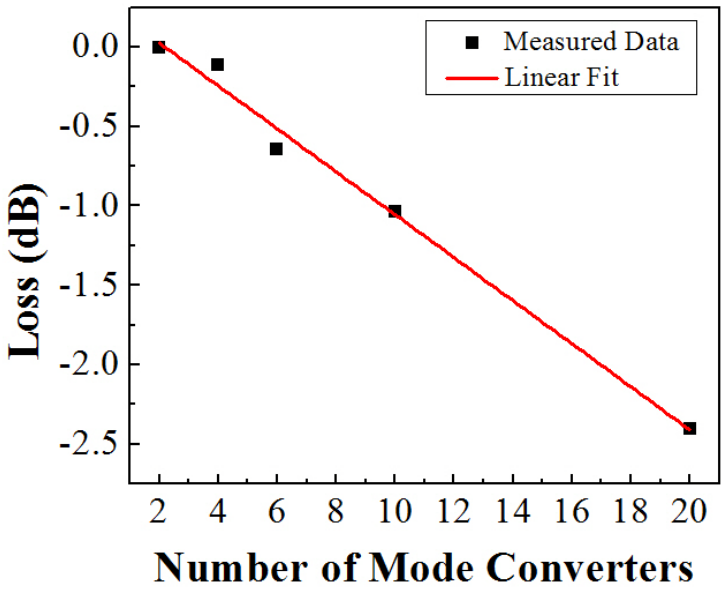


Figure 5.8 Measured loss versus number of strip-to-slot waveguide mode converters at an operating wavelength of 3.4μm. Approximately -0.13dB loss per mode converter is measured, corresponding to 97% conversion efficiency.

## 5.5 SUMMARY

In summary, we demonstrate to our knowledge the first slot waveguides in SOS for transverse-electric (TE) polarized wave guiding at 3.4 μm wavelength. Coupling efficiency of 29% for SWG coupler is experimentally demonstrated. Propagation loss of 11dB/cm was experimentally observed for slot waveguides. Two-stage taper strip-to-slot waveguide mode converters are utilized to gradually convert the strip waveguide mode into slot waveguide mode. The conversion efficiency for one mode converter is around -0.13 dB, corresponding to 97% conversion efficiency.

## 5.6 REFERENCES

[1] R. Soref, Nat. Photonics 4(8), 495 (2010).

[2] R. Soref, S. J. Emelett, and A. R. Buchwald, J. Opt. A 8(10), 840 (2006).

[3] X. Chen Z. Cheng, C. Y. Wong, K. Xu, C. Fung, Y. Chen, and H. K. Tsang, IEEE Photon. J. 4(1), 104 (2012).

[4] T. Baehr-Jones, A. Spott, R. Ilic, A. Spott, B. Penkov, W. Asher, and M. Hochberg, Opt. Express 18(12), 12127 (2010).

[5] R. Shankar, I. Bulu, and M. Loncar, Appl. Phys.Lett. 102(5), 051108 (2013).

[6] F. Li, S. D. Jackson, C. Grillet, E. Magi, D. Hudson, S. J. Madden, Y. Moghe, C. O'Brien, A. Read, S. G. Duvall, P. Atanackovic, B. J. Eggleton, and D. J. Moss, Opt. Express 19(16), 15212 (2011).

[7] A. Spott, Y. Liu, T. Baehr-Jones, R. Ilic, and M. Hochberg, Appl. Phys. Lett. 97(21), 213501 (2010).

[8] C. Y. Wong, Z. Cheng, X. Chen, K. Xu, C. K. Y. Fung, Y. M. Chen, and H. K. Tsang, IEEE Photon. J. 4(4), 1095 (2012).

[9] V. R. Almeida, Q. Xu, C. A. Barrios, and M. Lipson, Opt. Lett. 29(11), 1209 (2004).

[10] Q. Xu, V. R. Almeida, R. R. Panepucci, and M. Lipson, Opt. Lett. 29(14), 1626 (2004).

[11] Z. Wang, N. Zhu, Y. Tang, L. Wosinski, D. Dai, and S. He, Opt. Lett. 34(10) 1498 (2009).

[12] Y. Liu, T. Baehr-Jones, J. Li, A. Pomerene, and M. Hochberg, IEEE Photon. Technol. Lett. 23(20), 1496 (2011).

[13] R. Palmer, L. Alloatti, D. Korn, W. Heni, P. C. Schindler, J. Bolten, M. Karl, M. Waldow, T. Wahlbrink, W. Freude, C. Koos, and J. Leuthold, IEEE Photon. J. 5(1), 2200409 (2013).

[14] X. Xu, H. Subbaraman, J. Covey, D. Kwong, A. Hosseini, and R. T. Chen, Appl. Phys. Lett. 101, 031109 (2012).

[15] Y. Zou, S. Chakravarty, D. Kwong, W. Lai, X. Xu, X. Lin, A. Hosseini, and R. T. Chen, IEEE J. Sel. Top. Quantum Electron. 20(4), 6900710 (2014).

[16] S. M. Rytov, Sov. Phys. J. Exp. Theor. Phys. 2, 466 (1956).

# Chapter 6: Mid-Infrared Photonic Crystal Waveguides in Silicon-on-Sapphire

## 6.1 Introduction

Silicon has been the material of choice of the photonics industry over the last decade due to its easy integration with silicon electronics as well as its optical transparency in the near-infrared telecom wavelengths. In recent years, photonic devices on chips are increasingly being used for chemical and biological sensing. Ring resonators [1], photonic crystal waveguides (PCWs) [2], photonic crystal (PC) microcavities [3] operating at 1.55μm have been employed for biosensing. Optical biosensors can be theoretically designed for operation at any wavelength after taking into consideration the absorbance of water based biological media. In contrast, chemicals are best recognized by their unique wavelength specific optical absorption signatures. Slow light in PCWs [4] and PC slot waveguides [5, 6] has been used to reduce the optical absorption path length and achieve high detection sensitivity in on-chip optical absorption spectroscopy for the selective detection of volatile organic compounds [4, 5] and greenhouse gases [6] based on unique analyte absorption signatures in the near-infrared (near-IR). It is common knowledge that in contrast to the near-infrared, the mid-infrared (mid-IR) wavelengths offer at least two orders of magnitude larger absorption cross-sections than the near-IR. Silicon is optically transparent over the entire mid-IR till about 8μm [7]. Hence, PCWs and PC slot waveguides in silicon-on-insulator (SOI) (till 3.7μm), silicon-on-sapphire (SoS) (till 5.5μm) and free-standing silicon membranes (till 8μm) can serve as the ideal platform for highly sensitive optical absorption spectroscopy on chip. Strip [8-11] and slot waveguides [12] have been demonstrated by several groups in the mid-IR in silicon on both SOI and SoS. In spite of available material platforms and laser sources in the mid-IR, PC research in the mid-IR has been limited by the non-availability of appropriate

tunable laser sources that can characterize the entire PC transmission bandwidth [13, 14]. Optical parametric oscillators (OPOs) provide a relatively expensive and bulky option using free-space optics for optical coupling into mid-IR optical devices, and untenable for any realistic sensing system outside the lab [13]. Previously PC microcavities and PCWs have been demonstrated in free-standing silicon membranes in SOI in the mid-IR wavelengths [13, 14]. In this chapter, we present the first demonstration of photonic crystal waveguide (PCW) characteristics in SoS at the mid-IR wavelength 3.43μm of our fixed wavelength interband cascade laser (ICL). We demonstrate that by good control of device fabrication and device parameter engineering, PC waveguiding properties can be adequately determined in mid-IR PC devices to facilitate the accurate design of mid-IR PC sensors. The SoS platform provides a more rigid option for photonic sensing applications in the mid-IR compared to free-standing silicon membranes in SOI.

## 6.2 Device Design

The device comprises a conventional W1 PCW with a single missing row of holes along the Γ–K direction in a hexagonal lattice of air holes in silicon. Fig. 6.1(a) shows the simulated transmission spectrum of a W1 PCW with lattice constant a=845nm, radius of air holes r= 0.25a and height of silicon slab h=0.69a obtained by three-dimensional (3D) finite difference time domain (FDTD) simulation. Refractive indices of silicon and sapphire were considered as 3.429 and 1.7 respectively. A distinct transmission band edge is observed at λ=3.445μm. A conventional experimental demonstration of the transmission spectrum would simply comprise sweeping the wavelength range with a tunable spectrum and detector, or spectral identification via a spectral analyzer and a broadband source. However, it is also possible to characterize the PCW transmission characteristics by careful control of design and fabrication, and sweeping the lattice

constant a. Fig. 6.1(b) shows a set of FDTD simulations of a W1 PCW with different lattice constant a=830nm, 840nm, 845nm, 850nm, 860nm, 870nm and 890nm. The radius r was kept fixed at 0.25a. The height of the silicon device layer according to wafer specifications is 600+/- 60nm. In this work, the height of the silicon device layer was determined to be h=585nm from ellipsometry. h/a of the silicon slab was calculated accordingly for each lattice constant. The wavelength spectrum of our Fabry-Perot ICL is shown by the dashed black line.

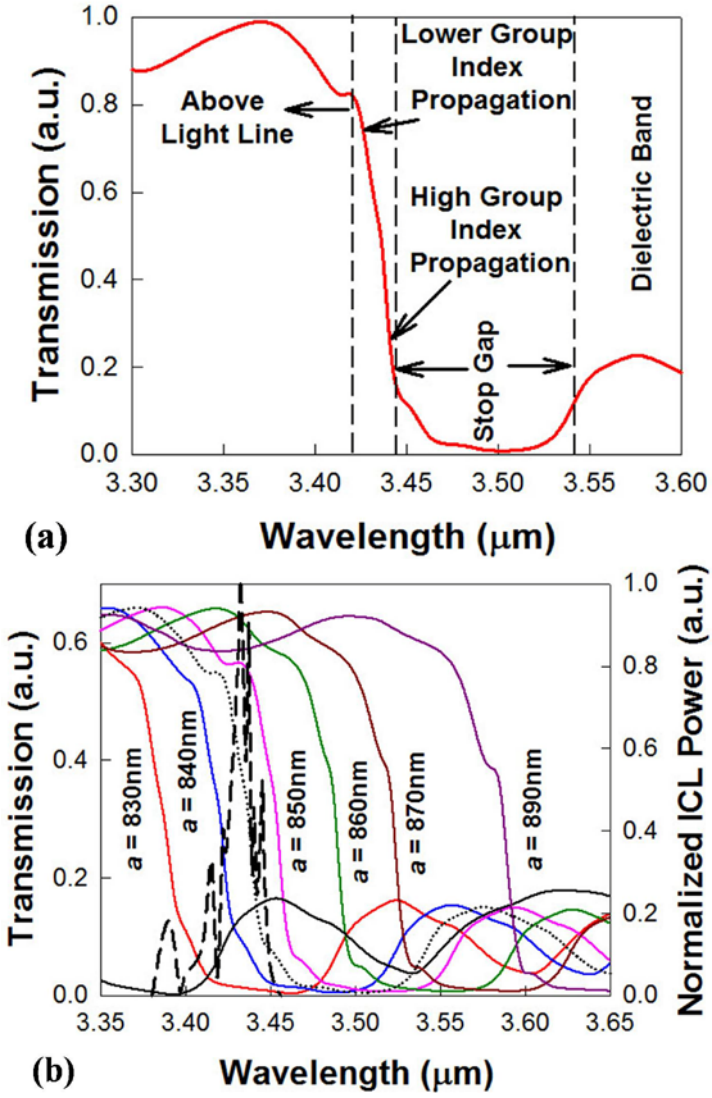


Figure 6.1 (a) 3D FDTD simulation of a short W1 PCW in silicon-on-sapphire for operation at 3.43μm with *a*=845nm. The different parts of the transmission spectrum are indicated. (b) Set of 3D FDTD simulations of short W1 PCWs with different lattice constants *a*. Simulation for *a*=845nm is indicated by the dotted black plot. The output spectrum of our source ICL is indicated by the dashed black plot (right axis).

## 6.3 Device Fabrication and characterization

Devices were fabricated using a combination of electron beam lithography and inductively coupled plasma etching. Light is guided in and out of the PCW by ridge waveguides with PC group index taper to enable high coupling efficiency into the slow light guided mode [15]. Fig. 6.2 shows the dispersion diagram of the W1 PCW obtained by 2D plane-wave expansion simulation using effective index n=2.91. Fig. 6.1(b) indicates that the ICL emission will propagate in the high group index regime in devices with a=845nm. Fig. 6.2 is thus calculated with a=845nm. The dispersion diagram shows the guided mode (in red) separated from the dielectric band by a stop gap. The light line for sapphire is superimposed. The PC group index taper is created by gradually tapering down the width of the PCW from the interface between the ridge waveguide and PCW over 8 lattice periods from W1.07 to W1. W1.07 indicates that the width of the PCW at the onset of the taper is $1.07\times \sqrt{3}a$. The red dashed plot in Fig. 6.2 shows the dispersion of the guided mode when the PCW is W1.07. Two dashed blue lines are drawn on the dispersion plots of the guided mode at the representative frequency $a/\lambda=0.246$. The slope of the lines $\delta k/\delta\omega$ gives the group indices (8 and 30 respectively) for W1.07 and W1 PCW, where $k$ is the wavevector and $\omega$ is the frequency. Hence instead of coupling light from the strip waveguide to the W1 PCW at a group index $n_g=30$ at $a/\lambda=0.246$ in Fig. 6.2, group index taper engineering results in light coupled from the strip waveguide into the PCW at $n_g=8$. It has been shown in the near-IR that such group index engineering reduces Fresnel reflection losses that would otherwise show significant fringe patterns in the PCW guided mode transmission spectrum [15].

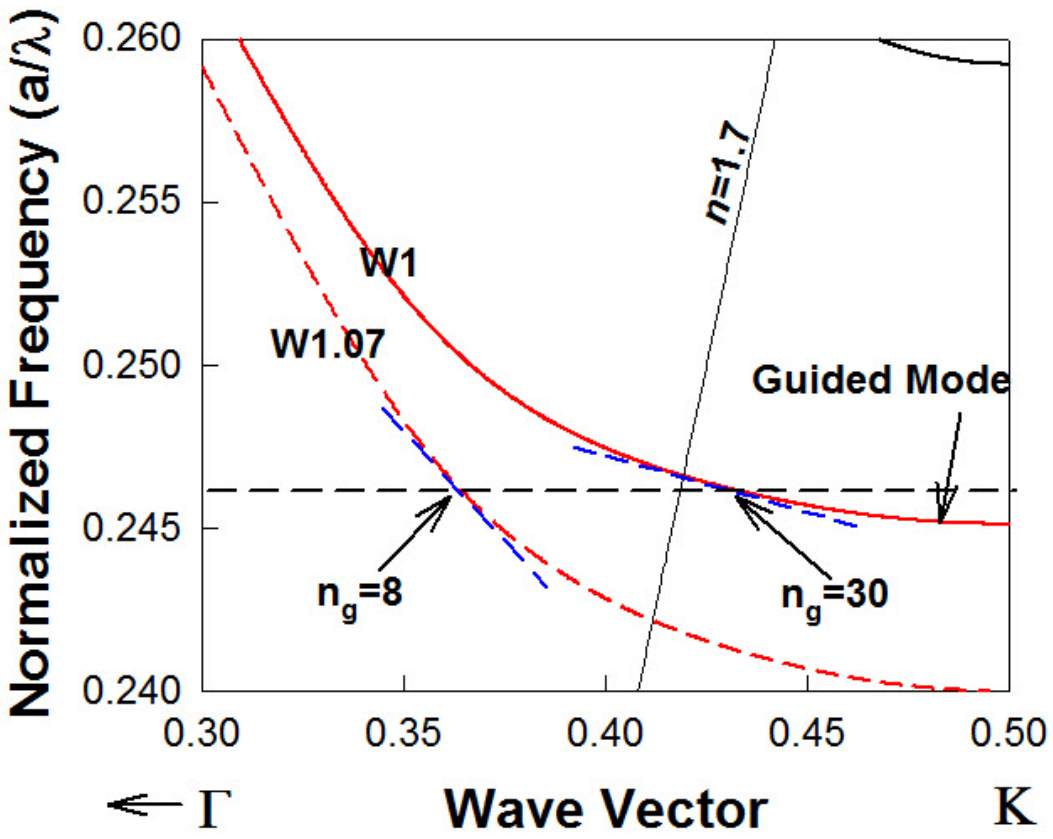


Figure 6.2 2D plane wave expansion simulation of the dispersion diagram of a sapphire clad silicon W1 PCW. The red dashed line indicates the PCW dispersion at the interface between silicon ridge waveguide and W1.07 PCW. The reduced group index at the interface is indicated by the lesser slope (dashed blue lines) at a representative frequency $a/\lambda$=0.246. Sapphire light line is superimposed.

Input and output ridge waveguides and sub-wavelength grating (SWG) couplers are fabricated in the same step as the PCW. The design, fabrication and experimental characterization of ridge waveguides and SWGs in SoS have been described in detail

elsewhere [12]. In order to ensure good control over the fabrication process, a thin conductive polymer (ESPACER) from ShowDenko chemicals was spin coated on the ebeam resist ZEP-520A, prior to ebeam lithography. The chip is cleaned using Piranha for 15 minutes and followed with three cycles of Piranha/HF post-process treatment [16]. Microscope and scanning electron micrograph images of the device are shown in Fig. 6.3.

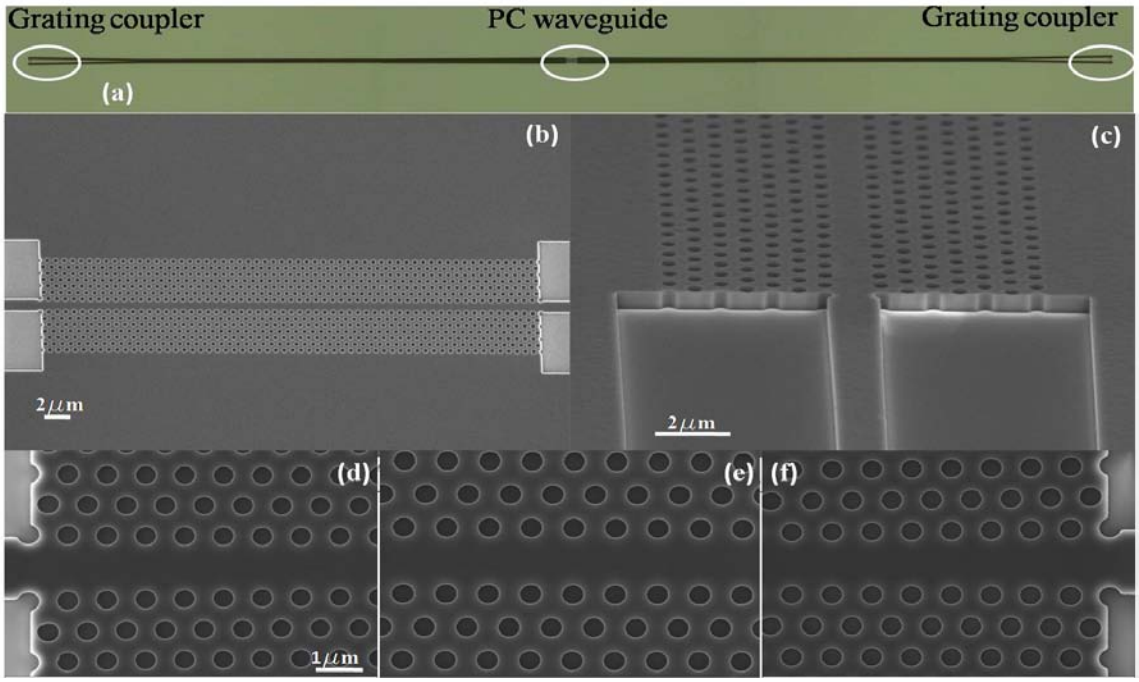


Figure 6.3 (a) Microscope image of the device showing input and output SWGs and PCW. (b) Top view SEM image of PCW and (c) side view SEM image of the PCW at the PCW-strip waveguide interface. Magnified top view SEM images of (d) input taper (e) PCW and (f) output taper.

The light from the output SWG for PCW devices with several lattice constants but the same *r/a* is plotted in Fig. 6.4(a). The length of the W1 PCW is 50μm. The plot is normalized with respect to the highest and lowest power observed versus lattice constant. It is observed that for a less than 845nm, the output power from the devices is practically zero. Fig. 6.4(a) also plots the output power from the devices when immersed in tetrachloroethylene ($C_2Cl_4$). $C_2Cl_4$ is practically non-absorbing at 3.43μm with a refractive index ~1.5 at room temperature. The absolute power measured by the photodetector is lower with $C_2Cl_4$ than with air cladding in Fig. 6.4(a) due to the lower modal confinement; however the normalized plot shows the transmission profile shifted to lower lattice constants. Fig. 6.4(b) plots the output power as a function of temperature for varying lattice constant. The temperature is varied from 25$^o$C to 60$^o$C. The normalized plot also shows a shift of the transmission profile to lower lattice constants, with increasing temperature.

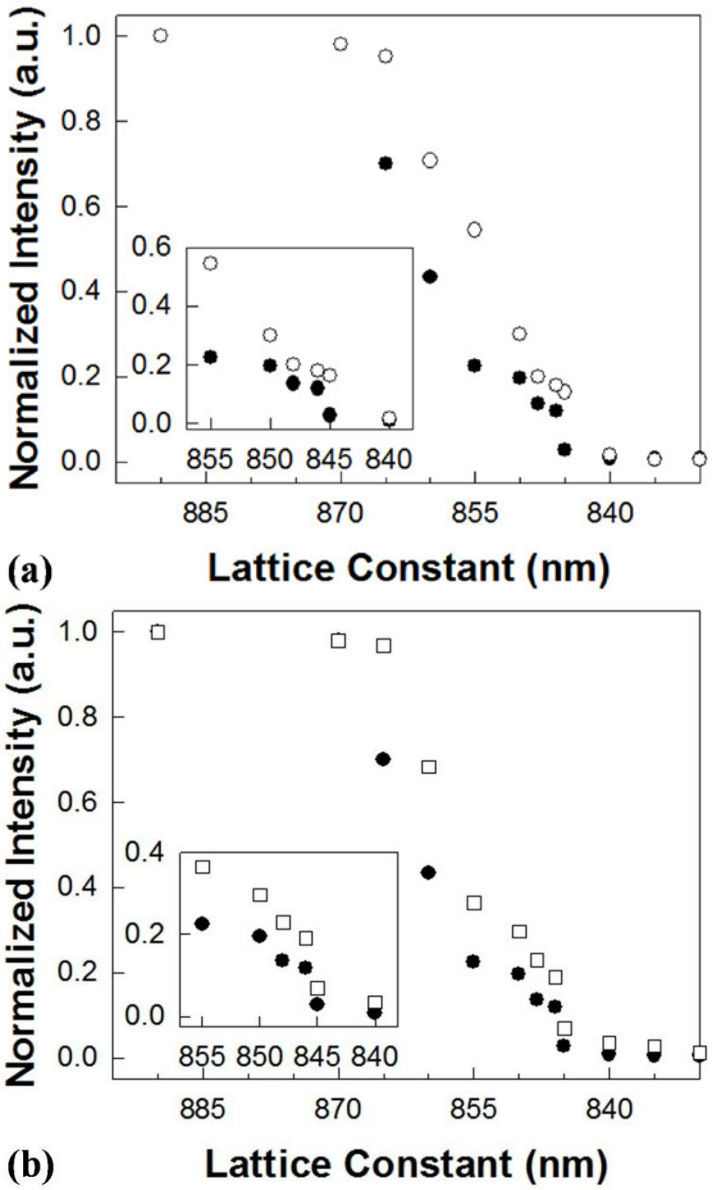


Figure 6.4 (a) Normalized transmitted intensity through an air-clad W1 PCW in SoS with $r$=0.25$a$, as a function of $a$ at λ=3.43μm plotted (a) in air (bold circles) and $C_2Cl_4$ (open circles) and (b) as a function of temperature at 25°C (bold circles) and 60°C (open squares). Insets magnify the data for devices between $a$=840nm and $a$=855nm.

At a=840nm and lower, the probed wavelength of 3.43μm is clearly within the photonic band gap; hence the transmitted power is zero. At lattice constants from a=845nm to a=850nm, the fixed wavelength ICL probes the W1 PCW guided mode at gradually decreasing group indices which translates experimentally to gradually increasing transmitted power. At a greater than 850nm, the probed wavelength propagates above the light line and the transmitted power reaches a maximum for the short W1 PCWs.

When the cladding refractive index is increased from n=1 in air to n=1.5 in $C_2Cl_4$, the W1 PCW guided mode is shifted down towards the dielectric band in Fig. 6.2(a). All simulated curves in Fig. 6.1(b) are shifted to longer wavelengths. As a result, the 3.43μm fixed wavelength source can be propagated through PCWs with smaller lattice constants. The phenomenon is experimentally observed by the shift of the transmitted intensity vs. lattice constant curves to shorter lattice constants. The effect of temperature can be similarly explained. Silicon has a positive temperature coefficient of refractive index at 3.43μm [17]. An increase in temperature increases the silicon refractive index so that the W1 PCW guided mode is again shifted down in frequency in the normalized dispersion diagram in Fig. 6.2(a). As a result, the 3.43μm source can be transmitted through PCWs with smaller lattice constants as temperature is increased, as observed in Fig. 6.4(b).

The position of the light line was validated by propagation loss measurements in Fig. 6.5. Devices with lengths 50μm, 100μm, 200μm and 400μm were fabricated at a=890nm, 870nm, 865nm, 860nm, 855nm, 850nm, 848nm and 846nm. It was ensured from ellipsometry that the selected chips for fabrication had h=585nm +/-1nm. Fig. 6.5(a) plots the corresponding propagation losses versus lattice constant. The measured propagation losses at a=846nm, 848nm and 850nm are 18dB/cm, 15dB/cm and 12dB/cm

respectively. At a=890nm, a=870nm, a=865nm, a=860nm and a=855nm, the propagation loss increases rapidly with increasing length of the PCW, reaching as high as 680dB/cm for a=865nm. It can thus be concluded that the ICL emission propagates above the light line for devices with a greater than 850nm.

The waveguide mode above the sapphire light line in the 2D PCW region propagates along the line defect due to the existence of the in-plane photonic bandgap. At the same time, the waveguide mode above the light line couples to the continuum of radiation modes and is thus continually radiated out of plane into the substrate. However, the devices in Fig. 6.4 are only 50μm (~ 60 periods) long and $n_g$ is small above the light line as observed from Fig. 6.2. Hence, for short PCWs, higher transmission is observed above the light line than below the light line where the PC waveguide mode is confined both laterally and vertically. As the PCW become longer, the out-of-plane losses dominate leading to huge propagation loss above the light line.

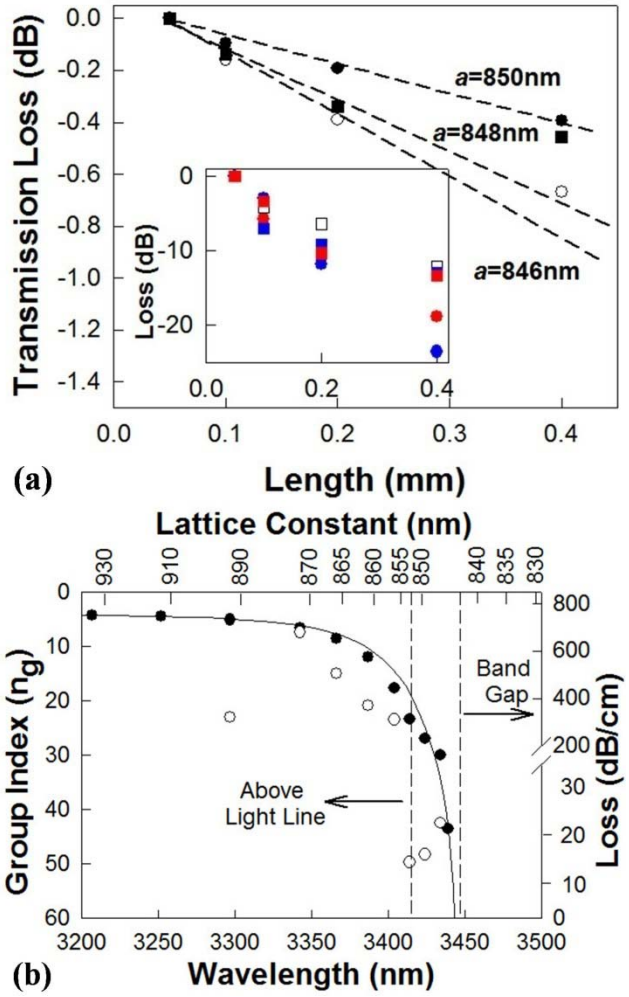


Figure 6.5 (a) Transmission losses in W1 PCWs in SoS below the light line for *a*=846nm (○), *a*=848nm (■) and *a*=850nm (●) at λ=3.43μm. Insets plot the propagation losses above the light line for devices with *a*=855nm (■), 860nm (■), 865nm (●), 870nm (●) and 890nm (□). (b) Solid line plot is the group index profile versus wavelength for W1 PCW in Fig. 6.2 with *a*=845nm. Estimated propagation group indices versus lattice constant are plotted with filled circles. Experimental propagation losses for measured devices are plotted versus lattice constant with open circles (right axis).

## 6.4 DISCUSSION

In Fig. 6.5(b), we estimate the approximate propagation group index at the ICL wavelength of 3.43μm for different lattice constants, by plotting the group index profile of the W1 PCW guided mode versus wavelength from Fig. 6.2. The guided mode dispersion profile in Fig. 6.2 and thus the $n_g$ profile versus wavelength is changed minimally with different h/a for the range of lattice constants studied here, except being shifted down in frequency with increasing a, h being nearly constant at 585nm. The $n_g$ plot is shifted versus a by the same wavelength magnitude as the offset of the transmission band edge in FDTD simulations in Fig. 6.1(b). We observe from Fig. 6.2 that at the intersection of the light line with the PCW guided mode, $n_g$~23. We thus estimate that in the a=850nm device, light propagates with $n_g$ ~23. Since the $n_g$ plot would just be shifted versus wavelength for other lattice constants, from the offsets calculated from Fig. 6.1(b), we estimate from Fig. 6.5(b) that at a=846nm and a=848nm, light propagates with $n_g$ approximately 30 and 27 respectively. The above propagation losses are better than 20dB/cm measured in ref. [13] at $n_g$=5. A W1 PCW with a=845nm, r/a=0.25 and h/a=0.69 in SoS would be expected to show similar propagation characteristics with a tunable laser source covering the wavelength range in Fig. 6.5(b).

One of the challenges of the SoS platform is the relatively high cladding index of sapphire which limits the PCW guiding bandwidth to only about 22nm in the present design. However, by lattice engineering the air hole diameter and PCW width, it is possible to obtain a larger PCW guiding bandwidth and is the object of future studies.

## 6.5 SUMMARY

In summary, we demonstrated the propagation characteristics of PCWs in SoS in the mid-IR. By engineering the lattice constant, we experimentally demonstrated the

transmission characteristics with a single wavelength source. In the guided mode region below the light line, propagation losses below 20dB/cm were observed for group indices $n_g$ greater than 20. Huge losses above the light line and zero transmission in the stop band were experimentally observed. Our method enables the design of guided wave photonic structures, using miniature PC devices in the mid-IR, even in the absence of mid-IR tunable sources.

## 6.6 REFERENCES


[1] M. Iqbal, M.A. Gleeson, B. Spaugh, F. Tybor, W.G. Gunn, M. Hochberg, T. Baehr-Jones, R.C. Bailey, and L.C. Gunn, IEEE J. Sel. Top. Quant. Electron. 16(3), 654 (2010).

[2] N. Skivesen, A. Tetu, M. Kristensen, J. Kjems, L. H. Frandsen, and P.I. Borel, Opt. Express 15(6), 3169 (2007).

[3] W-C. Lai, S. Chakravarty, Y. Zou, and R.T. Chen, Optics Lett. 37 (7), 1208 (2012)

[4] W-C. Lai, S Chakravarty, Y Zou, and R.T. Chen, Optics Lett. 38 (19), 3799-3802 (2013).

[5] W-C. Lai, S. Chakravarty, X. Wang, C. Lin, and R.T. Chen, Appl. Phys. Lett. 98 (2), 023304 (2011).

[6] W-C. Lai, S. Chakravarty, X. Wang, C. Lin, and R.T. Chen, Optics Lett. 36, 984 (2011).

[7] R. Soref, Nature Photon. 4, 495 (2010).

[8] Z. Cheng, X. Chen, C. Y. Wong, K. Xu, C. Fung, Y. Chen, and H. K. Tsang, IEEE Photon. J. 4, 104 (2012).

[9] T. Baehr-Jones, A. Spott, R. Ilic, A. Spott, B. Penkov, W. Asher, and M. Hochberg, Opt. Express 18, 12127 (2010).

[10] F. Li, S. D. Jackson, C. Grillet, E. Magi, D. Hudson, S. J. Madden, Y. Moghe, C. O'Brien, A. Read, S. G. Duvall, P. Atanackovic, B. J. Eggleton, and D. J. Moss, Opt. Express 19, 15212 (2011).

[11] A. Spott, Y. Liu, T. Baehr-Jones, R. Ilic, and M. Hochberg, Appl. Phys. Lett. 97, 213501 (2010).

[12] Y. Zou, H. Subbaraman, S. Chakravarty, X. Xu, A. Hosseini, W-C. Lai, P. Wray, and R. T. Chen, Opt. Lett. 39 (10), 3070 (2014).

[13] C. Reimer, M. Nedeljkovic, D.J.M. Stothard, M.O.S. Esnault, C. Reardon, L. O'Faolain, M. Dunn, G.Z. Mashanovich, and T.F. Krauss, Opt. Express 20 (28), 29361 (2012).

[14] R. Shankar, R. Leijssen, I. Bulu, and M. Loncar, Opt. Express 19 (6), 5579 (2011).

[15] Y. Zou, S. Chakravarty, L. Zhu, and R. T. Chen, Appl. Phys. Lett. 104, 141103 (2014)

[16] R. Shankar, I. Bulu, and M. Loncar, Appl. Phys. Lett. 102, 051108 (2013).

[17] B. J. Frey, D. B. Leviton, and T. Madison, Proc. SPIE 6273, 62732J (2006).

# Chapter 7: Mid-Infrared Holey and Slotted Photonic Crystal Waveguides in Silicon-on-Sapphire

## 7.1 Introduction

Slow light in PCWs [1] and PC slot waveguides [2, 3] has been used to reduce the optical absorption path length and achieve high detection sensitivity in on-chip optical absorption spectroscopy for the selective detection of volatile organic compounds [1, 2] and greenhouse gases [3] based on unique analyte absorption signatures in the near-infrared (near-IR). In the mid-infrared (mid-IR), most compounds and gases of interest, such as xylene and methane respectively, have at least two orders of magnitude larger absorption cross-sections than in the near-IR. Since silicon is optically transparent over the entire mid-IR till about 8μm [4], PCWs and PC slot waveguides in silicon-on-insulator (SOI) (till 3.7μm), silicon-on-sapphire (SoS) (till 5.5μm) and free-standing silicon membranes (till 8μm) can serve as the ideal platform for highly sensitive optical absorption spectroscopy on chip. Of these, the SoS platform provides a more rigid option for photonic sensing applications in the mid-IR compared to free-standing silicon membranes in SOI devices demonstrated by other researchers. PC research in the mid-IR has been limited by the need for bulky and expensive tunable laser sources [5, 6] and thus cannot be transitioned easily from the lab to the field.

Recently, we presented the first demonstration of photonic crystal waveguide (PCW) characteristics in SoS at the mid-IR wavelength 3.43μm of with a fixed wavelength interband cascade laser (ICL) [7]. While slowdown of light increases the interaction time between the analyte and the propagating optical mode, in PCWs the optical interaction in the slow light regime is limited primarily to the in-plane evanescent optical mode overlap within the holes of the PC lattice, in the first two or three rows adjacent to the PCW. It has been shown previously [8] that slot waveguides enhance the

optical intensity of the propagating mode in the low index slot within a high index ridge waveguide and photonic crystal waveguide. We previously demonstrated the enhanced detection sensitivity of VOCs in PC slot waveguides versus ridge and slot waveguides [9]. We previously demonstrated slot waveguides in the mid-IR in SoS [10]. However, in the mid-IR, structures such as the PC slot waveguide above, that enhance the optical mode overlap with the analyte together with the inherent slow light enhancement effects of the PCW, have not been experimentally demonstrated.

In this chapter, we experimentally investigate two structures that enable enhanced intensity overlap with the analyte within a PCW. The first structure is a holey PCW wherein smaller diameter holes than the bulk PC are etched along the propagation direction within the PCW at the antinodes of the PCW propagating mode. The second structure is a slotted PCW wherein a rectangular slot in etched uniformly at the center of the PCW from the input to the output.

## 7.2 Device Design

A schematic of the holey PCW is shown in Fig. 7.1(a). The holey PCW device comprises a W1.2 PCW with a single missing row of holes along the Γ–K direction in a hexagonal lattice of air holes in silicon, with lattice constant a. At the center of the PCW, a row of smaller holes with radius rs=0.625r, where r=0.25a is the radius of the holes in the bulk lattice, is etched at the lattice positions of the PC. W1.2 indicates that the width of the PCW at the onset of the taper is $1.2\times\sqrt{3}a$. Fig. 7.1(b) shows the dispersion diagram of the holey PCW obtained by 2D plane-wave expansion simulation using effective index n=2.91. The dispersion diagram shows the guided mode separated from the dielectric band by a stop gap. The light line for sapphire is superimposed. The electric field intensity profile of the propagating slow light mode, indicated by the red circle in

Fig. 7.1(b) is shown in Fig. 7.1(c). Fig. 7.1(d) is a cross section of the field intensity profile in Fig. 7.1(c) through one of the holes in the center of the holey PCW, showing the factor of 4 enhancement in the electric field intensity in the holes.

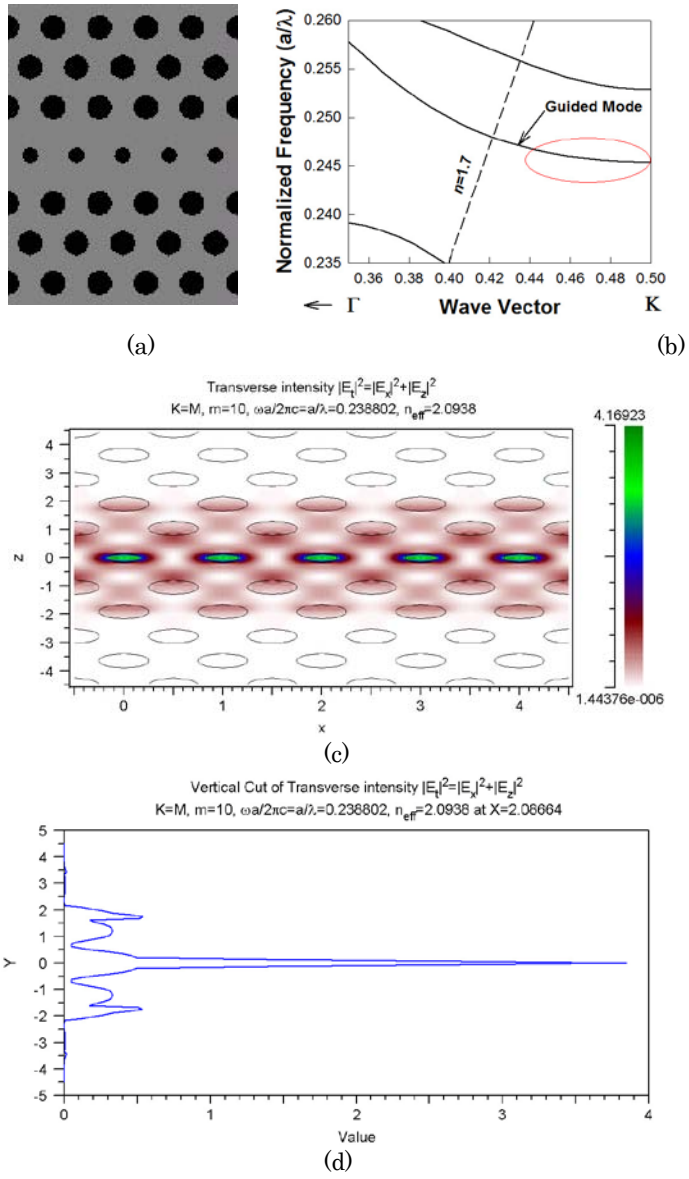


Figure 7. 1. (a) Schematic of the holey W1.2 PCW with a row of smaller air holes with radius *rs*=0.625*r*, in the center of the PCW. (b) Dispersion diagram of the device in (a) by plane-wave expansion. (c) Electric field intensity profile of the propagating slow light at the Brillouin zone boundary mode shown by red circle in (b). (d) Cross-section of the electric field intensity in (c) profile through the smaller air holes in the center of the PCW.

A schematic of the slotted PCW is shown in Fig. 7.2(a). The slotted PCW device comprises a W1.5 PCW with a single missing row of holes along the Γ–K direction in a hexagonal lattice of air holes in silicon, with lattice constant a. The radius of air holes is r=0.25a. At the center of the PCW, a rectangular slot with width s=0.155a, is etched from the input to the output. W1.5 indicates that the width of the PCW at the onset of the taper is $1.5\times\sqrt{3}a$. Fig. 7.2(b) shows the dispersion diagram of the holey PCW obtained by 2D plane-wave expansion simulation using effective index n=2.91. The electric field intensity profile of the propagating slow light mode, indicated by the red circle in Fig. 7.2(a) is shown in Fig. 7.2(c). Fig. 7.2(d) is a cross section of the field intensity profile in Fig. 7.2(c), showing the factor of 13 enhancement in the electric field intensity in the slot, larger than the holey PCW.

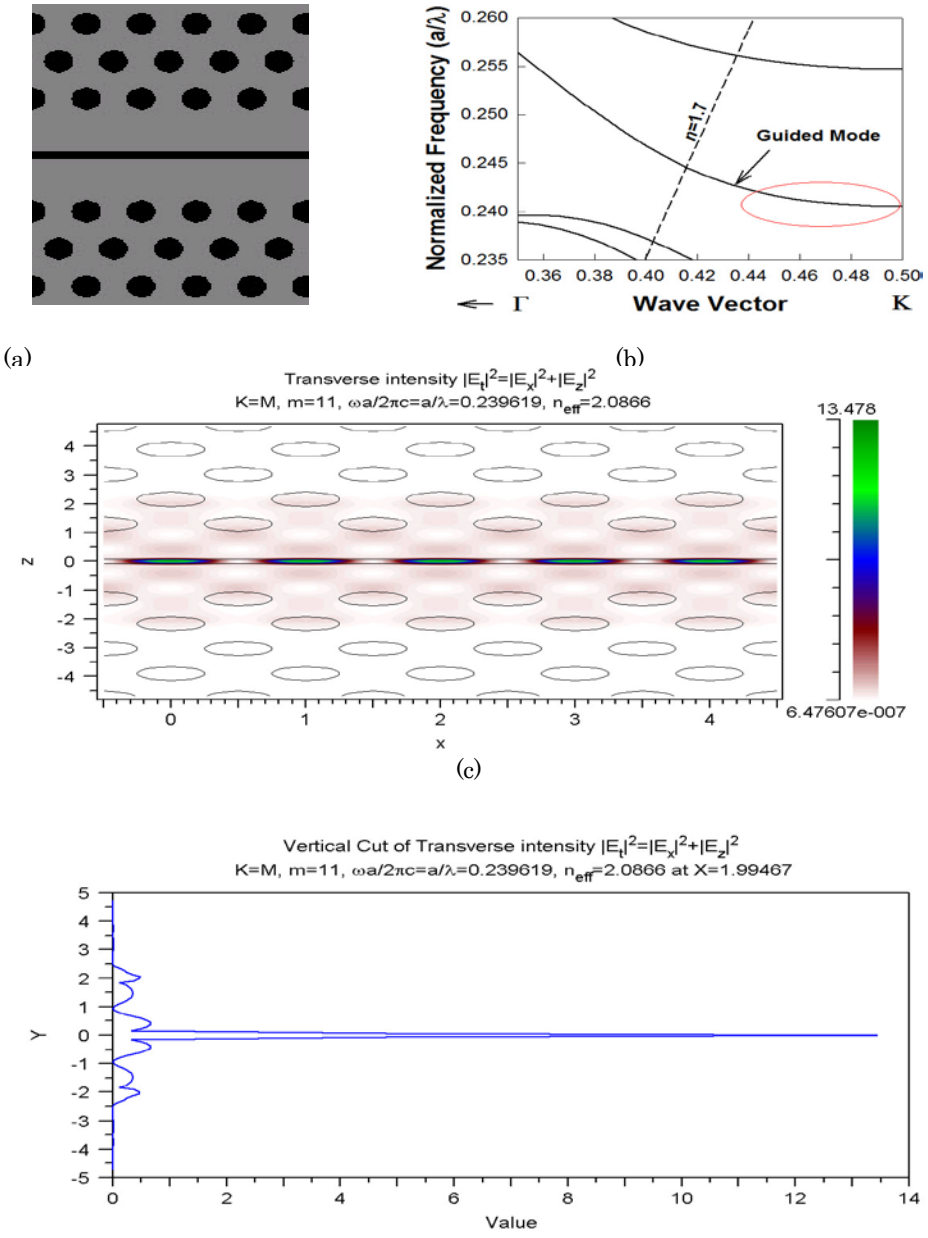


Figure 7.2 (a) Schematic of the slotted W1.5 PCW with a rectangular slot $s$=0.155$a$, in the center of the PCW. (b) Dispersion diagram of the device in (a) by plane-wave expansion. (c) Electric field intensity profile of the propagating slow light mode at the Brillouin zone boundary shown by red circle in (b). (d) Cross-section of the electric field intensity profile in (c).

Figs. 7.3 (a) and 7.3(b) show the electric field intensity profile and the cross-section intensity in a conventional W1 PCW. In contrast to the holey and slotted PCWs, the electric field intensity is primarily located in the dielectric (silicon in this case) and only interacts evanescently in-plane with the holes adjacent to the PCW.

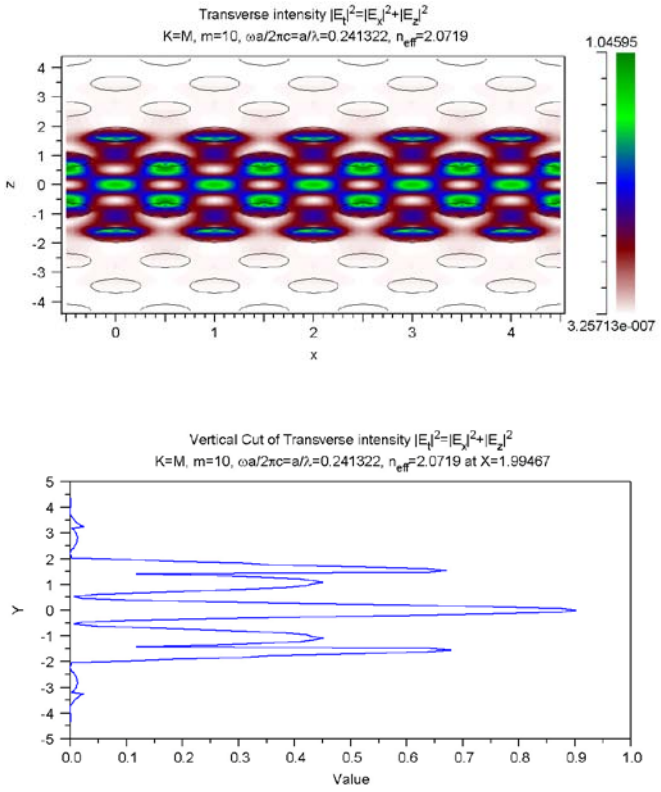


Figure 7.3. (a) Electric field intensity profile of the propagating slow light mode in a W1 PCW at the Brillouin zone boundary. (b) Cross-section of the electric field intensity profile in (a).

## 7.3 Device Fabrication and Characterization

The height of the silicon device layer according to wafer specifications is 600+/-60nm. In this work, the height of the silicon device layer was determined to be h=585nm from ellipsometry for the holey PCW and h=570nm from ellipsometry for the slot PCW.

h/a of the silicon slab was calculated accordingly for each lattice constant. Devices were fabricated using a combination of electron beam lithography and inductively coupled plasma etching. Scanning electron micrograph (SEM) images of the devices are shown in Fig. 7.4 and Fig. 7.5 respectively.

Light at 3.43μm from a source ICL is coupled into and out of the chip from a single mode $ZnF_4$ fiber from Thorlabs using subwavelength grating (SWG) couplers. The design and characterization of SWGs used here has been described in detail before [10]. As in previous research [7, 11], a PC group index taper is implemented at the input and output interfaces of the holey PCW with the ridge waveguide to reduce Fresnel reflection losses and enhance light coupling efficiency into the slow light guided mode. The PC group index taper is formed by gradually widening the PCW from W1.2 to W1.27 at the interface between the strip waveguide and holey PCW.

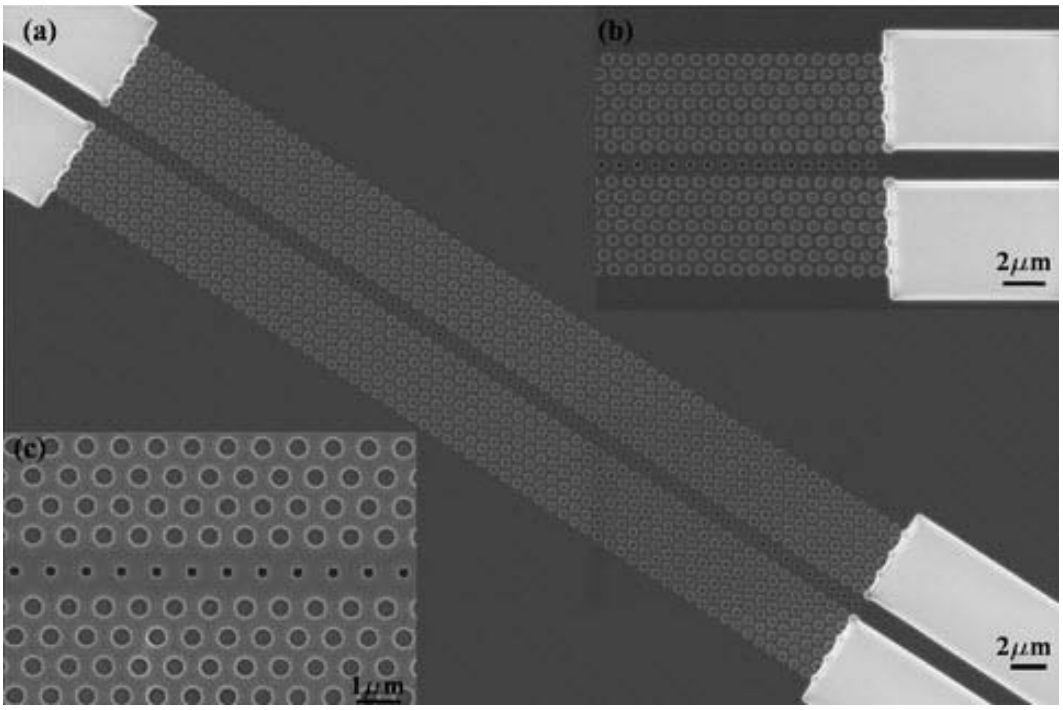


Figure 7.4 (a) Top view SEM image of the holey PCW. Top view magnified images showing the holey PCW (b) at the interface between the PCW and the input ridge waveguide in (a) and (c) near the center of the device.

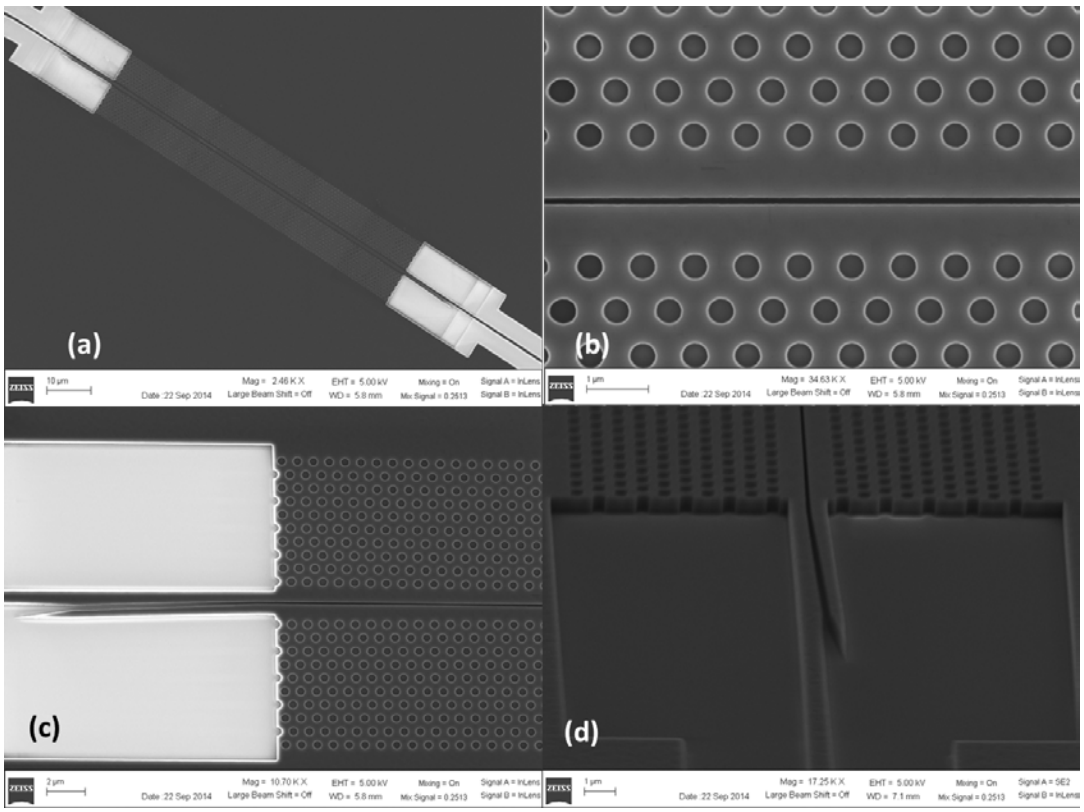


Figure 7.5. Top view SEM image of the slotted PCW. (b) Top view magnified images showing the slotted PCW near the center of the device image in (a). (c) Top view and (d) $70^{o}$ tilt view of the slot mode converter at the input (or output) of the slotted PCW.

In the slotted PCW, light is first coupled into the chip from SWGs into ridge waveguide. Light from the ridge waveguide is coupled next into a slot waveguide using a mode converter. Finally, light is coupled into the slotted PCW interface from the slot waveguide. The design, fabrication and characterization of the slot waveguide and mode converter used here has been described in detail previously [10]. Similar to the previous work, we chose a 130nm slot with 600nm rails as the input and output slot waveguide dimensions, which had resulted in highest optical coupling efficiency into the slot waveguides from input ridge waveguides. A PC group index taper is also implemented

to match group velocities from the slot waveguide into the slotted PCW. For the slotted PCW demonstrated here, the slotted PCW width is increased from W1.5 to W1.6 at the slotted PCW-slot waveguide interface. All device components for the respective holey and slotted PCWs are fabricated in the same step and post-processed as described before in Piranha/HF [7, 10].

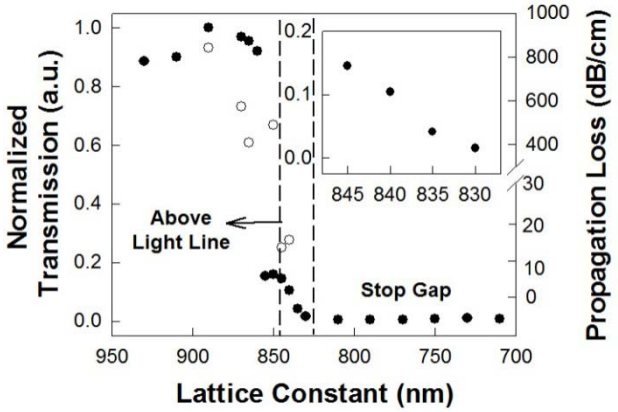


(a)

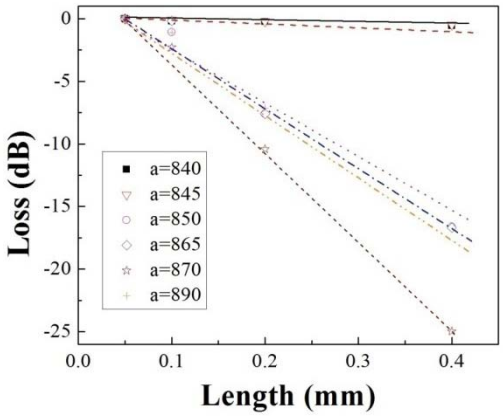


(b)

Figure 7.6: (a) Normalized transmitted intensity through an air-clad W1.2 holey PCW in SoS with $r$=0.25$a$, $rs$=0.625$r$ as a function of $a$ at λ=3.43μm plotted in air (bold circles). Propagation losses were measured for few devices (open circles). Insets magnify the data for devices between $a$=830nm and $a$=845nm. (b) Propagation loss for devices of different length at a=840nm (magenta), a=845nm (green), a=850nm (black), a=865nm (blue), a=870nm (yellow), and a=890nm (red).

The light from the output SWG for short 50μm (~60 periods) long holey PCW devices with several lattice constants but the same r/a is plotted in Fig. 7.6(a). The plot is normalized with respect to the highest and lowest power observed versus lattice constant. It is observed that for a less than 830nm, the output power from the devices is practically zero. Propagation loss measurements were done for several devices in Fig. 6(a) and plotted. Devices with lengths 50μm, 100μm, 200μm and 400μm were fabricated at a=840nm, 845nm, 850nm, 865nm, 870nm and 890nm. Transmission losses as observed in Fig. 7.6(b) were obtained. The lattice constants for propagation loss characterization were chosen based on a comparison with previous data [7] which showed a similar bulge in the short 50μm long PCWs at lattice constants for which the ICL emission propagates at wavelengths near the light line boundary. It was ensured from ellipsometry that the selected chips for fabrication had h=585nm +/-1nm. Fig. 7.6(a) also plots the corresponding propagation losses versus lattice constant (open circles). The measured propagation losses at a=840nm and 845nm are 15dB/cm and 13dB/cm respectively. At a=850nm, a=865nm, a=870nm, and a=890nm, the propagation loss increases rapidly with increasing length of the PCW, reaching as high as 900dB/cm for a=890nm. It can thus be concluded that the ICL emission propagates above the light line for devices with a greater than 845nm. The stop gap and light line boundaries are thus approximately demarcated based on the transmission measurements. In between the two dashed line, as shown in Fig. 7.6(a), light propagates in the holey PCW mode below the light line. As the lattice constant is decreased, from left to right in the inset of Fig. 7.6(a), the ICL emission propagates in the respective devices at higher group indices as a result of which the propagation loss increases and the transmitted intensity decreases.

Fig. 7.7 plot the transmission measurement results. ). The plot is normalized with respect to the highest and lowest power observed versus lattice constant. Similar to holey

PCW, as we tune the lattice constants, the output power varies. When lattice constants are smaller than 800nm, there are almost no output power. When lattice constants are larger than 860nm, the output power of these devices reaches the top. A clear power drop can be observed when lattice constant is bigger than 890nm that indicates the probe laser wavelength is at the other stop band. There is a similar bulge in the short 80μm long PCWs at lattice constants for which the ICL emission propagates at wavelengths near the light line boundary.

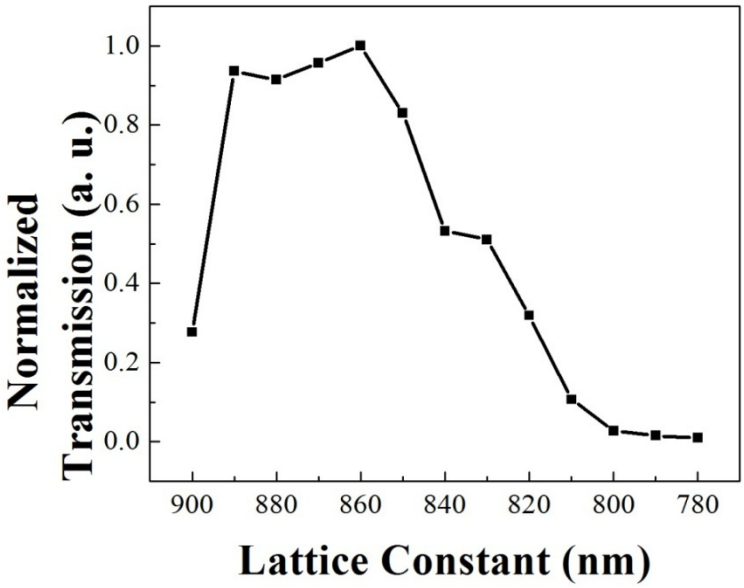


Fig. 7.7: Normalized transmitted intensity through an air-clad W1.5 slotted PCW in SoS with $r$=0.25$a$, $s$=0.155$a$ as a function of $a$ at λ=3.43μm plotted in air.

Fig. 7.8(a) plots the output power from the holey PCW devices when immersed in tetrachloroethylene ($C_2Cl_4$) compared with devices in air. $C_2Cl_4$ is practically non-absorbing at 3.43μm with a refractive index ~1.5 at room temperature. The absolute power measured by the photodetector is lower with $C_2Cl_4$ than with air cladding in Fig. 7.8(a). due to the lower modal confinement; however the normalized plot shows the

transmission profile shifted to lower lattice constants. Fig. 7.8(b) plots the output power as a function of temperature for varying lattice constant. The temperature is varied from 25°C to 60°C. The normalized plot also shows a shift of the transmission profile to lower lattice constants, with increasing temperature.

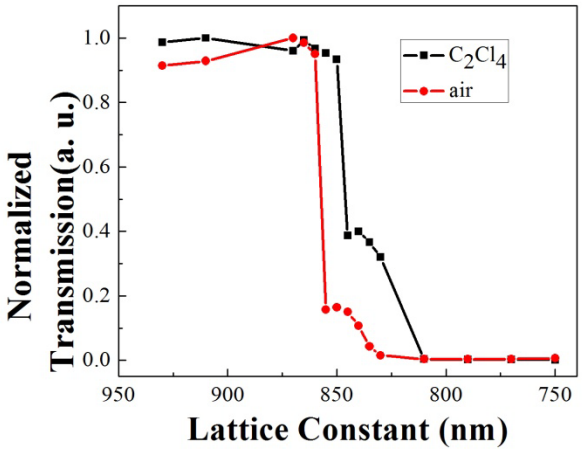


(a)

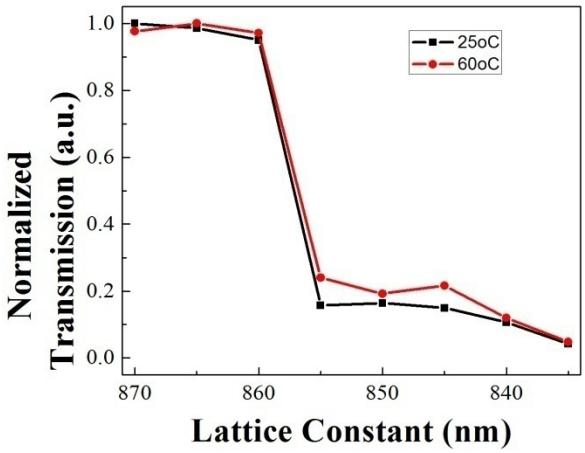


(b)

Fig. 7.8: Normalized transmitted intensity through an air-clad W1.2 holey PCW in SoS with $r$=0.25$a$, as a function of $a$ at λ=3.43μm plotted (a) in air (red) and $C_2Cl_4$ (black) and (b) as a function of temperature at 25°C (black) and 60°C (red).

Fig. 7.9 plots the output power from the slotted PCW devices as a function of temperature for varying lattice constant. The temperature is varied from 25$^{o}$C to 60$^{o}$C. It clearly shows the normalized transmission profiles shift to lower lattice constants with increase the refractive index of top cladding and temperature.

When the cladding refractive index is increased from n=1 in air to n=1.5 in $C_2Cl_4$, the holey PCW guided mode is shifted down towards the dielectric band in Fig. 7.1(b). All simulated curves in Fig. 7.1(b) shifted to longer wavelengths. As a result, the 3.43μm fixed wavelength source can be propagated through PCWs with smaller lattice constants. The phenomenon is experimentally observed by the shift of the transmitted intensity vs. lattice constant curves to shorter lattice constants. The effect of temperature can be similarly explained. Silicon has a positive temperature coefficient of refractive index at 3.43μm [13]. An increase in temperature increases the silicon refractive index so that the W1 PCW guided mode is again shifted down in frequency in the normalized dispersion diagram in Figs. 7.1(b) and 7.2(b). As a result, the 3.43μm source can be transmitted through PCWs with smaller lattice constants as temperature is increased, as observed in Figs. 7.8(b) and 7.9.

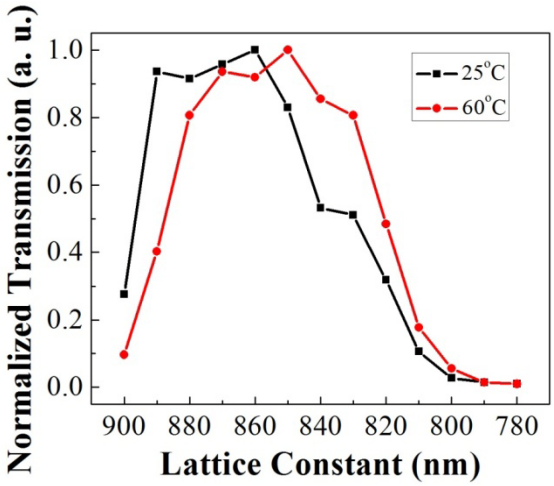


Fig. 7.9: Normalized transmitted intensity through an air-clad W1.5 slotted PCW in SoS with $r$=0.25$a$, $s$=0.155$a$, as a function of $a$ at λ=3.43μm plotted as a function of temperature at 25°C (black) and 60°C (red).

## 7.4 Summary

In summary, we demonstrated the propagation characteristics of holey and slotted PCWs in SoS in the mid-IR. By engineering the lattice constant, we experimentally demonstrated the transmission characteristics with a single wavelength source. In the guided mode region below the light line, propagation losses below 20dB/cm were observed. Huge losses above the light line and zero transmission in the stop band were experimentally observed. Our method enables the design of guided wave photonic structures, using miniature PC devices in the mid-IR, even in the absence of mid-IR tunable sources.

## 7.5 References

[1] W-C. Lai, S Chakravarty, Y Zou, and R.T. Chen, Optics Lett. 38 (19), 3799-3802 (2013).

[2] W-C. Lai, S. Chakravarty, X. Wang, C. Lin, and R.T. Chen, Appl. Phys. Lett. 98 (2), 023304 (2011).

[3] W-C. Lai, S. Chakravarty, X. Wang, C. Lin, and R.T. Chen, Optics Lett. 36, 984 (2011).

[4] R. Soref, Nature Photon. 4, 495 (2010).

[5] C. Reimer, M. Nedeljkovic, D.J.M. Stothard, M.O.S. Esnault, C. Reardon, L. O'Faolain, M. Dunn, G.Z. Mashanovich, and T.F. Krauss, Opt. Express 20 (28), 29361 (2012).

[6] R. Shankar, R. Leijssen, I. Bulu, and M. Loncar, Opt. Express 19 (6), 5579 (2011).

[7] Y. Zou, S. Chakravarty, P. Wray, R.T. Chen, Opt. Lett. (submitted)

[8] A. Di Falco, L. O'Faolain, T. F. Krauss, Photonics Nanostruct. Fundam. Appl. 6(1), 2008.

[9] W-C. Lai, Y. Zou, S. Chakravarty, L. Zhu, and R. T. Chen, Proc. SPIE 8990, Silicon Photonics IX, 8900Z (March 8, 2014)

[10] Y. Zou, H. Subbaraman, S. Chakravarty, X. Xu, A. Hosseini, W-C. Lai, P. Wray, and R. T. Chen, Opt. Lett. 39 (10), 3070 (2014).

[11] Y. Zou, S. Chakravarty, L. Zhu, and R. T. Chen, Appl. Phys. Lett. 104, 141103 (2014).

[12] R. Shankar, I. Bulu, and M. Loncar, Appl. Phys. Lett. 102, 051108 (2013).

[13] B. J. Frey, D. B. Leviton, and T. Madison, Proc. SPIE 6273, 62732J (2006).

# CHAPTER 8: SUMMARY

The objective of the dissertation was to employ the technology of two-dimensional photonic crystals on silicon platform to develop nanophotonic biological sensor in near-infrared and microphotonic chemical sensors in mid-infrared. In this section, I summarize chronologically the contributions of this work to the field of silicon photonics.

As discussed in Chapter 2 to 4, methods to improve device performance towards high sensitivity, high throughput, and high quality factor are demonstrated for silicon based biosensors. By engineering the photonic crystal microcavity in both cavity size and cavity-waveguide coupling condition, we successfully push the detection limit down to 50 femto-molar of biotin-avidin conjugates and resonance quality factor as high as 14,000 in PBS ambient. At the same time, using multi-mode interference (MMI) beam splitter and multiple photonic crystal microcavities coupled along the length of a single photonic crystal, we built a lab on a chip to sense multiple biomarkers simultaneously. Through better design of the group index tapers, we successfully integrated 64 sensors into a single device to form a high density sensor array for potential high throughput biological sensing application.

For mid infrared aspect, from Chapter 5 to 7, we have already demonstrated single mode strip waveguide and slot waveguide working at 3.4 μm wavelength. An efficient subwavelength grating coupler with 29% coupling efficiency and a robust strip-to-slot mode converter with 97% conversion efficiency are also experimental demonstrated. These achievements lay down a solid foundation for future sensing applications. This is the first demonstration of slot waveguide in silicon-on-sapphire. After that, we present the first demonstration of photonic crystal waveguide

characteristics in Silicon-on-sapphire at the mid-infrared wavelength 3.43μm of our fixed wavelength interband cascade laser. We demonstrate that by good control of device fabrication and device parameter engineering, photonic crystal waveguiding properties can be adequately determined in mid-IR PC devices to facilitate the accurate design of mid-IR PC sensors. Our method enables the design of guided wave photonic structures, using miniature PC devices in the mid-IR, even in the absence of mid-IR tunable sources. Following this characterization method, in order to enhance the light-matter interaction, we also proposed and demonstrated two structures that enable enhanced intensity overlap with the analyte within a photonic crystal waveguide: a holey photonic crystal waveguide and a slotted photonic crystal waveguide. Both these two devices are the first demonstration in mid-infrared region.

# Appendix A: Journal Publications

[1] **Yi Zou**, Swapnajit Chakravarty, Parker Wray, and Ray T. Chen, "Mid-infrared holey and slotted photonic crystal waveguides in silicon-on-sapphire" (on-going)

[2] **Yi Zou**, Swapnajit Chakravarty, Parker Wray, and Ray T. Chen, "Mid-infrared photonic crystal waveguides in silicon-on-sapphire" (under review)

[3] Xiaochuan Xu, Harish Subbaraman, Swapnajit Chakravarty, Amir Hosseini, John Covey, Yalin Yu, David Kwong, Yang Zhang, Wei-Cheng Lai, **Yi Zou**, Nanshu. Lu, and Ray T. Chen, “Flexible Single Crystal Silicon Nanomembrane Photonic Crystal Cavity”, ACS Nano (accepted) (2014).

[4]. Swapnajit Chakravarty, Amir Hosseini, Xiaochuan Xu, Liang Zhu, **Yi Zou**, and Ray T. Chen, "Analysis of ultra-high sensitivity configuration in chip-integrated photonic crystal microcavity bio-sensors," Applied Physics Letters, 104, 191109 (2014).

[5] **Yi Zou**, Harish Subbaraman, Swapnajit Chakravarty, Xiaochuan Xu, Amir Hosseini, Wei-Cheng Lai, Parker Wray and Ray T. Chen, “Grating-coupled silicon-on-sapphire integrated slot waveguides operating at mid-infrared wavelengths," Opt. Lett. 39, 3070-3073 (2014).

[6] **Yi Zou**, Swapnajit Chakravarty, Liang. Zhu, and Ray T. Chen, "The role of group index engineering in series-connected photonic crystal microcavities for high density sensor microarrays" Applied Physics Letters, 104, 141103 (2014).

[7] **Yi Zou**, Swapnajit Chakravarty, David Kwong, Wei-Cheng Lai, Xiaochuan Xu, Xiaohui. Lin, Amir. Hosseini, and Ray T. Chen, "Cavity-waveguide coupling engineered high sensitivity silicon photonic crystal microcavity biosensors with high yield," Selected Topics in Quantum Electronics, IEEE Journal of, vol.20, no.4, pp.1-10 (2014).

[8] Wei-Cheng Lai, Swapnajit Chakravarty, **Yi Zou**, and Ray. T. Chen, "Multiplexed detection of xylene and trichloroethylene in water by photonic crystal absorption spectroscopy," Opt. Lett. 38, 3799-3802 (2013).

[9] Wei-Cheng Lai, Swapnajit Chakravarty, **Yi Zou**, Yunbo Guo, and Ray T. Chen, "Slow light enhanced sensitivity of resonance modes in photonic crystal biosensors," Appl. Phys. Lett. 102, 041111 (2013).

[10] Swapnajit Chakravarty, Wei-Cheng Lai, **Yi Zou**, Harry A. Drabkin, Robert M. Gemmill, George R. Simon, Steve H. Chin, and Ray T. Chen, "Multiplexed specific label-free detection of NCI-H358 lung cancer cell line lysates with silicon based photonic crystal microcavity biosensors," Biosensors and Bioelectronics, 43(15) 50-55 (2013).

[11] Swapnajit Chakravarty*, **Yi Zou***, Wei-Cheng Lai, and Ray T. Chen, "Slow light engineering for high Q high sensitivity photonic crystal microcavity biosensors in silicon", Biosensor and Bioelectronics 38(1), 170-176 (2012)

*** joint first author**

[12] **Yi Zou**, Swapnajit Chakravarty, Wei-Cheng Lai, Che-Yun Lin, and Ray T. Chen, "Methods to array photonic crystal microcavities for high throughput high sensitivity biosensing on a silicon-chip based platform," Lab on a Chip 12, 2309-2312 (2012).

[13] Wei-Cheng Lai, Swapnajit Chakravarty, **Yi. Zou**, and Ray T. Chen, "Silicon nano-membrane based photonic crystal microcavities for high sensitivity bio-sensing.," Optics letters 37, 1208-10 (2012).

# Appendix B: Conference Publications


[1] **Yi Zou**, Swapnajit Chakravarty, Xiaochuan Xu, and Ray T. Chen, "Integrated Photonic Crystal Waveguides on Silicon-on-Sapphire for Volatile Organic Compound Sensing," Proc. SPIE, Photonic West (2015). (Accepted)

[2] **Yi Zou**, Swapnajit Chakravarty, Wei-Cheng Lai, Ray T. Chen, "Silicon Chip Based Near-Infrared and Mid-Infrared Optical Spectroscopy for Volatile Organic Compound Sensing," in CLEO: 2014 (Optical Society of America, 2014), Abstract ID STh3M.6.

[3] Chun-Ju Yang, **Yi Zou**, Swapnajit Chakravarty, Hai Yan, Zheng Wang, and Ray T. Chen, "Wide Dynamic Range Sensing in Photonic Crystal Microcavity Biosensors," in CLEO: 2014 (Optical Society of America, 2014), Abstract ID STh4H.5.

[4] Parker Wray, **Yi Zou**, Swapnajit Chakravarty, Ray T. Chen, "Silicon on Sapphire Chip Based Mid-Infrared Optical Spectroscopy for Detection of Chemical Warfare Simulant Triethyl phosphate," in CLEO: 2014 (Optical Society of America, 2014), Abstract ID AW1P.2.

[5] Hai Yan, **Yi Zou**, Chun-Ju Yang, Zheng Wang, Naimei Tang, Swapnajit Chakravarty, Ray T. Chen, "Photonic Crystal (PC) Waveguide Based Optical Filters for Dense Integration of High Sensitivity PC Biosensors," in CLEO: 2014 (Optical Society of America, 2014), Abstract ID JTu4A.94.

[6] Swapnajit Chakravarty, Naimei Tang, Hai Yan, Chun-Ju Yang, **Yi Zou**, Robert Gemmill, Q. Shen, Ray T. Chen, "Photonic Crystal Microarray Sensing of Cancer Cell Line Lysates," AACR Annual Meeting, 2014:5317.

[7] Swapnajit Chakravarty, Harish Subbaraman, **Yi Zou**, Wei-Cheng Lai, Ray T. Chen, "Methods to array photonic crystal microcavities for high throughput high

sensitivity biosensing on a silicon-chip based platform," Proc. SPIE 8990, Silicon Photonics IX, 89900S (March 8, 2014).

[8] **Yi Zou**, Harish Subbaraman, Swapnajit Chakravarty, Xiaochuan Xu, Amir Hosseini, Wei-Cheng Lai, and Ray T. Chen, “Integrated strip and slot waveguides in silicon-on-sapphire for Mid Infrared VOC detection in Water," Proc. SPIE, Photonic West (2014).

[9] Wei-Cheng Lai, **Yi Zou**, Swapnajit Chakravarty, Liang Zhu, and Ray T. Chen, “Comparative sensitivity analysis of integrated optical waveguides for near-infrared volatile organic compounds with 1ppb detection," Proc. SPIE, Photonic West (2014).

[10] Cheng-Chih Hsieh, Swapnajit Chakravarty, **Yi Zou**, Liang. Zhu, and Ray T. Chen, "High Sensitivity Biosensing Based on Symmetric Coupled Cavity Structure of Photonic Crystal Microcavities," in CLEO: 2013, OSA Technical Digest (Optical Society of America, 2013), paper CM2H.8.

[11] **Yi Zou**, Swapnajit Chakravarty, Wei-Cheng Lai, Cheng-Chih Hsieh, and Ray T. Chen, “High yield silicon photonic crystal microcavity biosensors with 100fM detection limit,” Proc. SPIE 8570, Frontiers in Biological Detection: From Nanosensors to Systems V, 857008 (March 5, 2013).

[12] Xingyu Zhang, Amir Hosseini, Xiaochuan Xu, Shiyi Wang, Qiwen Zhan, **Yi Zou**, Swapnajit Chakravarty, and Ray T. Chen; “Electric field sensor based on electro-optic polymer refilled silicon slot photonic crystal waveguide coupled with bowtie antenna,” Proc. SPIE 8624, Terahertz, RF, Millimeter, and Submillimeter-Wave Technology and Applications VI, 862418 (March 27, 2013).

[13] Wei-Cheng Lai, Swapnajit Chakravarty, **Yi Zou**, and Ray T. Chen; “Multiplexed selective detection and identification of TCE and xylene in water by on-chip

absorption spectroscopy," Proc. SPIE 8627, Integrated Optics: Devices, Materials, and Technologies XVII, 86270K (March 6, 2013).

[14] Swapnajit Chakravarty, Wei-Cheng Lai, **Yi Zou**, Robert M. Gemmill, and Ray T. Chen; "Silicon photonic crystal microarrays for high throughput label-free detection of lung cancer cell line lysates with sensitivity and specificity,". Proc. SPIE 8570, Frontiers in Biological Detection: From Nanosensors to Systems V, 857005 (March 5, 2013).

[15] **Yi Zou**, Swapnajit Chakravarty, Wei-Cheng Lai, Ray T. Chen, "Experimental detection of 1pico-molar concentration from high-Q photonic crystal microcavity biosensors," IEEE Photonics Conference (IPC) (2012).

[16] Wei-Cheng Lai, Swapnajit. Chakravarty, **Yi Zou**, and Ray T. Chen, "Loss Engineered High Sensitivity Photonic Crystal Microcavities for Multiplexed Detection of Biomolecules," in Frontiers in Optics Conference, OSA Technical Digest (online) (Optical Society of America, 2012), paper FM3H.5.

[17] Swapnajit Chakravarty, Wei-Cheng Lai, **Yi Zou**, and Ray T. Chen, "On-chip sensing of volatile organic compounds in water by hybrid polymer and silicon photonic-crystal slot-waveguide devices", Proc. SPIE, Photonic West (2012).

[18] Wei-Cheng Lai, Swapnajit Chakravarty, **Yi Zou**, Harry A. Drabkin, Robert M. Gemmill, George R. Simon, Steve H. Chin and Ray T. Chen, Silicon Photonic Crystal Microcavity Biosensors for Label Free Highly Sensitive and Specific Lung Cancer Detection, IEEE Photonics, 2012

[19] Swapnajit Chakravarty, Wei-Cheng Lai, **Yi Zou**, and Ray T. Chen, "Photonic crystal microcavity engineering and high-density bio-patterning for chip-integrated microarray applications", Proc. SPIE 8212, 82120A (2012).

[20] Swapnajit Chakravarty, Wei-Cheng Lai, **Yi Zou**, Cheyun Lin, Xiaolong Wang and Ray T. Chen, "Silicon-nanomembrane-based photonic crystal nanostructures for chip-integrated open sensor systems", Proc. SPIE 8198, 819802 (2011).

# Bibliography

## CHAPTER 1

[42] R. Soref, Nat. Photonics 4(8), 495 (2010).

[43] R. Soref, S. J. Emelett, and A. R. Buchwald, J. Opt. A 8(10), 840 (2006).

## CHAPTER 2

[44] T. Shoji, T. Tsuchizawa, T. Watanabe, K. Yamada, and H. Morita, "Low loss mode size converter from 0.3 μm square Si wire waveguides to single mode fibers," Electron. Lett., vol. 38, pp. 1669-1670, 2002.

[45] V. R. Almeida, R. R. Panepucci, and M. Lipson, "Nanotaper for compact mode conversion," Opt. Lett., vol. 28, pp. 1302-1304, 2003.

[46] K. K. Lee, D. R. Lim, D. Pang, C. Hoepfner, W-Y. Oh, K. Wada, L. C. Kimerling, K. P. Yap, and M. T. Doan, "Mode transformer for miniaturized optical circuits," Opt. Lett., vol. 30, pp. 498-500, 2005.

[47] S. J. McNab, N. Moll, and Y. A. Vlasov, "Ultra-low loss photonic integrated circuit with membrane-type photonic crystal waveguides," Opt. Express, vol. 11, pp. 2927 -2939, 2003.

[48] D. Taillaert, F. Van Laere, M. Ayre, W. Bogaerts, D. Van Thourhout, P. Bienstman, and R. Baets, "Grating Couplers for Coupling between Optical Fibers and Nanophotonic Waveguides," Jpn. J. Appl. Phys., vol. 45, pp. 6071–6077, 2006.

[49] Y. Tang, Z. Wang, L. Wosinski, U. Westergren, and S. He, "Highly efficient nonuniform grating coupler for silicon-on-insulator nanophotonic circuits," Opt. Lett., vol. 35, pp. 1290–1292, 2010.

[50] G. Roelkens, D. Vermeulen, D. Van Thourhout, R. Baets, S. Brision, P. Lyan, P. Gautier, and J. M. Fedeli, “High efficiency diffractive grating couplers for interfacing a single mode optical fiber with a nanophotonic silicon-on-insulator waveguide circuit,” Appl. Phys. Lett., vol. 92, pp. 131101-1-131101-3, 2008.

[51] F. Van Laere, G. Roelkens, M. Ayre, J. Schrauwen, D. Taillaert, D. Van Thourhout, T. F. Krauss, and R. Baets, “Compact and Highly Efficient Grating Couplers Between Optical Fiber and Nanophotonic Waveguides,” J. Lightwave Technol., vol. 25, pp. 151- 156, 2007.

[52] M. Antelius, K. B. Gylfason, and H. Sohlström, “An apodized SOI waveguide-to-fiber surface grating coupler for single lithography silicon photonics,” Opt. Express, vol. 19, pp. 3592-3598, 2011.

[53] F. Li, L. Wu, T. Li, M. Dubinovsky, S. Tang, and Ray T. Chen, “Unidirectional surface-normal waveguide grating coupler for wafer-scale MCM interconnect,” Proc. of the SPIE 3005, pp. 136-142, 1997.

[54] L. Liu, M. Pu, K. Yvind, and J. M. Hvam, “High-efficiency, large-bandwidth silicon-on-insulator grating coupler based on a fully-etched photonic crystal structure,” Appl. Phys. Lett., vol. 96, pp. 051126-1-051126-3, 2010.

[55] R. Halir, P. Cheben, S. Janz, D.-X. Xu, Í. Molina-Fernández, and J. G. Wangüemert-Pérez, “Waveguide grating coupler with subwavelength microstructures,” Opt. Lett., vol. 34, pp. 1408-1410, 2009.

[56] R. Halir, P. Cheben, J. H. Schmid, R. Ma, D. Bedard, S. Janz, D. X. Xu, A. Densmore, J. Lapointe, and ´I. Molina-Fern´andez, “Continuously apodized fiber-to-chip surface grating coupler with refractive index engineered subwavelength structure,” Opt. Lett., vol. 35, pp. 3243–3245, 2010.

[57] C. Xia and H. K. Tsang, “Nanoholes grating couplers for coupling between silicon-on-insulator waveguides and optical fibers,” IEEE Photonics Journal, vol. 1, pp. 184- 190, 2009.

[58] X. Xu, H. Subbaraman, J. Covey, D. Kwong, A. Hosseini, and R. T. Chen, “Complementary metal–oxide–semiconductor compatible high efficiency subwavelength grating couplers for silicon integrated photonics,” Appl. Phys. Lett., vol. 101, pp. 031109-1-031109-3, 2012.

[59] H. Subbaraman, X. Xu, J. Covey, and R. T. Chen, "Efficient light coupling into in-plane semiconductor nanomembrane photonic devices utilizing a sub-wavelength grating coupler," Opt. Express, vol. 20, pp. 20659-20665, 2012.

[60] M. Iqbal, M. A. Gleeson, B. Spaugh, F. Tybor, W. G. Gunn, M. Hochberg, T. Baehr-Jones, R. C. Bailey, and L. C. Gunn, “Label-free biosensor arrays based on silicon ring resonators and high-speed optical scanning instrumentation,” IEEE J. Sel. Top. Quant. Electron., vol. 16, pp. 654-661, 2010.

[61] C. F. Carlborg, K. B. Gylfason, A. Kazmierczak, F. Dortu, M. J. Banuls Polo, A. Maquieira Catala, G. M. Kresbach, H. Sohlstrom, T. Moh, L. Vivien, J. Popplewell, G. Ronan, C. A. Barrios, G. Stemme, and W. van der Winjgaart, “A packaged optical slot-waveguide ring resonator sensor array for multiplex label-free assays in labs-on-chips,” Lab Chip, vol. 10, pp. 281-290, 2010.

[62] A. Densmore, M. Vachon, D. X. Xu, S. Janz, R. Ma, Y. H. Li, G. Lopinski, A. Delage, J. Lapointe, C. C. Luebbert, Q.Y. Liu, P. Cheben, and J.H. Schmid, “Silicon photonic wire biosensor array for multiplexed real-time and label-free molecular detection,” Opt. Lett., vol. 34, pp. 3598 -3600, 2009.

[63] H. Sipova, S. Zhang, A. M. Dudley, D. Galas, K. Wang, and J. Homola, “Surface plasmon resonance biosensor for rapid label-free detection of microribonucleic acid at subfemtomole level,” Anal. Chem., vol. 82, pp. 10110-10115, 2010.

[64] B. S. Song, S. Noda, T. Asano and Y. Akahane, “Ultra-high-Q photonic double heterostructure nanocavity”, Nat. Mater., vol. 4, pp. 207-210, 2005.

[65] S. Chakravarty, Y. Zou, W. Lai, and R. T. Chen, “Slow light engineering for high Q high sensitivity photonic crystal microcavity biosensors in silicon,” Biosens. Bioelectron., vol. 38, pp. 170-176, 2012.

[66] W. C. Lai, S. Chakravarty, Y. Zou and R. T. Chen, “Silicon nano-membrane based photonic crystal microcavities for high sensitivity bio-sensing,” Opt. Lett., vol. 37, pp. 1208-1210, 2012.

[67] Y. Zou, S. Chakravarty, W. Lai, C. Lin and R. T. Chen, “Methods to array photonic crystal microcavities for high throughput high sensitivity biosensing on a silicon-chip based platform,” Lab Chip, vol. 12, pp. 2309-2312, 2012.

[68] P. Yeh, A. Yariv, and C.-S. Hong, “Electromagnetic propagation in periodic stratified media. I. General theory,” J. Opt. Soc. Am., vol. 67, pp. 423-438, 1977.

[69] S. M. Rytov, “Electromagnetic properties of a finely stratified medium,” Sov. Phys. JETP, vol. 2, pp. 466-475, 1956.

[70] W-C. Lai, S. Chakravarty, Y. Zou, and R.T. Chen, “Slow light enhanced sensitivity of resonance modes in photonic crystal biosensors,” Appl. Phys. Lett., vol. 102, pp. 041111-1-041111-4, 2013.

[71] C. Y. Lin, X. Wang, S. Chakravarty, B. S. Lee, W. C. Lai, and R. T. Chen, “Wideband group velocity independent coupling into slow light silicon photonic crystal waveguide,” Appl. Phys. Lett., vol. 97, pp. 183302-1-183302-3, 2010.

[72] S. A. Schulz, L. O'Faolain, D. M. Beggs, T. P. White, A. Melloni, and T. F. Krauss, “Dispersion engineered slow light in photonic crystals: a comparison,” J. Opt., vol. 12, pp. 104004-1-104004-10, 2010.

[73] D. Dorfner, T. Zabel, T. Hürlimann, N. Hauke, L. Frandsen, U. Rant, G. Abstreiter, and J. Finley, “Photonic crystal nanostructures for optical biosensing applications,” Biosens. Bioelectron., vol. 24, pp. 3688–3692, 2009.

[74] H. Li, and X. Fan, “Characterization of sensing capability of optofluidic ring resonator biosensors,” Appl. Phys. Lett. Vol. 97, pp. 011105, 2010.

[75] C. A. Barrios, “Optical Slot-Waveguide Based Biochemical Sensors,” Sensors vol. 9, pp. 4751–4765, 2009.

[76] K. De Vos, I. Bartolozzi, E. Schacht, P. Bienstman, and R. Baets, “Silicon-on-insulator microring resonator for sensitive and label-free biosensing,” Opt. Express vol. 15, pp. 7610–7615, 2007.

[77] M. Lee, and P. M. Fauchet, “Two-dimensional silicon photonic crystal based biosensing platform for protein detection,” Opt. Express vol. 15, pp. 4530–4535, 2007.

[78] C. Kang, C. T. Phare, Y. A. Vlasov, S. Assefa, and S. M. Weiss, “Photonic crystal slab sensor with enhanced surface area,” Opt. Express vol. 18, pp. 27930-27937, 2010.

[79] S. Mandal, and D. Erickson, “Nanoscale optofluidic sensor arrays,” Opt. Exp. vol. 16, pp. 1623–1631, 2008.

[80] M. G. Scullion, A. Di Falco, and T. F. Krauss, “Slotted photonic crystal cavities with integrated microfluidics for biosensing applications,” Biosens. Bioelectron. vol. 27, pp. 101-105, 2011.

[81] S. Zlatanovic, L. W. Mirkarimi, M. M. Sigalas, M. A. Bynum, E. Chow, K. M. Robotti, G. W. Burr, S. Esener, and A. Grot, “Photonic crystal microcavity sensor for ultracompact monitoring of reaction kinetics and protein concentration,” Sensors and Actuators B, vol. 141, pp. 13–19, 2009.

[82] S. Hachuda, S. Otsuka, S. Kita, T. Isono, M. Narimatsu, K. Watanabe, Y. Goshima, T. Baba, “Selective detection of sub-atto-molar streptavidin in 1013-fold impure sample using photonic crystal nanolaser sensor”, Opt. Express, vol. 21 iss. 10, pp. 12815-12821, 2013.

[83] T-Y. Chang, M. Huang, A. A. Yanik, H-Y Tsai, P. Shi, S. Aksu, M. F. Yanik and H. Altug, “Large-Scale Plasmonic Microarrays for Label-Free High-Throughput Screening,” Lab Chip vol. 11, pp. 3596-3602, 2011.

[84] Z. Chen, S. M. Tabakman, A. P. Goodwin, M. G. Kattah, D. Daranciang, X. R. Wang, G. Y. Zhang, X. L. Li, Z. Liu, P. J. Utz, K. L. Jiang, S. S. Fan and H. J. Dai, “Protein microarrays with carbon nanotubes as multicolor Raman labels,” Nat. Biotechnol., vol. 26, pp. 1285–1292, 2008.

## CHAPTER 3

[1] M. F. Templin, D. Stoll, J. M. Schwenk, O. Potz, S. Kramer, and T. O. Joos, Proteomics, 2003,3, 2155.

[2] M. Iqbal, M. A. Gleeson, B. Spaugh, F. Tybor, W. G. Gunn, M. Hochberg, T. Baehr-Jones, R. C. Bailey, and L. C. Gunn, IEEE J. Sel. Top. Quant. Electron. 2010, 16, 654.

[3] C. F. Carlborg, K. B. Gylfason, A. Kazmierczak, F. Dortu, M. J. Banuls Polo, A. MaquieiraCatala, G. M. Kresbach, H. Sohlstrom, T. Moh, L. Vivien, J. Popplewell, G. Ronan, C. A. Barrios, G. Stemme, and W. van der Winjgaart, Lab Chip 2010, 10, 281.

[4] A. Densmore, M. Vachon, D. X. Xu, S. Janz, R. Ma, Y. H. Li, G. Lopinski, A. Delage, J. Lapointe, C. C. Luebbert, Q. Y. Liu, P. Cheben, and J. H. Schmid, Opt. Lett. 2009, 34, 3598.

[5] H. Sipova, S. Zhang, A. M. Dudley, D. Galas, K. Wang, and J. Homola, Anal. Chem. 2010, 82, 10110.

[6] S. Chakravarty, J. Topoľančik, P. Bhattacharya, S. Chakrabarti, Y. Kang, and M. E. Meyerhoff, Opt. Lett. 2005, 30, 2578.

[7] W-C. Lai, S. Chakravarty, Y. Zou, C-Y. Lin, and R.T. Chen, Optics Lett. 2012, 37, 1208.

[8] S. Pal, E. Guillermain, R. Sriram, B. L. Miller, and P. M. Fauchet, Biosens. and Bioelectron. 2011, 26, 4024.

[9] A. Hosseini, D. N. Kwong, Y. Zhang; H. Subbaraman, X. Xu and R. T. Chen, IEEE J. Sel. Top. Quant. Electron. 2011, 17, 510.

[10] Y. Akahane, T. Asano, B-S. Song, and S. Noda, Nature 2003, 425, 944.

[11] A. Subramanian, S. J. Kennel, P. I. Oden, K. B. Jacobson, J. Woodward, and M. J. Doktycz, Enzyme and Microbial Tech.1999, 24, 26.

[12] C-Y. Lin, X. Wang, S. Chakravarty, B-S. Lee, W-C. Lai, and R. T. Chen, Appl. Phys. Lett. 2010, 97, 183302.

[13] S. Zlatanovic, L. W. Mirkarimi, M. M. Sigalas, M. A. Bynum, E. Chow, K. M. Robotti, G. W. Burr, S. Esener, and A. Grot, Sens. and Actuators. B 2009, 13, 141.

## CHAPTER 4

[1] T. Baba, Nature Photonics 2, 465 (2008).

[2] M. Povinelli, S. Johnson, and J. Joannopoulos, Opt. Express 13, 7145 (2005).

[3] C. Y. Lin, H. Subbaraman, A. Hosseini, X. Wang, L. Zhu, and R. T. Chen, Appl. Phys. Lett. 101, 051101 (2012).

[4] D. M. Beggs, T. P. White, L. O'Faolain, and T. F. Krauss, Opt. Lett. 33, 147 (2008).

[5] Y. Jiang, W. Jiang, L. Gu, X. Chen, and R. T. Chen, Appl. Phys. Lett. 87, 221105 (2005).

[6] L. Gu, W. Jiang, X. Chen, L. Wang, and R. T. Chen, Appl. Phys. Lett. 90, 071105 (2007).

[7] X. Wang, S. Chakravarty, B. S. Lee, C. -Y. Lin, and R. T. Chen, Opt. Lett. 34, 3202 (2009).

[8] C. -Y. Lin, X. Wang, S. Chakravarty, B. S. Lee, W. Lai, J. Luo, A. K. -Y. Jen, and R. T. Chen, Appl. Phys. Lett. 97, 093304 (2010).

[9] A. Hosseini, X. Xu, H. Subbaraman, C. Lin, S. Rahimi, and R. T. Chen, Opt. Express 20, 12318-12325 (2012).

[10] W. -C. Lai, S. Chakravarty, Y. Zou, and R. Chen, Opt. Lett. 37, 1208 (2012).

[11] S. Chakravarty, Y. Zou, W. Lai, and R. T. Chen, Biosens. Bioelectron. 38, 170 (2012).

[12] D. Dorfner, T. Zabel, T. Hürlimann, N. Hauke, L. Frandsen, U. Rant, G. Abstreiter, and J. Finley, Biosens. Bioelectron. 24, 3688 (2009).

[13] M. Lee, and P. M. Fauchet, Opt. Express 15, 4530 (2007).

[14] S. Zlatanovic, L. W. Mirkarimi, M. M. Sigalas, M. A. Bynum, E. Chow, K. M. Robotti, G. W. Burr, S. Esener, and A. Grot, Sensors and Actuators B, 141, 13 (2009).

[15]Y. Zou, S. Chakravarty, D. Kwong, W. Lai, X. Xu, X. Lin, A. Hosseini, and R. T. Chen, IEEE J. Sel. Top. Quantum Electron. 20(4), 6900710 (2014).

[16] Y. Zou, S. Chakravarty, W. Lai, C. Lin and R. T. Chen, Lab Chip 12, 2309 (2012).

[17] E. Guillermain, and P. M. Fauchet, Mater. Res. Soc. Symp. Proc. 1191, 1191-OO11-06 (2009)

[18] S. Mandal, and D. Erickson, Opt. Exp. 16(3), 1623 (2008).

[19] W. -C. Lai, S. Chakravarty, Y. Zou, Y. Guo, and R.T. Chen, Appl. Phys. Lett. 102, 041111 (2013).

[20] P. Pottier, M. Gnan, and R. M. De La Rue, Opt. Express 15, 6569 (2007).

[21] C. Y. Lin, X. Wang, S. Chakravarty, B. S. Lee, W. Lai, and R. T. Chen, Appl. Phys. Lett. 97, 183302 (2010).

[22] X. Xu, H. Subbaraman, J. Covey, D. Kwong, A. Hosseini, and R. T. Chen, Appl. Phys. Lett. 101, 031109 (2012).

[23] H. Takano, B-S. Song, T. Asano, and S. Noda, Opt. Exp. 14 (8), 3491 (2006).

[24] Y. Akahane, T. Asano, B-S. Song, and S. Noda, Nature 425, 944 (2003).

[25] B. -S. Song, T. Asano, Y. Akahane, Y. Tanaka, and S. Noda, J. Lightwave Tech. 23(3), 1449-1455 (2005).

## CHAPTER 5

[1] R. Soref, Nat. Photonics 4(8), 495 (2010).

[2] R. Soref, S. J. Emelett, and A. R. Buchwald, J. Opt. A 8(10), 840 (2006).

[3] X. Chen Z. Cheng, C. Y. Wong, K. Xu, C. Fung, Y. Chen, and H. K. Tsang, IEEE Photon. J. 4(1), 104 (2012).

[4] T. Baehr-Jones, A. Spott, R. Ilic, A. Spott, B. Penkov, W. Asher, and M. Hochberg, Opt. Express 18(12), 12127 (2010).

[5] R. Shankar, I. Bulu, and M. Loncar, Appl. Phys.Lett. 102(5), 051108 (2013).

[6] F. Li, S. D. Jackson, C. Grillet, E. Magi, D. Hudson, S. J. Madden, Y. Moghe, C. O'Brien, A. Read, S. G. Duvall, P. Atanackovic, B. J. Eggleton, and D. J. Moss, Opt. Express 19(16), 15212 (2011).

[7] A. Spott, Y. Liu, T. Baehr-Jones, R. Ilic, and M. Hochberg, Appl. Phys. Lett. 97(21), 213501 (2010).

[8] C. Y. Wong, Z. Cheng, X. Chen, K. Xu, C. K. Y. Fung, Y. M. Chen, and H. K. Tsang, IEEE Photon. J. 4(4), 1095 (2012).

[9] V. R. Almeida, Q. Xu, C. A. Barrios, and M. Lipson, Opt. Lett. 29(11), 1209 (2004).

[10] Q. Xu, V. R. Almeida, R. R. Panepucci, and M. Lipson, Opt. Lett. 29(14), 1626 (2004).

[11] Z. Wang, N. Zhu, Y. Tang, L. Wosinski, D. Dai, and S. He, Opt. Lett. 34(10) 1498 (2009).

[12] Y. Liu, T. Baehr-Jones, J. Li, A. Pomerene, and M. Hochberg, IEEE Photon. Technol. Lett. 23(20), 1496 (2011).

[13] R. Palmer, L. Alloatti, D. Korn, W. Heni, P. C. Schindler, J. Bolten, M. Karl, M. Waldow, T. Wahlbrink, W. Freude, C. Koos, and J. Leuthold, IEEE Photon. J. 5(1), 2200409 (2013).

[14] X. Xu, H. Subbaraman, J. Covey, D. Kwong, A. Hosseini, and R. T. Chen, Appl. Phys. Lett. 101, 031109 (2012).

[15] Y. Zou, S. Chakravarty, D. Kwong, W. Lai, X. Xu, X. Lin, A. Hosseini, and R. T. Chen, IEEE J. Sel. Top. Quantum Electron. 20(4), 6900710 (2014).

[16] S. M. Rytov, Sov. Phys. J. Exp. Theor. Phys. 2, 466 (1956).

## CHAPTER 6

[1] M. Iqbal, M.A. Gleeson, B. Spaugh, F. Tybor, W.G. Gunn, M. Hochberg, T. Baehr-Jones, R.C. Bailey, and L.C. Gunn, IEEE J. Sel. Top. Quant. Electron. 16(3), 654 (2010).

[2] N. Skivesen, A. Tetu, M. Kristensen, J. Kjems, L. H. Frandsen, and P.I. Borel, Opt. Express 15(6), 3169 (2007).

[3] W-C. Lai, S. Chakravarty, Y. Zou, and R.T. Chen, Optics Lett. 37 (7), 1208 (2012)

[4] W-C. Lai, S Chakravarty, Y Zou, and R.T. Chen, Optics Lett. 38 (19), 3799-3802 (2013).

[5] W-C. Lai, S. Chakravarty, X. Wang, C. Lin, and R.T. Chen, Appl. Phys. Lett. 98 (2), 023304 (2011).

[6] W-C. Lai, S. Chakravarty, X. Wang, C. Lin, and R.T. Chen, Optics Lett. 36, 984 (2011).

[7] R. Soref, Nature Photon. 4, 495 (2010).

[8] Z. Cheng, X. Chen, C. Y. Wong, K. Xu, C. Fung, Y. Chen, and H. K. Tsang, IEEE Photon. J. 4, 104 (2012).

[9] T. Baehr-Jones, A. Spott, R. Ilic, A. Spott, B. Penkov, W. Asher, and M. Hochberg, Opt. Express 18, 12127 (2010).

[10] F. Li, S. D. Jackson, C. Grillet, E. Magi, D. Hudson, S. J. Madden, Y. Moghe, C. O'Brien, A. Read, S. G. Duvall, P. Atanackovic, B. J. Eggleton, and D. J. Moss, Opt. Express 19, 15212 (2011).

[11] A. Spott, Y. Liu, T. Baehr-Jones, R. Ilic, and M. Hochberg, Appl. Phys. Lett. 97, 213501 (2010).

[12] Y. Zou, H. Subbaraman, S. Chakravarty, X. Xu, A. Hosseini, W-C. Lai, P. Wray, and R. T. Chen, Opt. Lett. 39 (10), 3070 (2014).

[13] C. Reimer, M. Nedeljkovic, D.J.M. Stothard, M.O.S. Esnault, C. Reardon, L. O'Faolain, M. Dunn, G.Z. Mashanovich, and T.F. Krauss, Opt. Express 20 (28), 29361 (2012).

[14] R. Shankar, R. Leijssen, I. Bulu, and M. Loncar, Opt. Express 19 (6), 5579 (2011).

[15] Y. Zou, S. Chakravarty, L. Zhu, and R. T. Chen, Appl. Phys. Lett. 104, 141103 (2014)

[16] R. Shankar, I. Bulu, and M. Loncar, Appl. Phys. Lett. 102, 051108 (2013).

[17] B. J. Frey, D. B. Leviton, and T. Madison, Proc. SPIE 6273, 62732J (2006).

## CHAPTER 7

[1] W-C. Lai, S Chakravarty, Y Zou, and R.T. Chen, Optics Lett. 38 (19), 3799-3802 (2013).

[2] W-C. Lai, S. Chakravarty, X. Wang, C. Lin, and R.T. Chen, Appl. Phys. Lett. 98 (2), 023304 (2011).

[3] W-C. Lai, S. Chakravarty, X. Wang, C. Lin, and R.T. Chen, Optics Lett. 36, 984 (2011).

[4] R. Soref, Nature Photon. 4, 495 (2010).

[5] C. Reimer, M. Nedeljkovic, D.J.M. Stothard, M.O.S. Esnault, C. Reardon, L. O'Faolain, M. Dunn, G.Z. Mashanovich, and T.F. Krauss, Opt. Express 20 (28), 29361 (2012).

[6] R. Shankar, R. Leijssen, I. Bulu, and M. Loncar, Opt. Express 19 (6), 5579 (2011).

[7] Y. Zou, S. Chakravarty, P. Wray, R.T. Chen, Opt. Lett. (submitted)

[8] A. Di Falco, L. O'Faolain, T. F. Krauss, Photonics Nanostruct. Fundam. Appl. 6(1), 2008.

[9] W-C. Lai, Y. Zou, S. Chakravarty, L. Zhu, and R. T. Chen, Proc. SPIE 8990, Silicon Photonics IX, 8900Z (March 8, 2014)

[10] Y. Zou, H. Subbaraman, S. Chakravarty, X. Xu, A. Hosseini, W-C. Lai, P. Wray, and R. T. Chen, Opt. Lett. 39 (10), 3070 (2014).

[11] Y. Zou, S. Chakravarty, L. Zhu, and R. T. Chen, Appl. Phys. Lett. 104, 141103 (2014).

[12] R. Shankar, I. Bulu, and M. Loncar, Appl. Phys. Lett. 102, 051108 (2013).

[13] B. J. Frey, D. B. Leviton, and T. Madison, Proc. SPIE 6273, 62732J (2006).